



Center of Excellence for Explosive Detection, Mitigation and Response

Center of Excellence for Explosive Detection, Mitigation and Response

A Department of Homeland Security
Center of Excellence

University of Rhode Island (URI);
California Institute of Technology; Purdue University
New Mexico State University; University of Illinois
Hebrew University, Jerusalem Israel

Second Annual Report
October 2009-April 2010

DHS agreement number: 2008-ST-061-ED0002

Table of Contents

Introduction	1
Characterization	
<i>Denaturing Explosive Precursors</i> James Smith & Jimmie Oxley (URI)	5
<i>Performance Estimation for HME</i> Jimmie Oxley & James Smith (URI)	9
<i>Theoretical Projects within the Center of Excellence</i> Ronnie Kosloff (Hewbrew UJI) & Yehuda Zeiri (BGU)	17
Detection	
Viewgraph overview	25
<i>Explosive Particles Sampling & Detection</i> Yehuda Zeiri (Ben Gurien U)	26
<i>Optical Chemical Sensors using Nanocomposites from Porous Silicon Photonic Crystals & Sensory Polymers</i> William Euler (URI)	38
<i>A Persistent Surveillance Technique for the Detection of Explosives and Explosive Precursors</i> Otto Gregory (URI)	42
<i>Fragmentation of Gas Phase Ions of Simulants & Explosives</i> Gary Eiceman (NMSU)	50
Mitigation	
<i>Damage Criterion and Residual Life of Structural Steel Subjected to Blast Loading</i> H. Ghonem (URI)	53
<i>Attenuation & mitigation of stress waves propagating in blast shielding materials</i> Carl Ernst Rousseau (URI)	56
<i>Development of Novel Composite Materials & Structures for Blast Mitigation</i> Arun Shukla (URI)	59
<i>Structural Response to Non-ideal Explosions</i> J. E. Shepherd (California Institute of Technology)	66
<i>Water Blast Mitigation: Progress Report</i> Steve Son (Purdue University)	70
<i>Self Healing Materials for Autonomic Mitigation of Blast Damage</i> Nancy R. Sottos (U of Illinois)	78
<i>Self-Healing Concrete</i> Arijit Bose (URI)	86

University of Rhode Island (URI)
DHS CoE in Explosives Detection, Mitigation, Response & Characterization

The mission of the DHS Center of Excellence in Explosives Detection, Mitigation, Response is to protect the nation from physical and economic harm caused by the threat, real or perceived, of attack using explosive devices. We take a four part approach to achieving our mission:

- identification/characterization of the most likely explosive threat scenarios to include compositions/formulations and design of ways to counter threat scenarios;
- development of detection schemes appropriate for each threat should countering fail;
- design and retrofit structural components to mitigate catastrophic results if there is failure at preventing a bombing.
- education of the next generation

Identification of the threat has included a literature review of explosive scenarios involving vehicle-borne improvised explosive devices (VDIED) as well as the types of explosives used in those events. Our approach includes the following

- identification of future threats by developing small-scale, “early warning” tests;
- determination of ways to prevent commonly available chemicals from being used to make explosives, including chemical denaturation and administrative controls;
- determination of explosive properties which would facilitate detection, destruction, or protection against threats. These objectives are being addressed by both theoretically and experimentally

Development of detection technologies for trace, bulk, standoff and persistent detection will continue. URI and partner universities are emphasizing trace, standoff and persistent detection schemes. New efforts in simulants will address needs for bulk detection. Northeastern University and partners are emphasizing standoff detection and improvement of data processing algorithms.

Protection of structures and structural components has focused on developing new materials, such as sandwiched and functionally graded, as well as self-healing concrete and polymers. In addition to new materials, projects have sought to model structural response for the purpose of new design criteria and for damage projections. Fundamental behavior, e.g. internal friction mechanisms; means by which they attenuate, deflect, channel, or scatter stress waves. When these are understood, mechanical response can be better handled with predictive approaches. The study of wave propagation and internal friction in particulate and graded composites will help bring fundamental behaviors and practical outcomes to light.

If you have any questions, please contact me—Dr. Jimmie C. Oxley 401-874-2103
joxley@chm.uri.edu

Education: Our work in this field to date is as follows. Each University project in the Center supports one or more graduate students. This is their best learning experience. Undergraduates are also supported on the projects as their class schedules permit. Since Spring we have performed five magic shows for elementary and junior high students. We opened our university labs for summer research experience for seven high school teachers and six undergraduates in the summer of 2009 and will have a similar number in summer of 2010. On February 2 we again participated in Ground Hog's Day Shadowing with two middle school students spending the day in our labs.

We have hosted and participated in a number of educational workshops.

TSA VIPER Port of Davisville	Aug. 7, 2009
TSA VIPER Block Island Ferry	Aug 14, 2009
a meth/explosive improvised lab workshop for RI first responders	Aug 17-21, 2009
workshop on thermal analysis of explosives at NATAS	Sept. 20, 2009
detection of explosives workshops for users and venders	Oct 9, 2009
Homeland Security S&T Advisory Committee	Jan 28, 2010
Delta airline security	Jan 29, 2010
URI Foundation Board	Jan 30, 2010
American Assoc. of Forensic Scientists	Feb.23, 2010
TSWG Homemade Explosive educators	March 10, 2010
ALERT safety workshop	April 30, 2010
a field day with the Massachusetts's bomb squad	May 10, 2010
TSA Bomb Appraisal Officers short courses	June 1-3, 2010
briefing to Under Secretary O'Toole	June 11, 2010
summer visiting Professor (Dr. Bu) and graduate student from Clark Atlanta University	
TSA Bomb Appraisal Officers short courses	July 25, Aug 12, Sept 16, 2010
TSA Fundamentals of Explosive short course	Aug 9-11, 2010
IMPLAST 2010	October 12-14, 2010
Texas Tech & ALERT safety course	October 27, 2010

We continued to offer specialty explosive courses for professionals with 9 new courses this year and a total of 443 professional participating.

Professional classes	Dates	# students
Fundamentals, Crane, IN	Jun 1-3, 2009	16
Fundamentals of Explosive, NJ	Jun 23- 25, 2009	22
DDT, Picatinny, NJ	July 28-30, 2009	23
Thermal Hazards of HE, NJ	Aug 3-4, 2009	16
Fundamentals of Explosives, Ottawa	Sept 8-10 2009	16
Material Response to Blast, NJ	Sept 29,30	21
Explosive Devices, NJ	Oct 27-29, 2009	25
Environmental Aspects of Explosives, NJ	Nov. 3,4, 2009	26
Fundamentals, Edwards AFB, CA	Jan 19-21, 2010	26
Fundamentals of Explosive, NJ	Feb 1-3, 2010	24
Unintended Ignitions Sources, Ottawa	Feb 3-5, 2010	20
Fundamentals, Kirkland AFB, NM	Feb 17-19, 2010	10
Unintended Ignitions Sources, Kirkland AFB, NM	Feb 17-19, 2010	12
Warhead Mechanics, NJ	Feb 23-25, 2010	25
Materials Response under Impulsive Loading, Ottawa	Mar 22-23, 2010	20
Air Blast & Structural Response, Ottawa	Mar 24-26, 2010	20
Terrorism Issues, NJ	April 26-27, 2010	40
Fundamentals of Explosives, RI	May 4-6, 2010	28
Nanomaterials, NJ	May 25, 26, 2010	25
Pyrotechnics, NJ	June 7-10, 2010	28

Denaturing Explosive Precursors

P.I. J. Smith; J. Oxley; Grad Students: J. Brady; Pat Bowden; Lucus Steinkamp; Maria Donnelly; Ryan Rettinger

Objective

The long-term *goal* is to identify ways to control chemical precursors to explosives. Some will require administrative controls; some can be adulterated yet still fulfill their intended function but not be diverted for illicit purposes. Our *approach* was to target two precursors—hydrogen peroxide (HP) and potassium nitrate (KN). For HP, we attempted to find a way to prevent concentrating widely available 3% HP. For KN we attempted to find a way to prevent its use in making urea nitrate. Both efforts have succeeded.

Summary & Accomplishments

Hydrogen Peroxide: We have tested 75 different additives for acceleration of HP decomposition at elevated temperatures (i.e. concentrating by boiling off water) but do not affect HP stability at room temperature. We have found 5 to 10 which at parts-per-million levels cause 3% HP solution to decompose rather than concentrate. These additives are not toxic and initial testing suggests no adverse affects on HP shelf-life.

Urea Nitrate: One approach to prevent terrorists from manufacturing their own explosives has been severe controls on nitric acid. Some terrorist groups have circumvented the ban by reaction of alkali nitrate with acid. To prevent synthesis of improvised nitric acid we have examined various potential additives to the nitrate salts. The approach has been to use an additive which does not affect its marketability. A desired result is for nitrate and additives to co-precipitate with the urea nitrate thus, greatly reducing its effectiveness. To date, we have examined phosphate salts appropriate for the fertilizer market where much potassium nitrate is sold. With 20 wt% added phosphates, we found the UN formed from use of the in situ nitric acid did not detonate, but this amount of additive is considered too high to be practical and lack of detonation may be a matter of scale.

Details

Hydrogen Peroxide: Figure 1 shows the concentration of HP after heating at 125°C for 8 to 10 hours. The blue line would be the concentration of HP if during heating water only was lost from HP. However, some HP is actually destroyed during heating; the black line is the observed concentration change; some additives do nothing to enhance HP decomposition (green markers). The red markers show the resulting HP concentration for HP solutions containing additives which promote HP decomposition. Among the red markers are at least 5 additives which at 1.25 ppm ($\mu\text{g/mL}$) concentration dramatically accelerated HP decomposition during heating at 125°C. Table 1 shows the additive used, the amount of additive used, and the percentage of HP destroyed in the process of distilling 3% HP to an apparent concentration of 30%. A value of "100%" represents a total destruction of HP during the distillation process.

It is important that the additive employed would not shorten the shelf-life of the product. Long-term stability is currently being examined at 4°C, 25°C, 40°C, and 60°C. The two lower temperatures represent refrigeration and room temperature storage of the HP, respectively. After nine months of storage at 4°C, ten of the most promising additives at the 1.25 $\mu\text{g/mL}$ level do not show any degradation of HP at the 3% level. The elevated temperature experiments are being conducted in flame-sealed glass ampoules to simulate long term ambient temperature storage on an accelerated time scale.

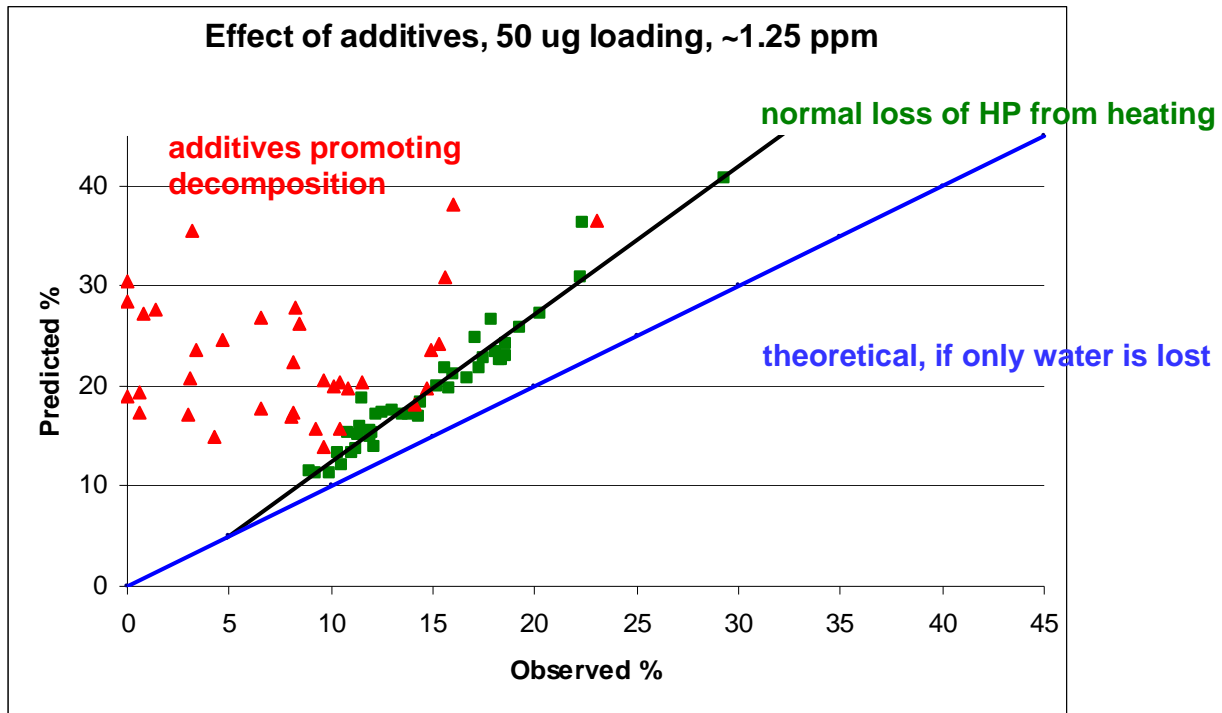
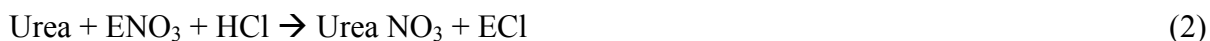
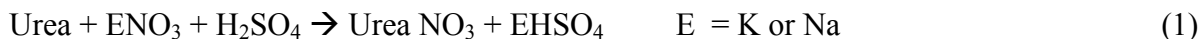


Fig. 1: HP Concentration Change upon Heating

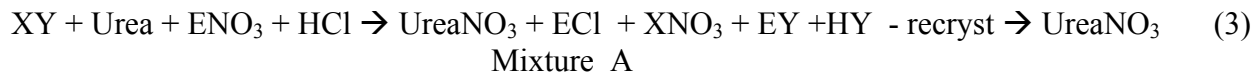
A literature search for potential toxicity of these additives was performed. It was found that all the additives except the cerium (Ce) salts are essential micronutrients. An individual would need to purposefully ingest liters of a hydrogen peroxide solution adulterated with the potential additives to exceed the FDA's Recommended Daily Allowance. We believe these additives could be used to denature HP sold into certain markets. We have found that some of the same additives used to denature 3% HP also denature 12% and 30% HP, two other commercially available concentrations of HP. Thus, it would become impossible to concentrate products such as Clairoxide 40 to use it to produce liquid explosives.

Urea Nitrate: Urea nitrate (UN) is readily prepared by addition of nitric acid to urea. The reaction does not require concentrated nitric acid or significant cooling. To prevent the synthesis of UN in certain areas of the world, authorities have restricted the availability of nitric acid. In response to this restriction terrorists have turned to a historic route to nitric acid preparation—addition of mineral acid to nitrate salt. Authorities have focused on the threat posed by KN, although both sodium and calcium nitrate would make better precursors for nitric acid preparation. We proposed to reduce the threat of UN preparation from the *in situ* generation of nitric acid from KN.

Under another program we have been investigating ways to prevent KNO₃ (KN) from being used to make black powder. In March we reported additives which were effective at the 10% level; now we find ammonium salts at the 3% level reduce burn rate by two-thirds. However, for this project we wish to prevent use of KN to produce *in situ* nitric acid, which, in turn, would be used to make urea nitrate (UN). Our aim is specifically at *in situ* preparation, that is the terrorists do not attempt to separate nitric acid from the byproduct EHSO₄ or ECl and these additives remain in the UN, thus prepared.



Our approach was to add a material which competes for the acidic proton. Thus, most of the additives tested were basic species. (Ammonium salts were effective offering the intriguing possibility that one additive might address both the black powder and the nitric acid threat.) Not only does the additive divert a portion of the available protons, but the resulting material precipitates with the UN formed and reduces the ease of initiation and performance of the UN. We prepared small (5 g) batches of UN using 12 adulterants which we thought would be acceptable for fertilizer use. (The use of KN in fertilizers was identified as one of the uses most sensitive to contamination.) Loading levels of the adulterants was 20wt% of the KN. Determination of the percentage of UN in mixture A (equation 3) was a challenging undertaking because there is presently no analytical method for examining intact UN (versus identifying the separate ions of uronium and nitrate). We met this challenge using two analytical techniques: recrystallization and thermogravimetric analysis (TGA). Since UN is thermally labile, it completely decomposes upon heating leaving only the inert inorganic salts. Success was judged by low weight loss after heating Mixture A by TGA or by low yields of UN after recrystallization. The desired result is such a low level of UN in Mixture A that it is impossible to initiate or detonate at any reasonable size.



To test detonability we choose one adulterant (ammonium sulfate) and participated in the preparation of several hundred pounds of UN. In that set of tests, UN was made by four methods:

- a) urea plus nitric acid;
- b) urea plus NaNO₃ + HCl
- c) urea plus KNO₃ + HCl
- d) urea plus KNO₃ + (NH₄)₂SO₄ + HCl

Upon initiation the formulations performed as follows A >> B > C > D

We attribute this differentiation in response to the level of inert materials deposited along with the UN. Simply by forcing terrorists to use something other than commercial nitric acid greatly reduced the yield of UN. The UN that is made from alkali nitrate salts is contaminated to some extent, depends on the solubility, with EHSO_4 or ECl (equation 1 or 2). For example, when the byproduct is NaCl , it is so soluble that it stays in the rinse water and does not dilute the effectiveness of the UN as dramatically as KN (hence prep B performed better than prep C). Preparation D performed worst of all, the detonator simply scattering the UN rather than detonating it. However, due to the wetness of all formulations, we feel that further proof of concept is needed and plan to achieve it during the next research year.

Future Work

Hydrogen Peroxide: Stability studies and toxicity reviews will continue. Additives which have proved effective in preventing concentration of 3% HP will be more thoroughly tested on 12% and 27% HP.

Urea Nitrate: A wider range of additive will be tested, seeking materials which are effective at the 3% level or less.

Chlorates: A new initiative will examine by literature review and/or experiments chlorate decomposition mechanisms so that materials which affect those pathways can be identified.

Graduate Students (partially supported PhD candidates)



Joe Brady Pat Bowden Ryan Rettinger Jon Canino Lucus Steinkamp Maria Donnelly

Presentations & Papers

Gordon Research Conference Poster

Master's Thesis Joseph Brady

The Explosive Threat, invited briefing to U/S Tara O'Toole, June 11, 2010

"Looking for HME: What, Where, With What; Bomb Squad Conf. Philadelphia, May 3, 2010

Pre- and Post-Blast: What to Look For, What to Look With, Am. Assoc of Forensics Scientists, Seattle, Feb 23, 2010

RI Emergency Management Advisory Council; URI Feb 9, 2010

DHS Center of Excellence: an Overview; URI Foundation Board, Jan 30, 2010

Studying Energetic Materials for Safety & Security; Miami, Florida International U, Jan 14, 2010

Peroxide Explosives—Hazards & Remedies; Tel Aviv, Dec 9, 2009

HME—Old Explosives, New Applications, Tel Aviv, Dec 8, 2009

Characterization: Performance Estimation for HME

PI J. Oxley, J. Smith, J. Kennedy, S. Stewart; Grad Students: P. Bowden & R. Rettinger

Non-ideal Explosives Characterization: What kinds of fundamental research can be done to better understand non-ideal explosives and mixtures of explosives? What kinds of research will provide better predictive capability for improved detection of these types of explosives?

The long-term **goal** is to develop a test that allows early identification of detonable formulations and prediction of their detonation velocity and critical diameter. Our **approach** is to surround a cylinder of “acceptor” material with an annular “booster” of detonable material.

Work to date:

In the last year we conducted four live tests of our approach [March (20 shots), August (22 shots), November (36 shots) 2009 and May 2010 (41 shots)]. In the first three test series the device contained roughly 950 g (2 lb) total explosive weight surrounding a ~1” cylinder of the test material, about 60 mL volume. Those tests indicated that the length and width of the booster charge (a 4” x 4” right cylinder) were not critical to the results; thus, in the May 2010 test series the outer cylinder was reduced to 3” in diameter, reducing the total explosive weight to about 500 g (1 lb). The test series experimented with the following variables:

- type of flyer (series 1: flat disk; series 2 & 3: stainless steel ball; series 4: none);
- stand-off distance from the witness plate;
- detonator interrupter (low density polyethylene, high density polyethylene, none);
- mode of initiating the booster;
- chemistry of the booster and acceptor.

In the **first test series**, a nickel coin was used as a flyer plate to impact a 1” thick steel witness plate about 7 mm beneath the test fixture. The annular booster was a detonable hydrogen peroxide (HP)/H₂O/ethanol (EtOH) mixture (60/27/13 wt%) and the test material was a variety of HP formulations, mainly those believed to be non-detonable based on the ternary diagram. A variable in this series was the amount of sheet explosive used to couple the detonator impulse to the annular booster: one or two 2 mm sheets. A detonator interrupter (Fig 1- purple section), preventing impulse from going directly into the center acceptor material was placed below the sheet explosive. Severe bowing of the witness plate from the detonation of the annular booster and poor reproducibility of flyer dent caused us to change device configuration.

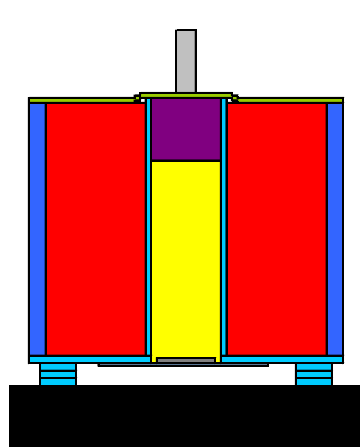


Fig. 1: Series 1 Fixture

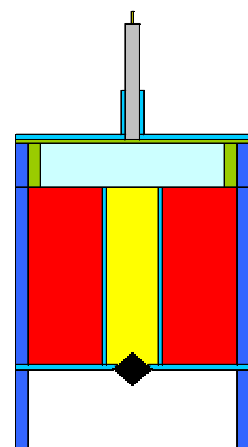


Fig 2: Ribbon Design

Table I: Test Series 1 (Aug 2009)(colors indicate repeats)
Red letter test in steel

Test #	outer tube	inner tube	Inner HP %	inner mix HP/EtOH/H ₂ O	# sheets HE	max mL	Max Dent (mm)
18	A	G	50	G= 50% HP only	1	11.5	2.01
8	A	A	70	A= 60/26/14	1	15	3.02
3b	A	A	70	A= 60/26/14	2	17.5	4.47
14	A	F	35	F= 27/50/23	1	17	4.52
3a	A	A	70	A= 60/26/14	2	20.5	4.75
4	A	water	0	water	2	18.5	5.31
9	A	F	35	F= 27/50/23	1	17	5.44
15	A	C	50	C= 47.6/47.6/4.8	1	17	5.44
13	A	G	50	G= 50% HP only	1	6.5	5.46
1	A	C	50	C= 47.6/47.6/4.8	2	24	5.64
7	A	A	70	A= 60/26/14	2	30	5.72
10	A	C	50	C= 47.6/47.6/4.8	1	30	6.86
5	A	G	50	G= 50% HP only	2	28	7.8
16	A	G	50	G= 50% HP only	1	24.5	7.98
17	A	oxy	--	solid percarbonate	1	31.5	10.2
6	G	--	50	50%HP only	2	no go	
2	1"	C	50	C= 47.6/47.6/4.8	2	no go	
11	F	--	35	27/50/23	1	no go	
12	C	--	50	47.6/47.6/4.8	1	no go	
19	H	--	70	70% HP only	1	no go	

Outer booster is mix A= (60.45 HP/25.91EtOH/13.64H₂O)

In test series 2 and 3 a stainless steel ball flyer was used and stand-off was varied. For test series 2, the sealing of the flyer ball to the fixture was accomplished by melting the polycarbonate with dichloromethane, but leakage was a problem in many tests. The **second test series** used the same HP/H₂O/EtOH annular booster as series 1, in almost all tests. Six inch stand-off distance was determined to produce observable dents from the center test material without causing severe damage to the witness stack by the booster. In this test series, the sheet explosive configuration was varied from flat across the entire cylindrical device, with HDPE interrupter, to a ribbon of several strips of sheet explosive positioned 90° to the fixture top edge (Fig 2). The ribbon configuration produced smaller dents and was abandoned for the easier to fabricate flat initiator. Reproducibility of results was better, but differentiation between an inert (H₂O) and a detonable material (60/27/13 HP/H₂O/EtOH) was not great (0.068 to 0.106, respectively). Fixture length was increased from 4” to 8” without a dramatic change in results. What did change the results was changing the booster from HP/H₂O/EtOH to sensitized nitromethane (NM). It was clear sensitized NM was a more powerful annular booster.

Table 2

Test Series 2 (Nov 2009)

Standoff Distance	variable	annular booster	inner test material	dent depth	Repeatability	variable	annular booster	inner test material	dent depth		
1	4" device	2"	A	C	-0.116	3	4" device, 6" standoff	interrupter	A	C	-0.127
2	4" device	4"	A	C	-0.13	14	" " " "	interrupter	A	C	-0.103
3	4" device	6"	A	C	-0.127	9	" " " "	interrupter	A	C	-0.06
14	4" device	6"	A	C	-0.103	7	4" device, 6" standoff	ribbon	A	C	-0.074
4	4" device	8"	A	C	-0.052	8	" " " "	ribbon	A	C	-0.086
6	4" device	8"	A	C	-0.072	5	4" device, 6" standoff	interrupter	NM	C	-0.431
Initiation Configuration					Range of Results (inert H2O to detonable mix A)						
3	4" device, 6" standoff	interrupter	A	C	-0.127	12	4" device, 6" standoff	interrupter	A	H2O	-0.068
14	" " " "	interrupter	A	C	-0.103	14	" " " "	interrupter	A	C	-0.103
7	4" device, 6" standoff	ribbon	A	C	-0.074	13	" " " "	interrupter	A	A	-0.106
8	" " " "	ribbon	A	C	-0.086	10	4" device, 6" standoff	ribbon	A	H2O	-0.077
12	4" device, 6" standoff	interrupter	A	H2O	-0.068	7	" " " "	ribbon	A	C	-0.074
10	4" device, 6" standoff	ribbon	A	H2O	-0.077	8	" " " "	ribbon	A	C	-0.086
13	4" device, 6" standoff	interrupter	A	A	-0.106	11	" " " "	ribbon	A	A	-0.063
11	4" device, 6" standoff	ribbon	A	A	-0.063	18	8" device, 6" standoff	interrupter	A	H2O	-0.058
5	4" device, 6" standoff	interrupter	NM	C	-0.431	17	" " " "	interrupter	A	C	-0.146
15	" " " "	interrupter	NM	C	-0.418	19	" " " "	interrupter	A	A	?
22	4" device, 6" standoff	ribbon	NM	C	-0.309	Device Length					
Device Length					Booster Chemistry						
3	4" device, 6" standoff	interrupter	A	C	-0.127	3	4" device, 6" standoff	interrupter	A	C	-0.127
14	" " " "	interrupter	A	C	-0.103	14	" " " "	interrupter	A	C	-0.103
17	8" device, 6" standoff	interrupter	A	C	-0.146	5	4" device, 6" standoff	interrupter	NM	C	-0.431
5	4" device, 6" standoff	interrupter	NM	C	-0.431	15	" " " "	interrupter	NM	C	-0.418
15	4" device, 6" standoff	interrupter	NM	C	-0.418	17	8" device, 6" standoff	interrupter	A	C	-0.146
20	8" device, 6" standoff	interrupter	NM	C	-0.406	20	8" device, 6" standoff	interrupter	NM	C	-0.406

A=detonable H₂O₂/EtOH A= 60%HP, 25% H₂O, 15% EtOH C=non-detonable H₂O₂ mix C=48%HP, 48% H₂O, 5%EtOH
 NM = nitromethane @ 4% DETA

For **third test series**, the change to sensitized nitromethane booster required a redetermination of appropriate standoff distance; experimentation suggested 10” was best. The change also required investigation into the safest way to sensitize NM. Diethylenetriamine (DETA) reacts with HP, therefore, concentrated nitric acid (70 wt%) was used to sensitize NM. Preliminary experiments suggested NM with 10% nitric acid (NA) was not detonable at 1”; therefore, most of the tests were primarily performed using 30% NA although 20% and 50% concentrated NA were also tested.

Table 3.1

Test #	Size inches	Inner Mix	Outer Mix	Dent Depth (mm)	Volume (mL)	Standoff (inch)
1	4x4	C = 50HP/5EtOH	O= 8/2 NM/NA			6
2	4x4	C	O= 8/2 NM/NA	-9.91		8
3	4x4	C	O= 8/2 NM/NA			10

In the third series one variable examined was the size of the test fixture; it was increased from 4” to 6” in diameter and from 4” to 8” in length. The dents produced by the larger devices were not noticeably different from the smaller device; thus, in keeping with the goal of using less energetic material, the 4” x 4” fixture was used in most tests. In some tests in series 3 there was more than one main dent (Fig 13).

Table 3.2 Test Series 3 (November 2009)

Liquid Test Materials

Test #	Size inches	Inner Mix	Outer Mix	Dent Depth (mm)	Volume (mL)	Standoff (inch)	Comment
15	4x8	7/3 NM/NA	P = 7/3 NM/NA	0.0	0.00	10	Ball in Dent
5	4x4	8/2 NM/NA	O= 8/2 NM/NA	-2.5	1.05	10	Ball Dent
9	4x4	P	P	-2.9	1.01	10	2 dents
32	4x8	A= 70HP/13EtOH	P	-5.0	1.48	10	Ball Dent
18	4x4	A= 70HP/13EtOH	P	-5.5	2.03	10	Ball Dent
22	6x8	P	P	-6.6	1.26	12	Ball Dent
11	4x4	C = 50HP/5EtOH	50/50 NM/NA	-9.1		10	2 dents
10	4x4	C	98/2 NM/deta	-14.5	2.16	10	2 dents
21	6x8	C	P	-15.5	6.65	12	Jet Dent
7	4x4	C	P= 7/3 NM/NA	-16.5	5.30	10	Jet Dent
3	4x4	C	O		2.34	10	2 dents
31	4x8	C	P	-17.0	8.18	10	Jet Dent
14	4x8	C	P	-18.3	7.05	10	Jet Dent
4	4x4	H2O	O	-19.3	5.16	10	2 dents
12	4x4	Brine	50/50 NM/NA	-19.3	6.88	10	Jet Dent
8	4x4	Brine	P	-24.4	7.59	10	Jet Dent
16	4x8	Brine	P	-25.4	13.53	10	Jet Dent

Solid Test Materials and Special Tests

Test #	Size inches	Inner Mix	Outer Mix	Dent Depth (mm)	Volume (mL)	Standoff (inch)	Comment
28	4x4	Percarbonate	P	-12.2	3.64	10	
25	6x8	DNT	P	-12.4	5.16	12	
17	4x4	Sand	P	-13.5	4.57	10	
19	4x4	Bullseye	P	-14.7	4.04	10	
20	4x4	AN	P	-14.7	3.94	10	
29	4x8	AN	P	-15.0	4.66	10	
23	4x4	Sugar	P	-16.0	4.68	10	
26	4x4	DNT	P	-24.6	8.27	10	
24	4x4	empty	P	-6.858	0.87	10	Multiple Dents
27	4x4	C	P	-3.048	0.99	28	
33	4x4	C	P	--	--	10" + sand	

Ordering test materials in Table 3.2 from smallest to largest dent, no clear trend is seen among the solid materials; but for the liquids, materials known to be detonable came out on top; those known to be inert, on the bottom. This is a trend but exactly opposite from what we expected. We had expected that detonable materials would drive the flyer ball deep into the witness plate whereas inert materials would barely push it. Instead, inert materials, such as water and brine, bore large holes in the 1” steel witness plate and the detonable material left only the dent of the flyer ball (Fig. 2). In attempt to understand this phenomenon, Scott Stewart (U of Illinois) modeled the test series 3 setup using ALE3D (Fig. 3). The ALE3D model suggested that inert materials were propelled out of the inner tube as a jet which overtook the flyer ball, impacting the witness plate before the ball, hence, the presence of two dents in some test.



Fig. 2: Top: Shot 8 Brine in center; Bottom: Shot 9 same as booster 70/30 NM/NA

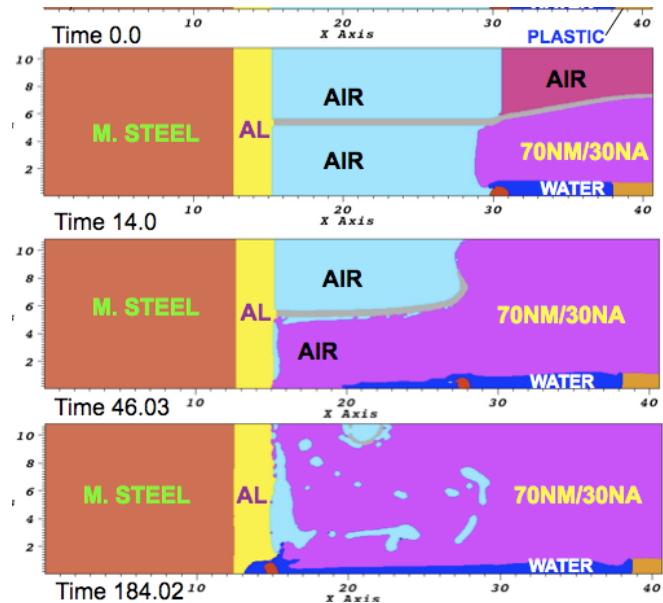


Fig. 3: ALE3D Model of Series 3 Water Shot

The **fourth test series** used the previous test to guide a number of changes in the test fixture. The overall fixture was reduced in outer diameter to 3” so that only about 1 lb of explosive was required for the annular booster. This reduction in size was possible because of the change in annular booster from HP to NM. To make the inner tube walls impervious to NM, it was constructed of PVC rather than acrylic or polycarbonate; as a result its diameter became a little larger than 1.” The biggest change was elimination of any flyer. We relied on a jet of unreacted material or lack thereof to leave its mark on the 7” stack witness plates, the top 2” of which were changed to aluminum in order to allow better differentiation between inert and explosive test materials. Table 4 shows a clear trend, albeit in reverse of our initial expectations. There is also a trend among the solid test materials, but unlike the liquid explosives, the solid explosives, e.g. the commercial emulsion explosive MagnaFrac® (Orica), produced a dent, though smaller than that made by the inert polymethylmethacrylate (PMMA).

Table 4.1 Test Series 4 Solid Test Materials

Shot #	Stand-Off Inches	Inner Mix	Booster	Dent Depth (mm)	Volume (mL)	g of inner mix
Solid Inner Material						
39	8	MagnaFrac - no det int	70/30 NM/NA	-14	4	84
24	8	DNT - no det int	70/30 NM/NA	-16	5	81
21	8	87/13 AN/IS - no det int	70/30 NM/NA	-17	6	82
23	8	70/30 KN/IS - no det int	70/30 NM/NA	-18	8	100
20	8	AN - no det int	70/30 NM/NA	-20	11	82

Table 4.2 Test Series 4 Liquid Test Materials

Shot #	Stand-Off Inches	Inner Mix	Booster	Dent Depth (mm)	Volume (mL)	g of inner mix	mm.g	cm3/g
Liquid Inner Materials								
14	8	70/30 NM/NA - No Det. Int.	70/30 NM/NA	-2.3	0	89	0	0
35	8	70/30 NM/NA	50/50 NM/NA	-3.5	0	67	0	0
19	8	80/20 NM/NA	70/30 NM/NA	-4.5	0	66	0	0
36	8	70/30 NM/NA	80/20 NM/NA	-4.7	0	67	0	0
40	8	70/30 NM/NA	98/2 NM/DETA	-4.7	0	66	0	0
5	8	70/30 NM/NA	70/30 NM/NA	-5.1	0	65	0	0
41	8	70% HP/ 13% EtOH	98/2 NM/DETA	-11	9	66	0	0.14
17	8	90/10 NM/NA	70/30 NM/NA	-11	8	65	0	0.12
18	8	95/5 NM/NA	70/30 NM/NA	-11	4	63	0	0.07
34	8	99.5/0.5 NM/DETA	70/30 NM/NA	-12	13	63	0	0.2
38	8	NM	98/2 NM/DETA	-12	10	63	0	0.16
25	8	50/50 NM/NA	70/30 NM/NA	-13	8	71	0	0.12
9	8	NM	70/30 NM/NA	-13	10	63	0	0.15
31	8	80/20 NM/EtOH	70/30 NM/NA	-13.2	6	60	0	0.11
11	8	80/20 NM/Acetone	70/30 NM/NA	-16	7	59	0	0.12
10	8	90/10 NM/Acetone	70/30 NM/NA	-16	11	61	0	0.19
12	8	70/30 NM/Acetone	70/30 NM/NA	-16.8	5	56	0	0.1
33	8	30/70 NM/NA	70/30 NM/NA	-16.2	10	73	-0.22	0.14
27	8	70/13 HP/EtOH	70/30 NM/NA	-19	7	67	0	0.1
16	8	Acetone	70/30 NM/NA	-24.1	12	45	-0.54	0.26
29	8	50/10 HP/EtOH	70/30 NM/NA	-25.9	17	63	-0.41	0.27
30	8	50/30 HP/EtOH	70/30 NM/NA	-27.9	12	59	-0.48	0.2
15	8	Turpentine	70/30 NM/NA	-29.2	22	49	-0.59	0.44
28	8	70% HP	70/30 NM/NA	-32.7	24	71	-0.46	0.34
7	8	50/5 HP/EtOH - No Det. Int.	70/30 NM/NA	-37.0	25	85	-0.43	0.29
6	8	50/5 HP/EtOH	70/30 NM/NA	-38.9	23	64	-0.61	0.36
1	2	Brine	70/30 NM/NA	-39.4	36	67	-0.59	0.54
26	8	70% wt NA	70/30 NM/NA	-43.4	23	82	-0.53	0.28
3	6	Brine	70/30 NM/NA	-45.0	27	66	-0.68	0.41
13	8	Brine - No Det. Int.	70/30 NM/NA	-45.9	20	86	-0.54	0.23
2	4	Brine	70/30 NM/NA	-47.3	36	67	-0.71	0.53
8	10	Brine	70/30 NM/NA	-47.6	26	66	-0.72	0.39
4	8	Brine	70/30 NM/NA	-50.8	26	66	-0.77	0.39
32	8	99.5/0.5 NM/DETA	NM/0.5%det	did not detonate				
37	4	Brine	70% HP/ 13% EtOH	-6	1	66	-0.09	0.01
42	2	70/30 NM/NA	70% HP/ 13% EtOH	-3	0	65	-0.05	0

Summary

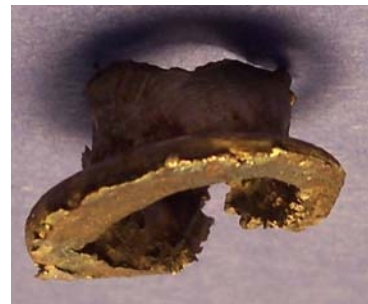
We have a test which differentiates energetic materials from non-detonable and detonable materials. The test requires only one pound of explosives. We would like to have a clearer differentiation of the line. In subsequent tests we may find a way to instrument the test.

Experimental Details

Test Series 1

A flyer plate or ball was used in the first 3 test series with the intention that the depth of the dent created by the impact of the flyer would provide the metric for rating performance. In series 1, 2 and 3 the most commonly used fixture was a PVC cylinder (4" inside diameter by 4" high) with a ~1" concentric cylinder made of acrylic or polycarbonate. Both cylinders were fixed to a PVC base. The top of the center tube was fitted with a detonator interrupter (usually a 1" tall cylinder of high density polyethylene, although low-density polyethylene plugs wrapped in Saran wrap were used in a few tests). The purpose of the interrupter was to prevent the impulse from the detonator and sheet explosive to directly affect acceptor material (Fig 5).

In test series 1 the flyer was a nickel (Fig 6-8) and the stand-off from the steel witness plate was 6.6 mm. This configuration was abandoned due to the extreme damage to the witness plate from the annular booster, while there was little denting from the flyer. No differentiation was observed between known detonable, questionably detonable, and water as acceptor material. Methylene chloride was used to melt fixture components together; this proved inefficient at preventing leakage.



From left: Fig 5: Filling fixture; Fig 6: Affixing thin PVC sheet & nickel; Fig 7 & 8: Recovered nickels

Test Series 2 and 3

In series 2 and 3 the flyer was changed to a ½” stainless-steel ball half way in and out at the center of the base (Fig 9).



From left: Fig 9: Flyer ball; Fig 10: Filling booster; Fig 11: Fixture before detonating

In test series 1 and 2 the annular booster was a mixture of 70% wt HP with ethanol (EtOH). However, in a few shots in test series 2 a sensitized nitromethane (NM) mixture (center photo above) was used and found to provide such a stronger impulse that in test series 3 only sensitized NM was used as the annular booster. It was necessary to do a certain amount of experimenting to determine how best to sensitize the NM. Traditionally, diethylenetriamine (DETA) is used, but it reacted unfavorably with HP. We found that adding 20, 30, or 50 wt% concentrated (65-70% wt) nitric acid (NA) allowed the NM to initiate in the configuration of the fixture. The polycarbonate center tube used for series 2 and 3 was immediately destroyed by NM, neat or sensitized with DETA. In some cases the shot was fired before the tube leaked. The tubes were not destroyed as quickly when NA was the sensitizing agent. The acceptor material was varied

from inert materials (water, brine, sugar and sand) to materials of questionable detonability [50% HP + EtOH, 2,4-dinitrotoluene (DNT), Bullseye® smokeless powder, sodium percarbonate (Oxiclean®)] to mixtures of known detonability (70% wt HP with EtOH and sensitized NM).



Far Left: Fig 12: Witness plates illustrating more powerful NM/DETA mix (test series 2); All plates have TM-C (48/48/4 HP/H₂O/EtOH) as acceptor mix, top plates are Shots #5 & #15 with NM/DETA outer & bottom plates are Shots #3 and #14 with TM-A (60/27/13 HP/H₂O/EtOH).
Left: Shot #3 from Test Series 3 illustrating two dents.

Surprisingly, the dent found was largest for inert samples and smallest for detonable material. We attributed this to a high-velocity jet formation. Modeling was performed by Scott Stewart using ALE3D. Using a constitutive burn the fixture was modeled with either water or the booster material in the inner tube. Simulations were matched to the experimental results.

Test Series 4

Forty-one successful tests were carried out in May, 2010. Overall fixture dimensions were reduced to 3” diameter but retained 4” height. Inner tube (1.17” in diameter) and the entire fixture were made of PVC which made it resistant to NM and made it easier to seal against leaks (Fig 14). Standoff spacers maintained a 4” diameter in an effort to decouple the blast effects from the witness plate. Most shots used a 70/30 mix of nitromethane (NM) and 66% wt nitric acid (NA) and had 8” standoff. Witness plates were 2”x5”x5” aluminum (Al) on top of a stack of 5 1”x5”x5” steel plates. Three liquid acceptors and all solid acceptors were done without detonator interrupters.



Witness plates showed four characteristic responses: uniform depression (Fig 15) for detonation of acceptor mix, hole (Fig 16) for inert or partial reaction, spike/depression (Fig 17) and non-specific (Fig 18).



Fig 15: Shot #42
Uniform Depression



Fig 16: Shot #2
Hole



Fig 17: Shot #38
Spike/Depression



Fig 18: Shot #31
Non-specific

Fig 14: “Wedding Cake” design

Graduate Students (partially supported PhD candidates)



Pat Bowden (California native, dressed for bombing making exercise with MA State bomb squad)



Ryan Rettinger (New Mexico native, determining hydrogen peroxide concentration by titration)

Presentations & Papers

Gordon Research Conference Poster

A conference paper in IMPLAST 2010 Conference report proceedings has been accepted

Featured in Discovery Canada upcoming show

“Looking for HME: What, Where, With What; Bomb Squad Conf. Philadelphia, May 3, 2010

Pre- and Post-Blast: What to Look For, What to Look With, Am. Assoc of Forensics Scientists, Seattle, Feb 23, 2010

RI Emergency Management Advisory Council; URI Feb 9, 2010

DHS Center of Excellence: an Overview; URI Foundation Board, Jan 30, 2010

Studying Energetic Materials for Safety & Security; Miami, Florida International U, Jan 14, 2010

Developing Small-Scale Tests to Predict Explosivity; Sept 21, 2009 NATAS Lubbock Tx

Theoretical Projects within the Center of Excellence

Ronnie Kosloff and Yehuda Zeiri

Hebrew University Israel

I. Objective

The goal is to establish and apply theoretical methods that will be able to predict the sensitivity and detonatability of energetic materials. The theoretical study performed in Israel is aimed at three main objectives:

- Understanding of the details of detonation processes in liquid explosive. These include two main issues: the identification of the reaction products following the detonation and sensitivity changes in mixtures of detonable materials and different fuel materials. These subjects are being studied using the molecular dynamics approach.
- The development of reliable method to obtain the vibrational spectrum of energetic materials. We are interested in the whole vibrational spectrum including low frequency modes (TeraHerzt region). The main goal is to devise a method that will enable one to link between the vibrational frequencies obtained and the vibrational modes they correspond to. This goal is being achieved using a newly developed approach based on the molecular dynamics method.
- To utilize electronic structure calculations to develop procedures that will allow simple and safe routes to destroy large quantities of improvised explosives. We focus mainly on peroxide based explosive.

II. Accomplishments

Detonation of liquid explosives: The effort this year was devoted to establish computational tools to simulate, from first principles, the properties of liquid explosives. We chose liquid Nitromethane as our primary research subject since it has been extensively studied both experimentally as well as theoretically. Our study employs the molecular dynamics method using a reactive force field (REAXFF). Calculations were carried out under various conditions of constant temperature and compression. We identified a change of decomposition mechanism that occurs at an intermediate density. For low density at elevated temperatures the first step in the thermal decomposition is the breakup of the nitrogen carbon bond. At high density there is a transition of the initial decomposition mechanism towards a bimolecular reaction with a proton transfer. This change of decomposition mechanism may explain the large experimental difference between Nitromethane detonation in liquid and solid forms. This study is an important step in establishing a computational method for predicting the initiation and detonation properties of liquid explosives.

THz Spectroscopy: Our next effort was to establish a first principle simulation of THz spectroscopy for explosive crystalline material. The basic idea is to extract the vibrational spectrum by simulating the dynamics of the dipole tensor. The spectrum is then extracted by a spectral filter applied to the calculated dipole correlation function. We find good agreement between the method we developed and the experimental data for RDX.

Peroxide based explosive disposal: Disposal of TATP and other peroxide based improvised explosives is a major problem. We assisted the experiments carried out in URI by electronic structure calculations of metal ion-TATP complexes. The purpose of these calculations was to identify a suitable catalyst for safe disposal of improvised explosives. We suggest an additional role of high ion concentrations as a means to screen van der Waals (VDW) forces and allow dissolution of TATP.

III. Details

Thermal decomposition of liquid Nitromethane at different temperatures and compressions.

Work carried out by Dr. Naomi Rom

Nitromethane (H_3CNO_2 , NM), a high explosive (HE), has been studied intensively experimentally and theoretically both in crystalline phase and the liquid phase. Here we focus on reactive molecular dynamics simulations in the liquid phase, aiming at identifying and quantifying the detailed chemical reactions starting from the first decomposition steps all the way to the formation of final products. The study was performed under various temperature, compression and shear conditions. These conditions resemble rapid laser heating experiments to a constant temperature in diamond anvil cell, where sample volume is held constant.

There are computational and experimental evidences that H-transfer is the initial step of NM decomposition at high compressions (depending on temperature). For instance, in Car-Parrinello *ab initio* MD NM at 150K and compression factor of 3.0 was shown to start the decomposition via H-transfer reaction; Measured time to explosion with deuterated NM was 10 time longer than with protonated NM, supporting the suggestion that hydrogen abduction is the rate determining step. At lower density we find that the rate limiting step is the unimolecular dissociation of the C-N bond. The following table show the final stable reaction products as obtained in the simulations at different compressions.

Table 7: Main final products asymptotic amounts, at 4000K and various densities.

Frag.	d0	1.1d0	1.2d0	1.3d0	1.4d0	1.44d0
OH	0.103	0.119	0.143	0.164	0.271	0.334
H ₂	0.495	0.422	0.508	0.404	0.221	0.174
H ₂ O	0.652	0.700	0.700	0.738	0.535	0.483
CO	0.304	0.420	0.193	0.134	0.031	0.033
N ₂	0.350	0.492	0.424	0.402	0.364	0.357
CO ₂	0.318	0.272	0.247	0.244	0.211	0.149

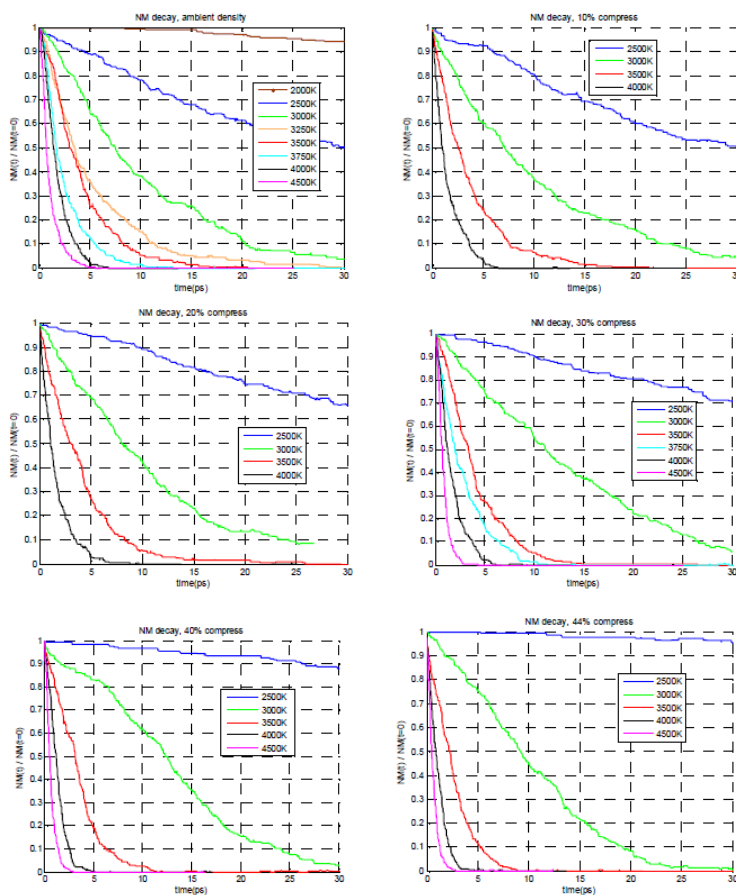


FIG. 1: Nitromethane decay vs. simulation time for various temperatures, plotted separately per density (ambient density, 10, 20, 30, 40, and 44% compressions).

Figure 1 shows the variation of the thermal decomposition rate of NM during the simulation at different temperatures (see color index in the inset) and for six initial compression values. For all compressions the decomposition is completed during the simulation for temperatures above 3000 K. At higher compression values the low temperature rate is slower than for low compressions. These rates were used to calculate Arrhenius curves, k_1 , as shown in the figure below as solid lines. In addition, the variation of the average potential energy (PE) of the system was evaluated and its initial rate of change is plotted in the figure as dashed lines, k_2 . It has been demonstrated in the literature that the PE variation can also serve as a measure of the reaction rate.

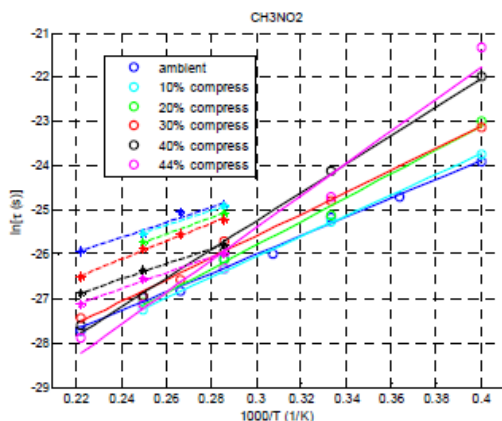


FIG. 5: Arrhenius plots for Nitromethane initial decomposition (k_1 , full lines) and Potential Energy decay (k_2 , dashed lines), for various densities. This plot unravels the different mechanism of dissociation.

In the figure below, the variation of the main reaction products during the simulation is shown. It is clear that the main products are nitrogen, water and OH radicals. At this high temperature most of the stable reaction products shown are formed within a few picoseconds.

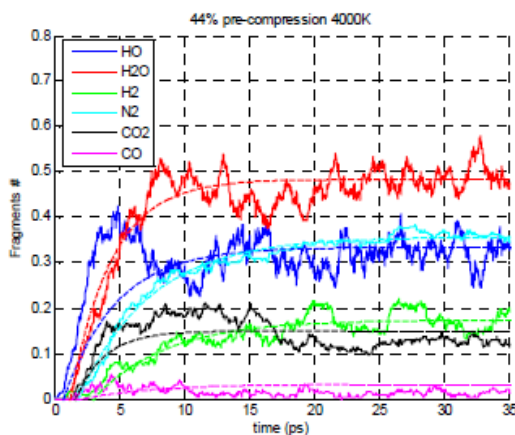


FIG. 8: Products creation and fit at 4000K.

Simulations of terahertz spectroscopy based on molecular dynamics simulations

Work carried out by Dr. Gil Katz

Remote sensing is based on the ability of light to interact with the subject matter and convey the information to the detector. Different light matter interactions can be selected by a choice of frequency band. The selection depends on the signal to noise ratio which in turn depends on the availability of intense light sources. Even more important is the specificity of light matter interaction is the band chosen. The terahertz band (THz) has become a candidate for remote sensing due to its ability to penetrate dry material and the development of new sources. The remaining question is therefore can the spectroscopy be developed to unravel

specific threatening materials. In this study we have concentrated on developing a computational scheme able to simulate THz absorption for soft organic solids.

The structure of the MD simulation allows incorporating an external time dependent dipole field. The atoms will respond by their partial charge to this force. If the frequency of the external field matches a molecular frequency the amplitude energy will be absorbed to this mode. For small molecules where the modes are isolated the energy in this mode will grow quadratically with time. This effect can be employed to determine the mode frequencies by scanning the driving frequency. For larger systems this procedure is inadequate to increasing importance of anharmonic coupling the normal mode picture breaks down. Nevertheless by scanning the driving frequency the energy absorbed by a specific mode will partition to other modes with the final result of a total increase in the energy of the molecular dynamics system. The energy increase will be proportional to the incident frequency. The procedure adopted is to apply a Gaussian pulse with a varying carrier frequency to the system and compare the energy added to the system as a function of frequency. This result should be compared to the linear response result. The advantage of this procedure is that it does not require to address specifically the dynamics of a specific mode. Fig. 2 shows excitation by a 5psec with accompanying energy increase in the molecule. The spectral resolution will depend on the pulse duration.

Filter Diagonalization could be applied to extract the frequencies and the amplitudes from a general time signal $c(t)$ only assuming that the time signal was generated by quantum dynamics, even in the case, when the time signal $c(t)$ was not generated by a quantum Hamiltonian. It should be noted that the extracted are generally complex and therefore include the contribution of the width. In this case plays the role of an effective Hamiltonian whose spectral parameters are extracted by the filter diagonalization procedure. As such the method was applied to extract the instantaneous normal modes from a time signal generated by calculating the classical trajectories of a multi-particle system. The molecular dynamics simulation has to supply the dipole correlation function. Chaotic noise generated by a non linear classical Hamiltonian even at moderate energy overwhelms the dynamics. A MD simulation in room temperature for a large system with many coupled modes leads to almost a "white" spectrum which masks the normal modes. The first step of the procedure is to anneal the system to obtain the lowest energy configuration where a normal mode description is appropriate. The second step is to calculate $c(t)$ at this configuration as well as a reference spectrum. This spectrum generated from random fluctuations usually contains the main spectral features.

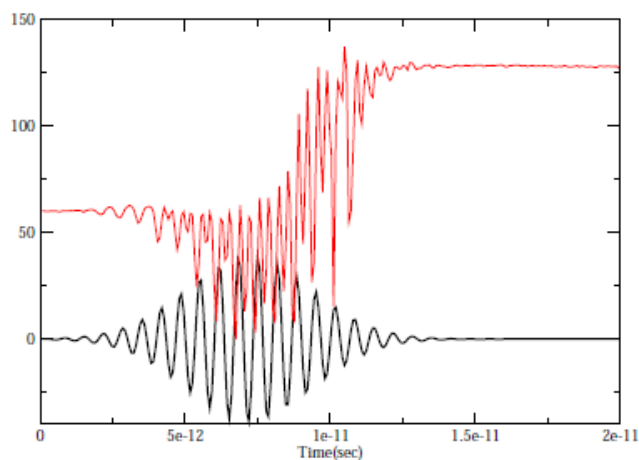


FIG. 2: A typical excitation field (black) as a function of time with carrier frequency of 1 THz and pulse duration of 5 psec. The energy absorption as a function of time of a RDX slab of one unit cell is superimposed on the pulse. The red dashed line corresponds to a peak in the absorption of 1 THz. The green solid line corresponds to pulse with frequency of 1.5 THz a minimum in the absorption.

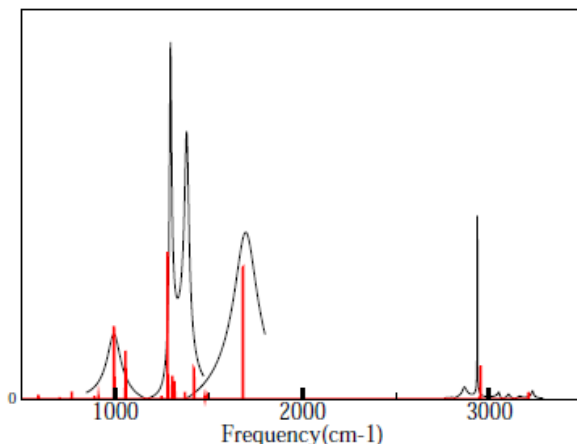
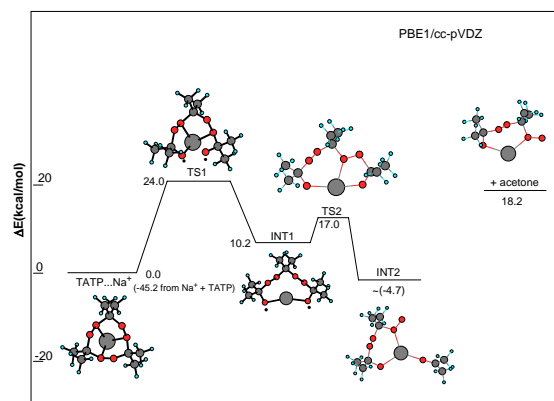


FIG. 3: The RDX spectrum calculated by MD (black) compared to electronic structure calculations. The spectrum was obtained by a spectral filter on the time series of the dipole correlation function. The electronic structure calculation was obtained using Gaussian 2003. Only the MD procedure can simulate the THz spectrum.

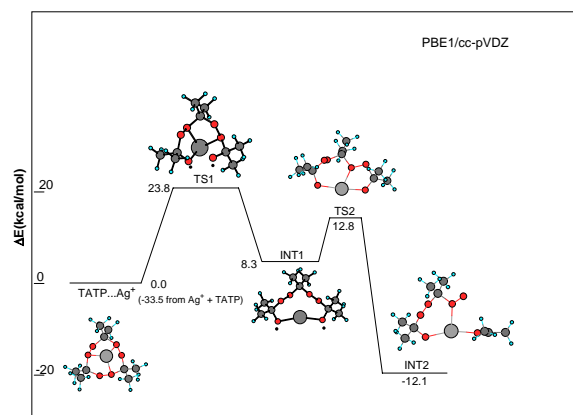
Benign disposal of peroxide-based explosives

Work carried out by Dr. Faina Dobnikova

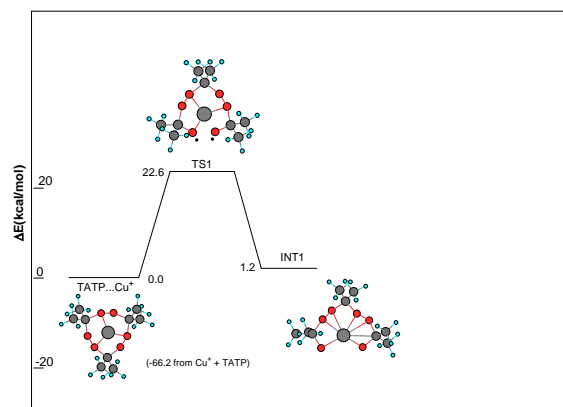
We have examined, using electronic structure calculations, the stability and thermochemistry of ion-TATP complexes. This study is an extension of our work in the past and follows the experimental work carried out in URI in the laboratory of Professor Jimmie Oxely and Prof. Jim Smith. The basic idea is to find decomposition routes which will not lead to detonation of the peroxide. We found that the methods of calculation need refinement. The reason is the charge transfer character of the metal TATP complexes. We changed the functional used in our DFT calculations. This work is still in progress since we are trying other, new and more accurate functional. We suggest very high ion concentrations in agreement with the experimental findings. The theoretical idea is to screen Van der Waals forces and thus dissolve the soft organic molecular crystal of TATP (and other peroxide based explosives). The following figures shows examples of our calculations of transition states for decomposition of TATP. All energy values in kcal/mol.



Calculated transitions states for TATP decomposition by attachment of a sodium ion



Calculated transitions states for TATP decomposition by attachment of a silver ion



Calculated transitions states for TATP decomposition by attachment of a copper ion

The following tables summarize the binding energies (E_{bind}), the energy of the first and second transition state (ST1 and ST2), energy of first and second intermediate (INT1 and INT2) for different ions.

B3LYP/cc-pVDZ method and basis set. Energy value in kcal/mol.

	E_{bind}	TS1	INT1	TS2	INT2
TATP		31.3	28.1	34.0	9.3
$\text{Na}^+ \dots \text{TATP}$	-44.7	21.5	7.4	10.6	-24.80
$\text{Na}^+ \dots \text{TATP}^*$		19.90	-7.3	12.0	
$\text{Cu}^+ \dots \text{TATP}$	-65.8	16.8	-4.8		
$\text{Ag}^+ \dots \text{TATP}$	-54.1	20.9	3.7		
$\text{Li}^+ \dots \text{TATP}$	-67.3	19.67			
$\text{Zn}^{2+} \dots \text{TATP}$	-221.9	11.8	-64.8		
$\text{Zn}^{2+} \dots \text{TATP}^*$		9.81	-40.6		
$\text{Fe}^{2+} \dots \text{TATP}^*$	-252.3	8.84	-5.82	2.25	-15.26

IV.

weak

Ido

Students Supported

Morag Am Shalem: PhD.
Subject: Molecular
dynamics simulations of
detonation waves.

Shefer: MsC. Subject:
Molecular dynamics

simulations of THz spectroscopy of TATP.

Ezra Levine: Undergraduate. Subject: Molecular dynamics simulations of shock waves in TATP.

V. Conference & Journal Publications

- 1) Gil Katz, Sergey Zybin, Adri C. T. van Duin, Yehuda Zeiri, Ronnie Kosloff, and W. A. Goddard III
Simulations of terahertz spectroscopy based on molecular dynamics simulations In preparation (2010).
- 2) Noami Rom, Yehuda Zeiri, Ronnie Kosloff and Sergey Zybin
Decomposition of liquid Nitromethane under the influence of temperature and compression. In Preparation (2010).



Trace Explosives Detection

Ion Mobility Spectrometry

Mechanism of Detection: Ionization of the Analyte
Eiceman (New Mexico State University)

Chemiresistors

Mechanism of Detection:
Polymer Swelling
Lewis (CalTech)

Particle-Substrate Adhesion
Particle Lifetime
Zeiri (Ben-Gurion University)

Porous Silicon

Mechanism of Detection:
Fluorescence Quenching
Euler/Levitsky (URI)

Catalytic Decomposition

Mechanism of Detection: Heat Evolution from Analyte
Gregory (URI)

Explosive Particles Sampling & Detection

Yevgeny Zakon, Paz Elia, Arcady P.Gershanik and Yehuda Zeiri

Ben Gurion University

Objective

The main objectives in the research were measurement and analysis of adhesion forces between explosive particles and various substrates using the method based on AFM force measurements. These measurements were performed using various explosive particles as well as alumina particles. The alumina particles were also employed in the aerodynamic approach to measure adhesion forces with the goal of comparing the results obtained in the two methods.

Another direction we pursued this year included the study of the sublimation of TNT micro-particles. These experiments were carried out using a Quartz Crystal Microbalance (QCM) apparatus to follow the sublimation process.

Accomplishments

AFM measurements: A very large number of measurements were carried out. These examined the adhesion of: PETN, RDX and HMX. The substrates considered in these measurements included: Glass, Stainless steel, polypropylene and four car paint coupons (obtained from the TSL laboratory). Most of the measurements were carried out at both ambient room conditions and under water. In addition to the evaluation of the adhesion forces we also calculated the Hamaker constants for these systems.

QCM measurements: Reliable measurements of non-uniform TNT micro-crystals layer sublimation rate was carried out using quartz crystal microbalance (QCM). The micro-crystal layer was precipitated from solution of TNT on the QCM electrode. It is shown that the kinetics of small TNT particles sublimation is controlled by the molecular diffusion in air. The sublimation process is well described by diffusion expressions discussed in literature for both individual micro-crystals and disk shaped sample layers. Based on the diffusion controlled model, expressions to describe the particle size evolution in time were derived including particles with size comparable to the mean free path in the gas phase.

Details

AFM measurements:

In figure 1 a typical approach and retraction route is shown for adhesion measurement of an explosive particle on a glass substrate. The vertical axis show degree of cantilever bending while the horizontal one the cantilever-substrate separation. The blue curve shows the approach route. It is clear the no significant deflection of the tip is obtained for large particle-substrate separations. When the particle approaches the substrate before contact is obtained, the Van der Waals (VDW) attraction overcomes the cantilever force that prevents it of bending and a sharp “jump-to-contact” of the particle and the substrate is observed. The magnitude and location of this “jump-to-contact” point serve to evaluate the magnitude of the VDW interaction and from it the

value of the corresponding Hamaker constant. Farther motion of the cantilever towards the substrate results in sampling the repulsive wall of the corresponding interaction. Along the retraction rout, red trajectory, the adhesion forces between the particle and the substrate lead to the bending of the cantilever to the other direction. Once the force that corresponds to the bending of the cantilever overcomes the adhesion force the tip “jumps” away from the substrate. The magnitude of this jump is related to the adhesion force/energy. It should be noted that while the “jump-to-contact” along the approach rout is only weakly dependent on the particle-substrate contact area, the magnitude of the adhesion force strongly depends on this contact area.

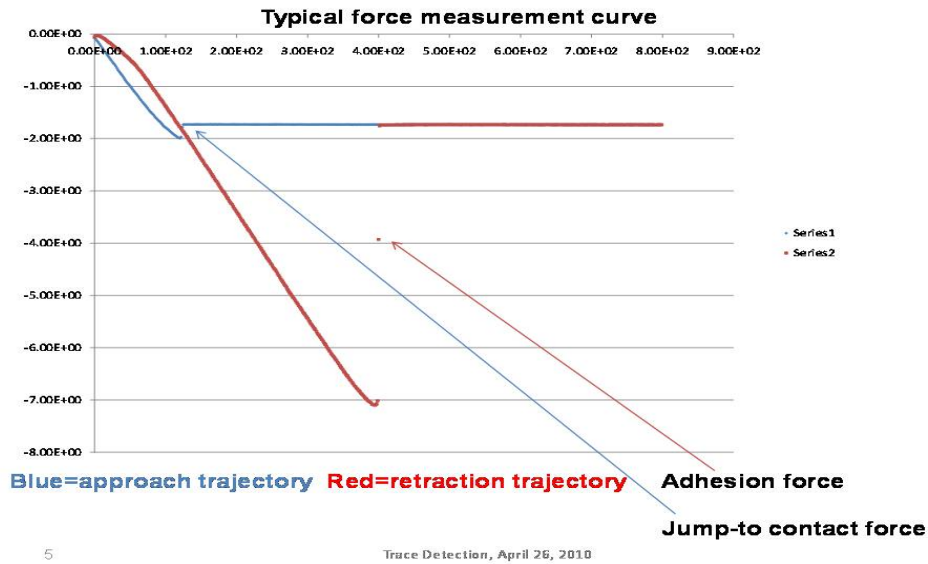


Fig. 1: Typical approach and retraction curve obtained in adhesion force measurement using AFM.

In figure 2 below we present the topography of the four different car paint coupons (CPC) obtained from TSL. The roughness of the substrate surface increases in the order: “Cream Metal” > “White Plastic” > “Black” and “Grey” metal. The last two substrates show very similar morphology while the first one, “Cream Metal” exhibits much larger roughness than the other three samples.

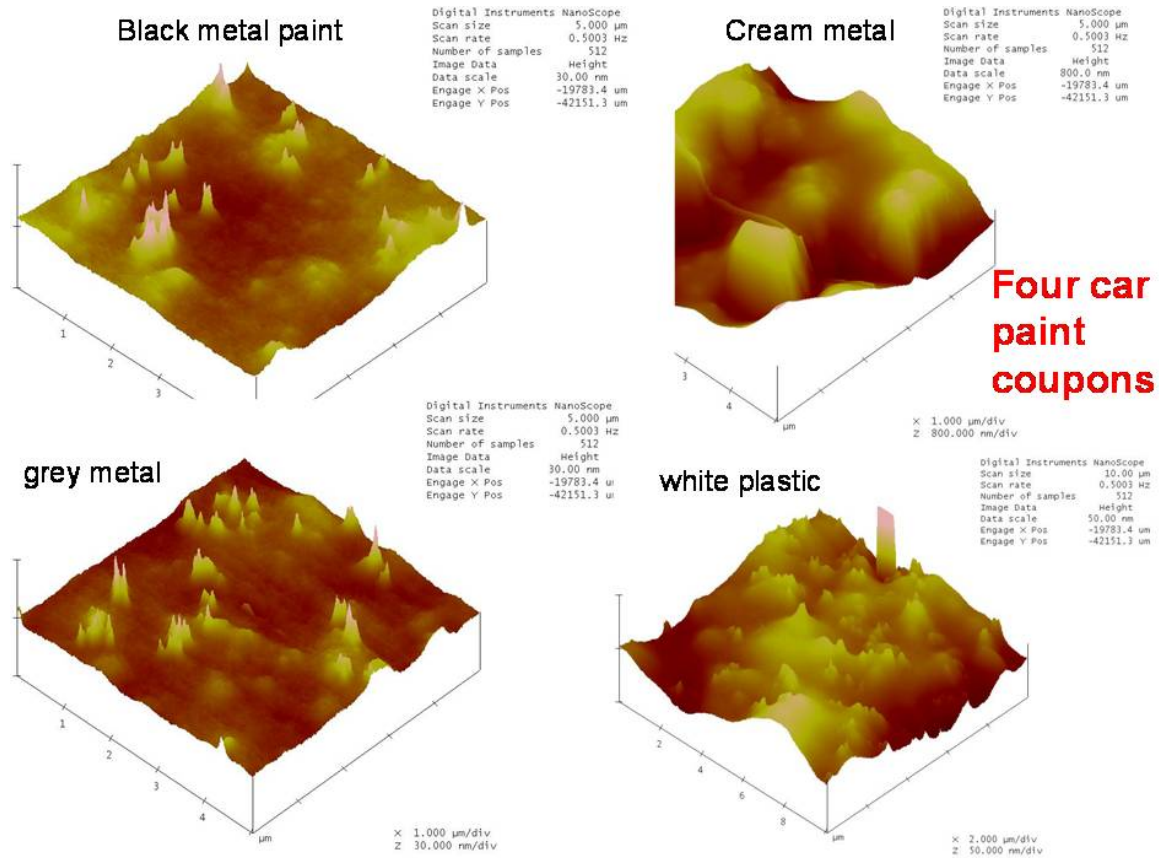


Fig. 2: AFM topographic scan results of the four car paint coupons.

Four typical force curves of two explosives on two different substrates are shown in Fig. 3. It is clear that the four curves show quite different behavior. This large variation forces us to carry out many measurements over different random substrate sites to be able to compare results. Such a comparison for the three explosive particles examined on the four CPC substrates is shown in Fig. 4.

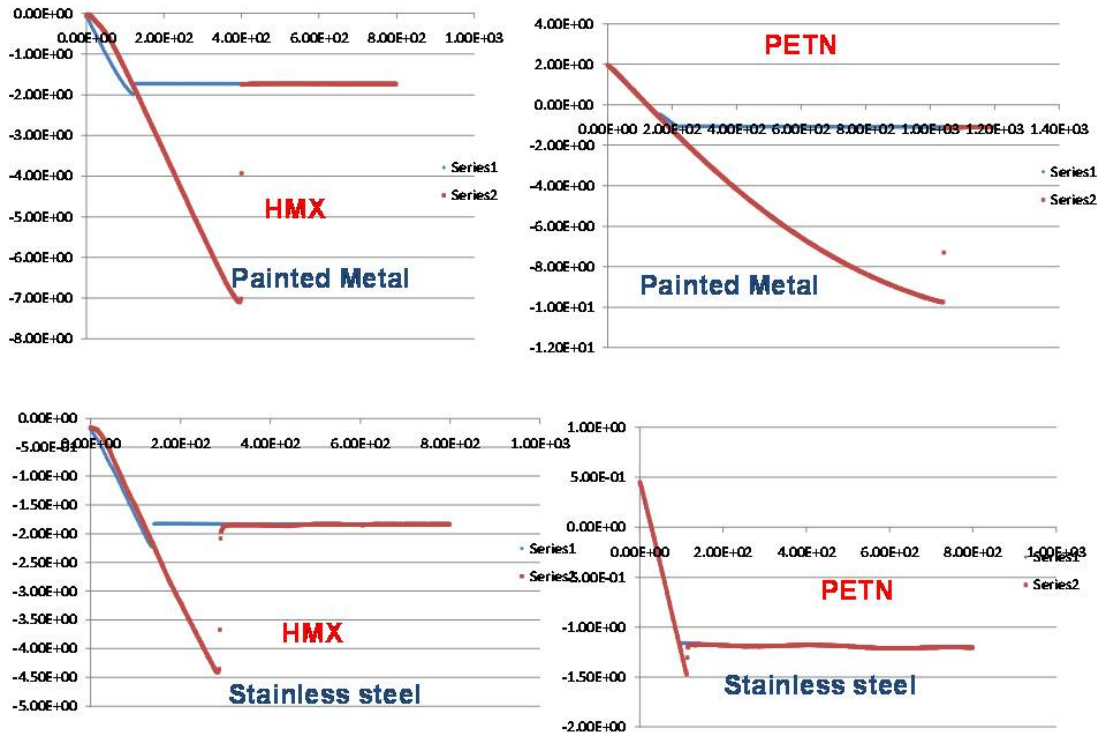
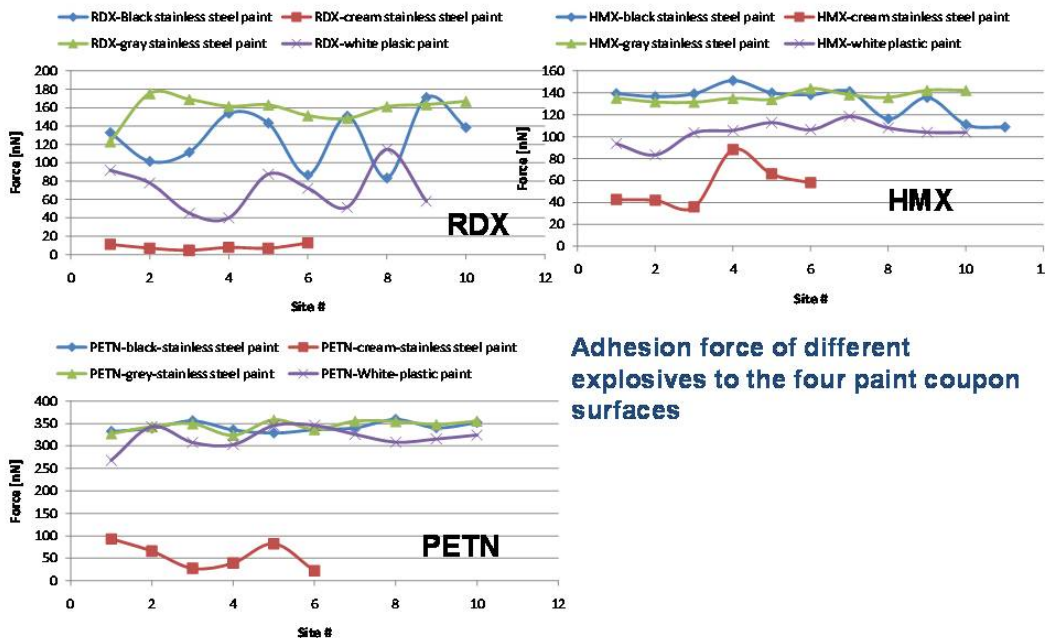


Fig. 3: Typical measurements of adhesion force curves for different explosive particles and substrates.

The data presented in Fig. 4 was obtained in adhesion measurements of about ten different random adhesion sites on each of the four CPC samples. It is clear that the adhesion force over different site may change in magnitude. We think these variations are mainly due to variations in the magnitude of “contact area” between the rough particle surface and the rough substrate site to which the particle is attached. There is no simple way we know off to measure this contact area, hence one is forced to carry out many measurements to obtain a characteristic average for the system studied.

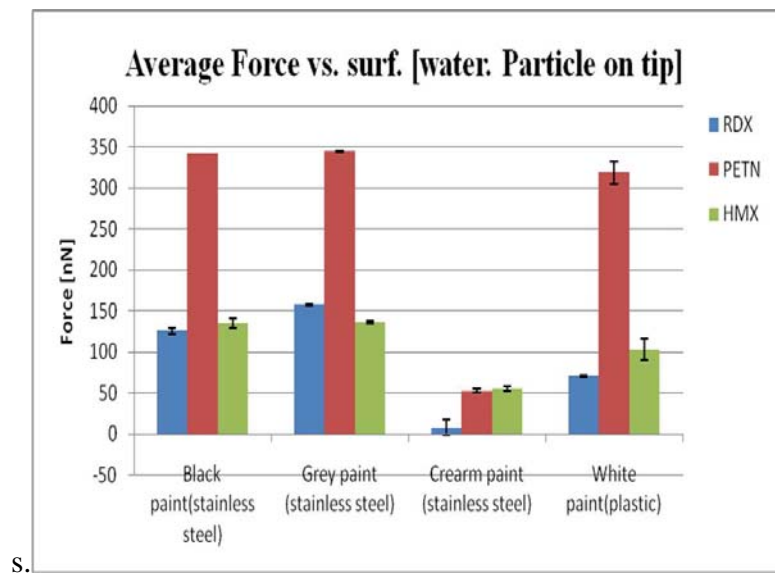
Inspection of these results shows clearly that the roughest substrate, “Cream Meta” exhibit the lowest adhesion force for all three explosives examined. In addition, is clear that the three different explosives show marked differences in the magnitude of the adhesion forces over the four CPC substrates. Note the vertical axis for PETN is quite different than that for RDX and HMX.



Surface roughness increases in the order:
Cream on metal >> White on plastic > Black and Grey on metal

Fig. 4: AFM of three explosive particles on the four car paint coupon surfaces.

The average adhesion forces for the three explosive on the four CPC are shown in Fig. 5 below. These results clearly indicate that the adhesion of PETN to there of the four CPC substrates is much stronger than that for RDX and HMX. In addition, the adhesion forces of all three explosives to the “Cream Metal” relatively rough substrate are much smaller than to the smoother substrate



S.

Fig. 5: Average adhesion forces of three explosives on the four CPC substrates.

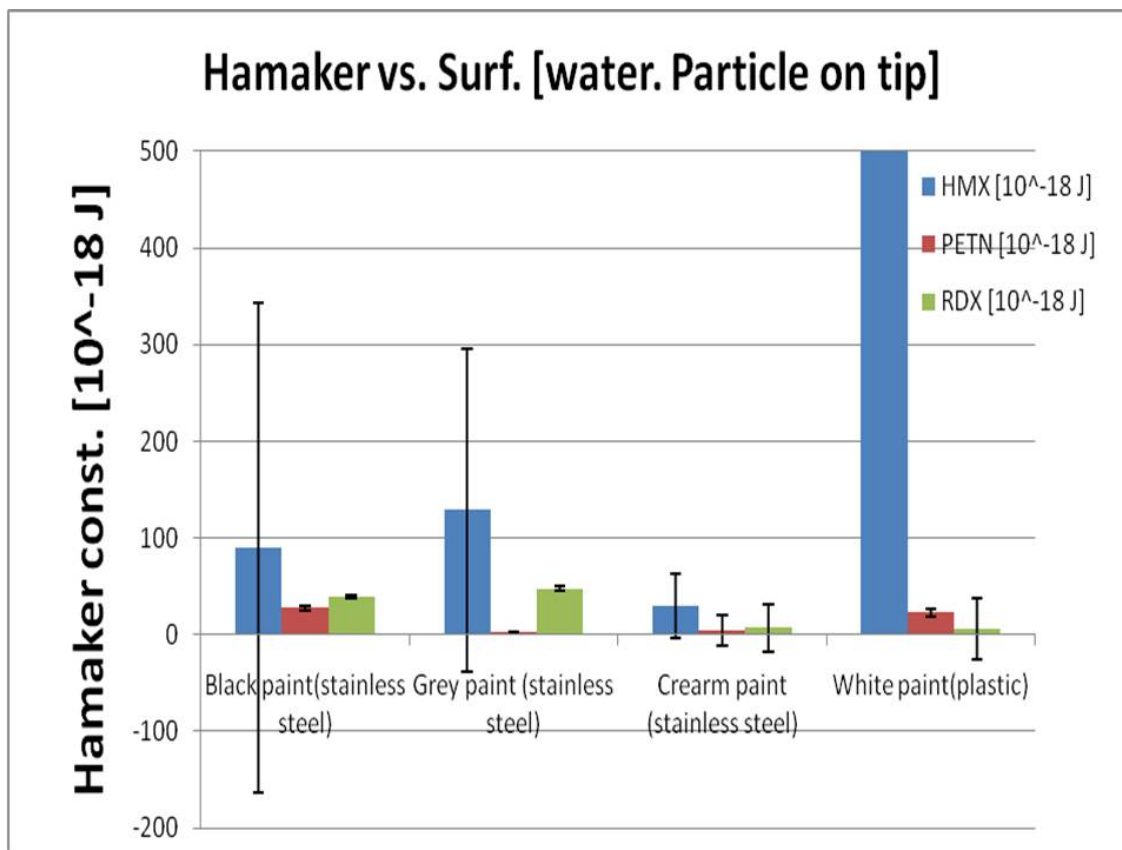


Fig. 6: Hamaker constant obtained for three explosives examined on the four CPC samples.

The adhesion curves were analyzed to obtain estimated for the Hamaker constant for these systems. Note that all these measurements were carried out in ambient air surroundings. The values obtained for the Hamaker constants show that HMX possesses the largest value on all four substrates examined, moreover, the values obtained exhibit marked differences. These values for the Hamaker constant of the systems investigated here can be used to model the interaction of such explosive particles with these types of substrates.

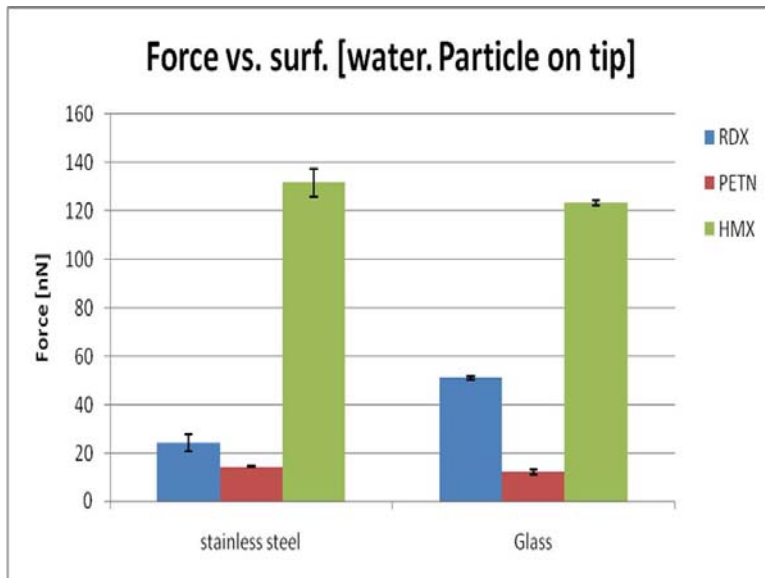


Fig. 7: Average adhesion forces (underwater) for 3 explosives on glass and stainless steel.

Figures 7 and 8 exhibit the average adhesion force obtained for the three explosive particles on a glass and stainless steel substrates. These experiments were carried out under water (Fig. 7) and in ambient air (Fig. 8). There is some difference between the two sets of measurements (water vs. air); however, the differences are relatively small. In both cases and on the two substrates HMX exhibits the largest adhesion force among the three explosives. RDX correspond in all cases to a slightly stronger adhesion force than PETN; however, the differences are quite small.

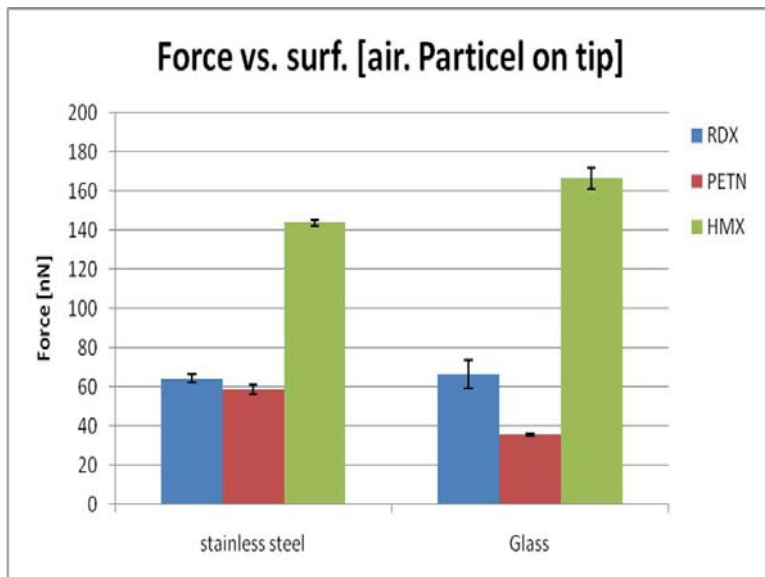


Fig. 8: Average adhesion forces (in air) for 3 explosives on glass and stainless steel.

The Hamaker constants for these systems are presented in Figs. 9 and 10 respectively. In all cases the Hamaker constant for HMX is much larger than those for RDX and PETN. However, a clear difference between measurements under water and in ambient air is seen. For all three explosives the Hamaker constant measured under water is larger than that obtained in ambient air

(by a factor in the range of 3-7). These differences are associated with the large differences in the dielectric constant of the medium under which the experiment was carried out.

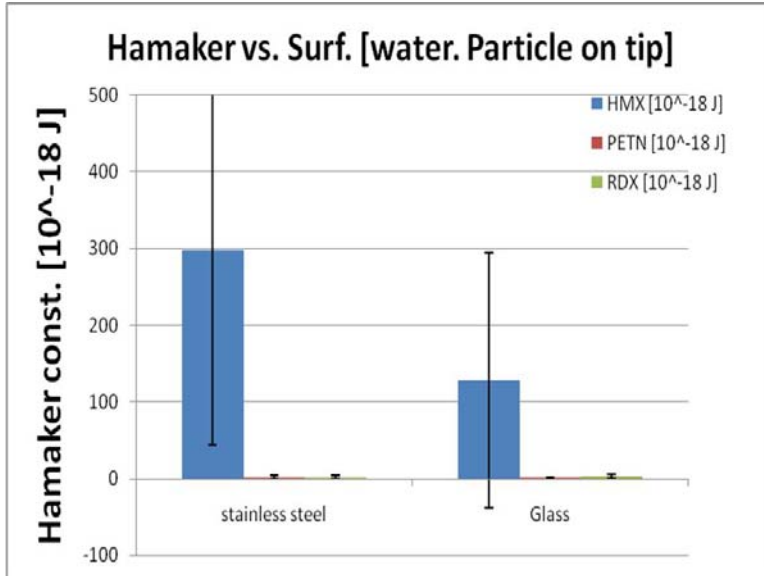


Fig. 9: Hamaker constants for the three explosives on Glass and Stainless Steel (SS) substrates. Measurements carried out under water.

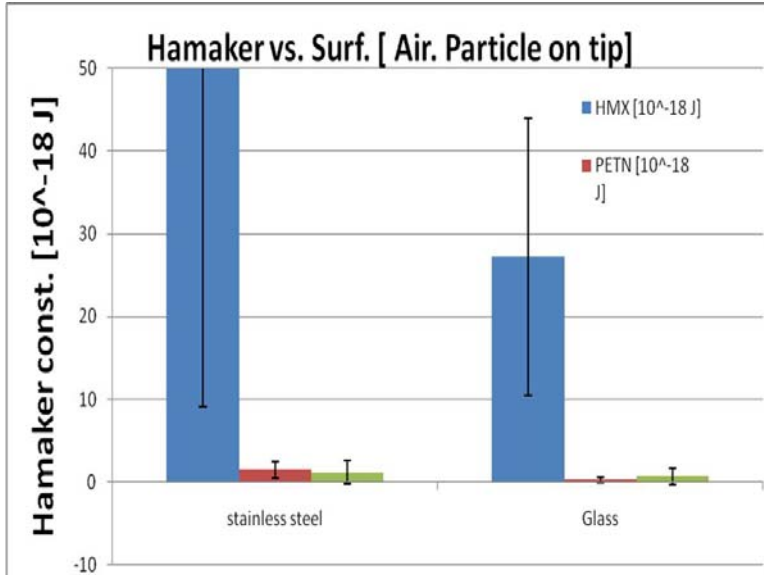


Fig. 10: Hamaker constants for the three explosives on Glass and Stainless Steel (SS) substrates. Measurements carried out in ambient air.

QCM measurements:

To be able to estimate the life time of explosive particles in ambient conditions we carried out sublimation experiments of explosive particles by following the variation in their weight using a

QCM. The first explosive studied was TNT. The samples were prepared by the deposition of a well defined volume of TNT solution in acetonitrile (2 mg/ml) onto the QCM sensor surface and evaporation of the solvent. The sample obtained constituted of well separated micro-crystals on TNT with radius of approximately 6 microns as shown in Fig. 11 below. We measured the height variation of these TNT micro-crystals using a light interferometer. A typical line scan is shown in Fig. 12 below. Analysis of the micro-crystal height variation shows that the average value is about 5.6 microns. Hence, most of the TNT micro-crystals in the sample have hemi-spherical shape with a radius close to 6 microns.

All the experiments were carried out in an oven with fixed temperature whose variation was up to 0.1 degrees and with air flow during the measurements. During the experiments we followed the sample weight variation.

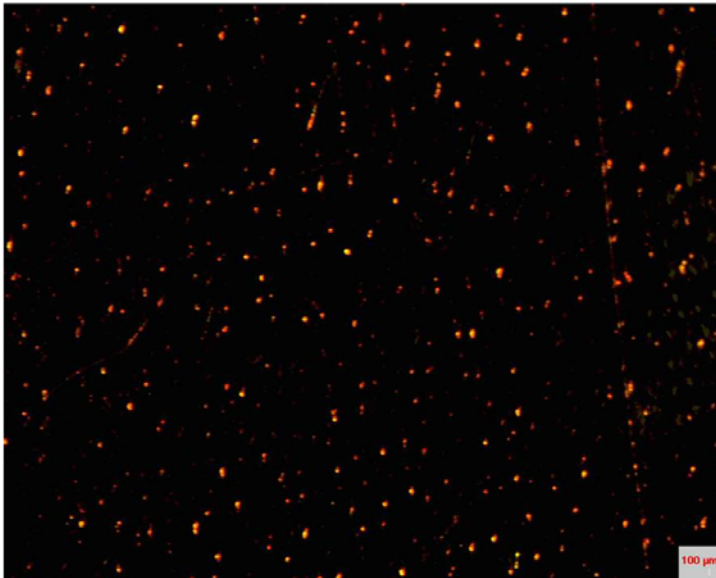


Fig. 11: Typical TNT sample for the sublimation experiments.

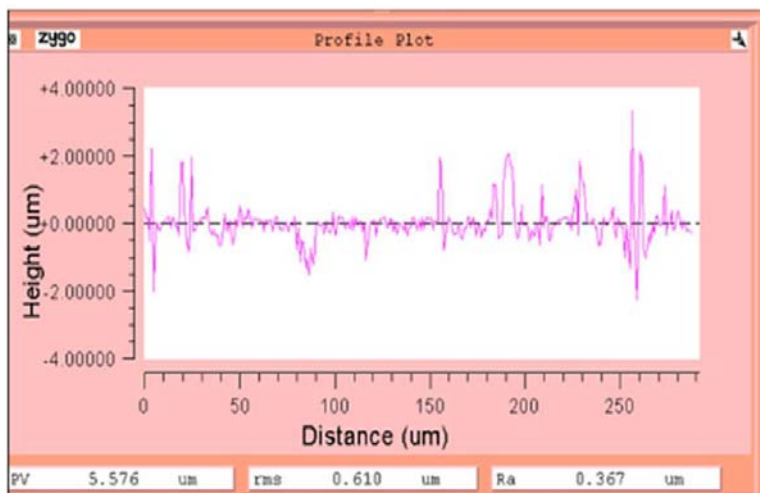


Fig. 12: A typical interferometer line scan along the QCM crystal surface.

The sublimation rates we obtained for TNT at four temperatures are shown in Fig. 13.

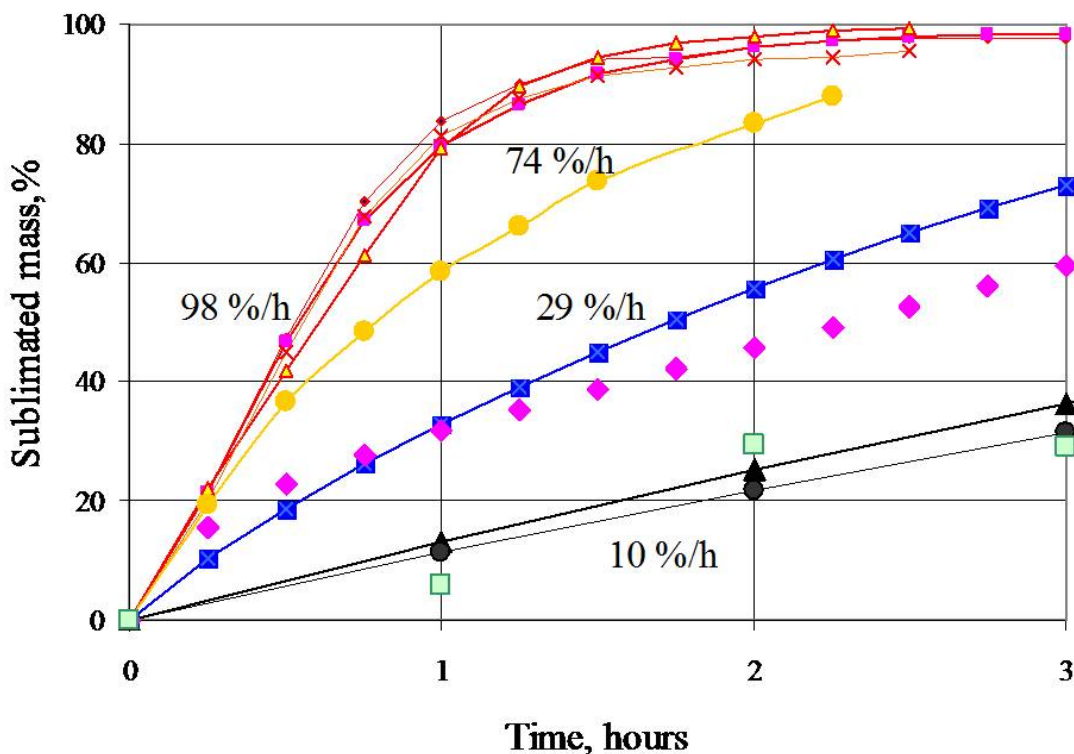


Fig. 13: Variation of TNT sublimation rates. Red lines at $T=50^{\circ}\text{C}$, yellow at $T=45^{\circ}\text{C}$, blue at $T=40^{\circ}\text{C}$, and black at $T=30^{\circ}\text{C}$. Magenta points = data obtained in experiment with the sample positioned in the vicinity of ventilation system of the oven green points correspond to data obtained in the experiment where analytical balance was used to follow weight fraction changes. Initial sublimation rates are noted near the curve of the different T values.

The mass fraction change during the sublimation process as measured by the QCM is shown in Figure 13 for four different temperatures. One should note two points: a) Measurements in which analytical balance was used to monitor weight change at 30°C confirms the reliability of the data obtained by the QCM. This substantiates the validity of evaporation rate measurements using the QCM. b) The relatively strong air flow induced by the oven ventilation system does not affect considerably the measured evaporation rate.

The reproducibility of the measurements at any given temperature is very good. This confirms the reliability of non-uniform layer measurements using QCM. Moreover, this result also suggests that the approach used here for sample preparation yield statistically very similar initial sample morphology.

The initial slope of the various curves is related to the evaporation rate of the sample. If one assumes an Arrhenius form for the temperature dependence of evaporation rates, the activation energy of the process can be obtained from the slope of the line shown in Figure 14. The value obtained for the activation energy associated with TNT sublimation is 96 kJ/mol . This value is very close to the value of the heat of sublimation 99 kJ/mol .

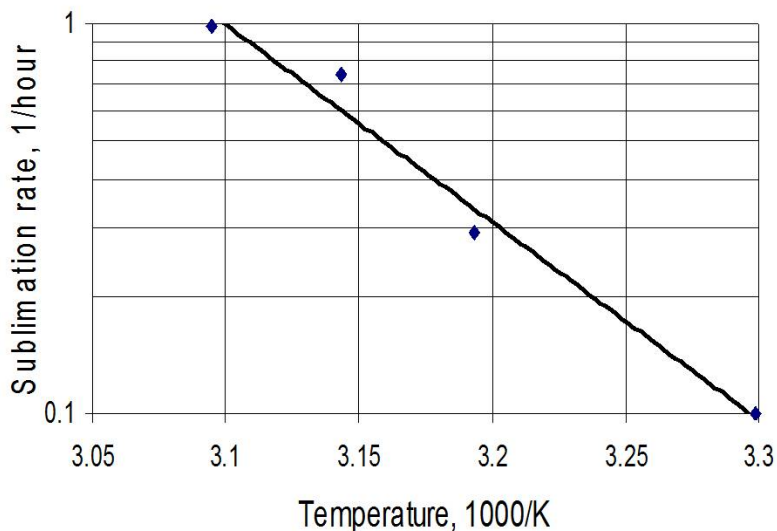


Fig. 14: Arrhenius plot of the initial sublimation rates.

We have shown that the rate limiting event is the diffusion of the sample vapor in air. A simple model was developed to describe well the evaporation rates. A full description is given in a paper sent for publication (see below).

Students Supported

Yevgeny Zakon – is a M.Sc. student who was partially supported during the last two years. He is writing his Master’s thesis at present. He carried out most of the AFM and Aerodynamics adhesion measurements.

Raya Zach – a retired technician who work in the lab 2-3 days a week. She is involved in the preparation of explosive coated particles. Raya is seen below near the stand alone DMS system.



Stella Reizelman – a M.Sc. student who was partially supported last year. She is mainly responsible to work related to the DMS and IMS. In the picture (right) Stella on the left and Mr. Yossi Matana (retired technician) on the right standing near the GC-DMS system.

Pas Elia – a new PhD student who will be involved with AFM measurements and IMS and DMS
Below is Paz near the particle-tip gluing system for the AFM system.



Arcady P. Gershanik – retired physicist who works 2-3 days a week and is partially supported.
Arkady carried out all the QCM measurements described.

Conference & Journal Publications

1. I participated and presented a talk in the Particle sampling meeting last April in Baltimore.
2. A paper on the TNT sublimation was submitted to the journal of physical chemistry.
3. A paper related to the AFM measurements is being written at present.

Optical Chemical Sensors using Nanocomposites from Porous Silicon Photonic Crystals & Sensory Polymers

William Euler, Igor Levitsky, S D. Brodeur, C. Latendresse, E. Hwang, Meredith Matoian

University of Rhode Island

Objective

Explosives sensors are being developed that are based on fluorescence quenching of a polymer deposited onto or into a porous substrate. The sensor sensitivity is by two mechanisms: amplification of the fluorescence decay by electronic communication along the conjugated polymer backbone and by choice of the large surface area substrate, which provides more opportunity for interactions with the analyte. The initial studies were motivated by collaboration with Emitech, Inc., which has built a breadboard prototype of a TNT sensor based on this



Figure 1. Handheld explosives sensors developed by Emitech, Inc.

technology, shown in Figure 1. The research goals are two-fold. First, optimization of the materials parameters used in the Emitech device. This includes understanding the role of the pore structure, the influence of the fluorescent material deposited into the pores, and development of multiple analytical techniques to assess the efficacy of the sensor platform. The second goal is to find new types of pore structures and new fluorophores that can be used to improve the sensitivity and selectivity of the device.

Accomplishments

For the porous silicon based sensors, the initial work has been in characterization of the fundamental properties of the sensor platform. New methods for determining pore size and depth using IR spectroscopy was established. This was extended to measuring the extent of pore-filling by the polymer fluorophore. Metrics for each of these parameters are being correlated with sensor performance so that a quick, nondestructive, and simple measurement with little sample preparation can be used for quality control of the sensor. Finally, the photochemical lifetime of the polymer was investigated. The useful lifetime of the sensor is limited by the total light exposure. Sacrificial additives have been synthesized and tested that lengthen the polymer lifetime without degrading the sensor performance.

Several new types of fluorescent sensor systems have been investigated. Sol-gel materials have been developed that can be used to incorporate a fluorophore. Sol-gels are an alternative to porous silicon because they can be used to design 3-dimensional porous structures, in contrast to

the 2-dimensional pores on etched silicon. Porphyrins have been examined as a new class of fluorophores and zinc tetraphenylporphyrin appears to be a promising candidate. We also have started to examine the polymer Nafion as a substrate for a sensing system. Nafion is naturally porous with pores that are surrounded by strongly acidic sulfonic acid groups. The initial work to exploit these features led to the design of a simple dosimetric sensor for amine type bases.

Details

The standard method to evaluate pore structure is to use microscopy. For the porous silicon based materials this viable but sample preparation is tedious. Figure 2 shows scanning electron micrographs (SEM) of two different porous silicon samples, one with large pores and one with small pores. The two types of samples are created using different electrochemical etching conditions (specifically, different current densities).

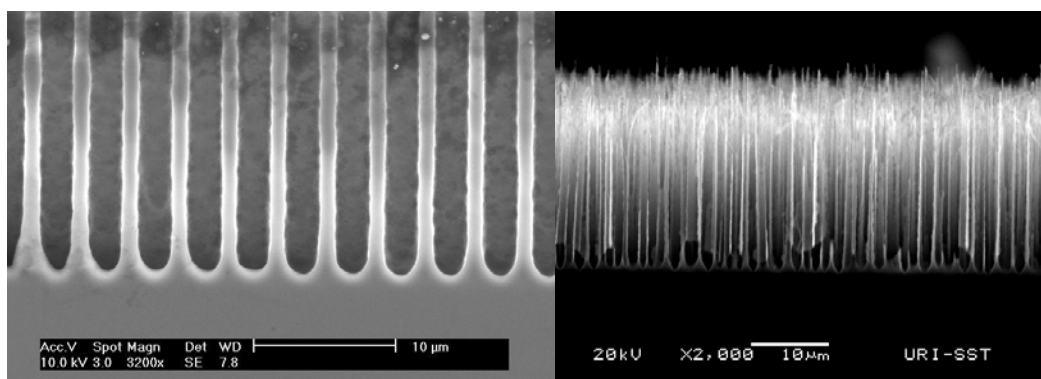
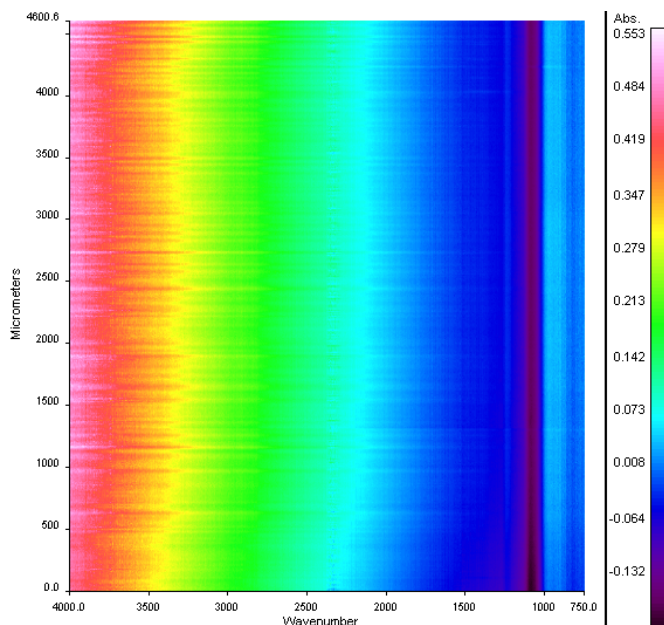


Figure 2. SEM images of two porous silicon samples using high current density (left image) and low current density (right image).



Chemical reaction with KOH can be used to estimate the porosity, as well. Simply using the mass of the porous area before etching, after etching, and after reaction with KOH (which completely removes porous silicon) allows a simple determination of the porosity. The SEM and chemical reaction methods give comparable results for the overall porosity and the depth of the porous layer.

In the working sensor, a fluorescent polymer (poly-5-methoxy-3-2-ethylhexyloxyphenylenevinylene, MEH-PPV) is

Figure 3. FTIR microscope image of porous silicon filled with MEH-PPV. The fine structure along the distance (y) axis shows the pore locations in the sample.

added to the pores. The MEH-PPV can also be used to characterize the pore structure using infrared microscopy. Figure 3 shows an FTIR microscope image of a porous silicon layer filled with MEH-PPV. Of particular interest is the “streaking” observed along the distance (y) axis. These fine structure features are assigned to the pore structure of the sample as interrogated by the depth of the MEH-PPV.

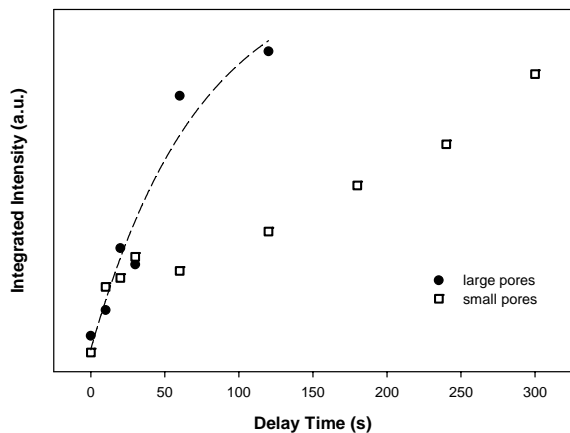


Figure 4. Integrated fluorescence signal of MEH-PPV as a function of residence time on a porous sample prior to spinning the solution off. Closed circles are for a large pore sample and open squares are for a small pore sample.

the solution off of the sample. The delay before spinning allows the polymer to penetrate into the pores for different times, thus effecting a depth profiling of filling. Figure 4 shows the integrated fluorescent signals for both large and small pores as a function of the residence time before spinning. The interesting result is that for both large and small pores a short residence time (less than 40 sec) has no effect on the amount of MEH-PPV deposited but at longer residence times the pore size becomes important. The mechanisms to explain these observations need to be determined.

The working sensor system detects TNT by quenching, i.e. the fluorescent signal decreases marked and rapidly in the presence of the analyte. One of the unique features of this sensor is that it also is able to detect RDX but not by fluorescence quenching but by a fluorescence enhancement. A comparison is shown in Figure 5. This means that the sensor can be used for

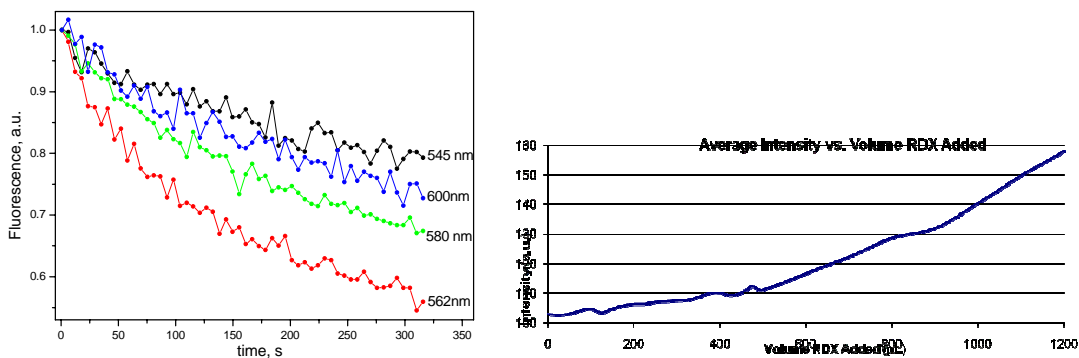


Figure 5. Fluorescent quenching by TNT (right) and fluorescence enhancement by RDX (right).

multiple explosives and distinguish between different types of explosives. The selectivity is readily monitored by the change (positive or negative) of the MEH-PPV emission.

One new type of sensor using Nafion as the porous substrate has been demonstrated. Nafion is doped with Rhodamine B, a fluorescent dye. In the presence of the strongly acid sulfonic acid groups in Nafion the sensor is light yellow/brown. Upon exposure to an amine base, the sensor changes to a bright pink color, as shown in Figure 6. The next step in the sensor development is

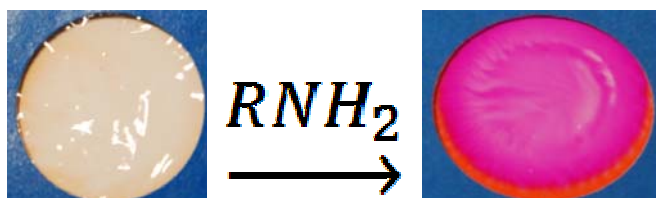


Figure 6. A Nafion sensor for amine bases. Left: in the absence of the analyte. Right: in the presence of methylamine.

to modify the chemistry in the Nafion pores to react with explosive molecules. Most explosives have nitro (NO_2) groups that can be reduced to amines (NH_2). If suitable chemistry can be found that can rapidly and reliably reduce nitro groups in the Nafion pores, then the ability to detect the amines is equivalent to being able to detect the original explosive.

Students Supported

Graduate Students

Drew Brodeur – porous silicon sensors

Christopher Latendresse – sol-gel fluorescent sensors

Undergraduate Students

Meredith Matoian – porous silicon sensors

Eunhae Hwang – Nafion sensors

Jungmin Hwang – quantum dot fluorescent sensors (a new direction)

Hyun Jeong “Christina” Yang – sol-gel fluorescent sensors

Publications

“Gas Phase Sensors for Bases Using Rhodamine B in Nafion Films,” Eunhae Hwang, Igor A. Levitsky, William B. Euler, *J. Appl. Polym. Sci.*, **2010**, *116*, 2425 – 2432.

A Persistent Surveillance Technique for the Detection of Explosives and Explosive Precursors

Prof. Otto Gregory, Michael Platek
University of Rhode Island

Objective

The detection of explosives and explosive precursors in suspected “bomb labs” and other enclosed areas that terrorists may target for the deployment of improvised explosive devices (IED) is the overall goal of this project. The significance of this work was first highlighted by the failed attempt of "Shoe Bomber" Richard Reid to deploy an IED based on triacetone triperoxide (TATP), with which he attempted to initiate an explosive device containing pentaerythritol tetranitrate (PETN). The ability to detect energetic materials at low concentrations in relatively confined spaces is particularly important in such scenarios. Therefore, the early detection of specific gas molecules without interference effects from background gases continues to be our goal. A robust sensor system must be sensitive enough to detect minute concentrations of the target gas, yet not generate false positives. Our initial focus this past year was on explosive precursors related to ammonium nitrate, specifically those compounds containing inorganic nitrates that are used in IED's. We have now identified catalysts and sensor templates that are tuned for ammonia and urea under pre-blast conditions. More recently our list of target molecules has been expanded to include hydrogen peroxide and TATP. The latter exhibits a sufficiently high vapor pressure that it can be detected directly in the gas phase. Because of the simplicity of its synthesis, TATP is an explosive of choice for terrorists. Thus, the early detection of TATP and isolation of such individuals is essential to the security of the general population.

Accomplishments

We are reporting the unambiguous, high-sensitivity detection of TATP for the first time using our current sensor template. Since high purity, crystalline TATP is available from the Energetic Materials Lab in the URI Chemistry department, controlled experiments for the detection of TATP in our laboratory is now possible. Nanogram quantities of TATP have been fixed in filter paper to enable the safe handling of this explosive. Based on its vapor pressure at room temperature, levels in the 8 ppm range in the gas phase have been achieved. A number of metal oxide catalysts have been successfully used to detect TATP at these levels, shown in Figure 1. Since we have recently demonstrated that we can detect hydrogen peroxide at comparable levels using the same metal oxide catalysts, we have compared the TATP and peroxide responses to determine if the TATP has been decomposing in the vicinity of the microheater during detection. The responses of V_2O_5 and SnO catalysts to TATP and peroxide are shown in Figures 2 and 3. It appears that the response of each catalyst to these target molecules occurs at the same temperature and the signatures have a similar shape. Therefore, since our gas sensor can detect hydrogen peroxide or hydrogen peroxide derived from TATP decomposition equally well, it may prove to be advantageous in some venues. Earlier in the program, we were able to detect acetone using CuO and FeO catalysts with some success and thus plan to do additional testing of acetone using V_2O_5 and SnO as well as other transition metal oxide catalysts. Since much of our effort has been on catalyst development as well as data compilation protocols, these experiments will enable us to accomplish our goal of early detection without interference effects. The active sensor elements in our various templates are thermally scanned using controlled input power. The power difference between a reference microheater and a catalyst-coated microheater has been detected as a function of temperature; i.e. by measuring the power required to maintain the temperature of the sensor relative to a reference microheater in the absence of a catalytic reaction. Thus, our technique measures the differential power response or thermodynamic response and not a response based on the electrical conductivity changes or associated electrical resistance changes of the catalyst upon exposure to the target gas. Unlike some sensor platforms where the metal oxide serves as both a transducer and a receptor, these functions are “separate” in our sensors, which are based on micro-differential thermal analysis. Thus, our “thermodynamic” sensors are not limited by operational temperature or electrical properties of the metal oxides. To date we have

investigated V_2O_5 , CoO_2 , CuO , FeO , SnO , SnO_2 , NiO and WO as catalysts for the detection of ammonia, urea, hydrogen peroxide and TATP, the results of which are summarized in Table 1. Table 1 shows that SnO may be considered a non-specific catalyst in that it responds to all target gases tested to date, however, the light-off conditions and signatures are unique. Thus, we have started a series of experiments to combine the responsiveness of the SnO catalyst with the specificity of a transition metal oxide catalyst to form a much more responsive catalyst using combinatorial chemistry techniques.

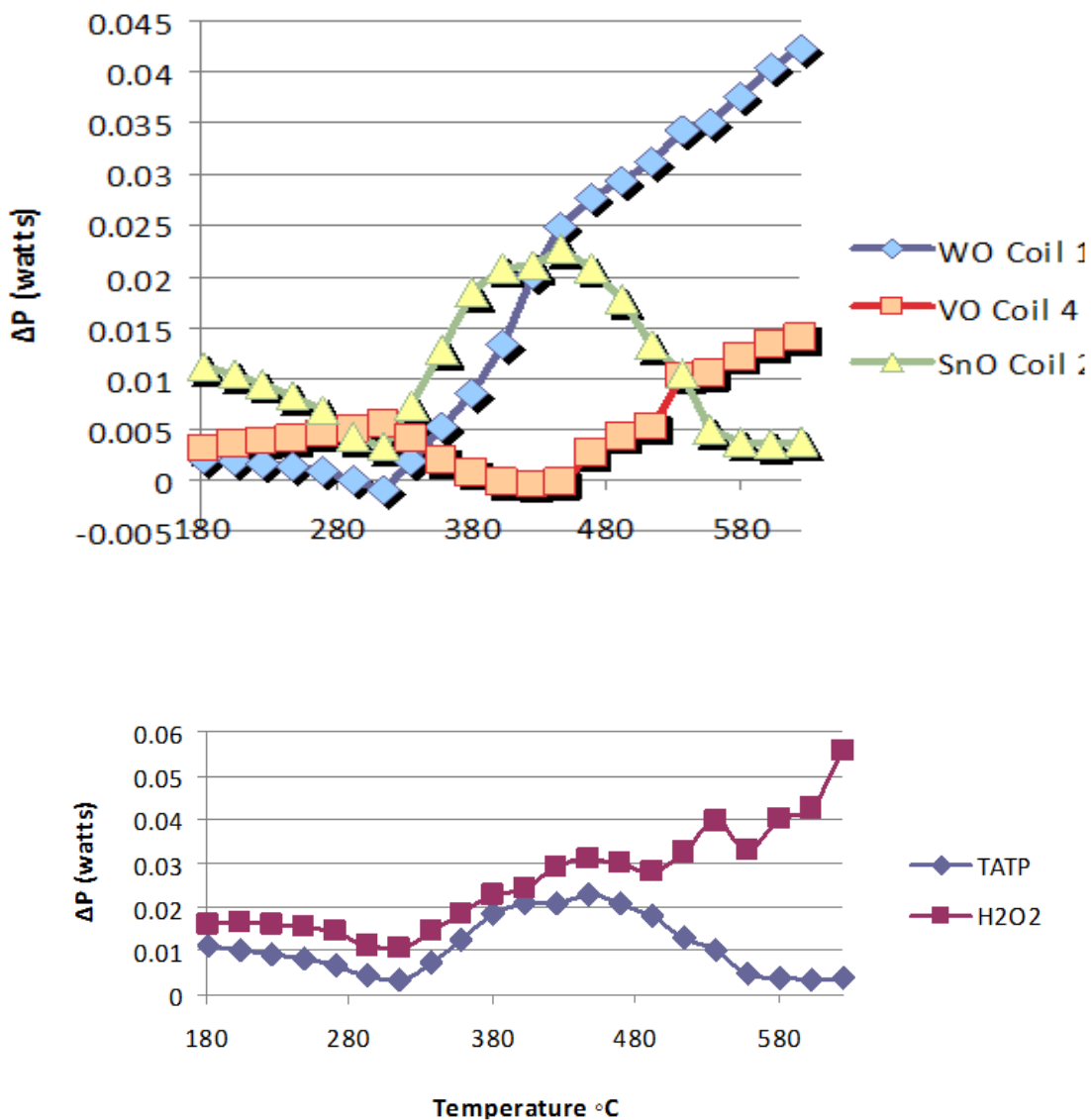


Figure 2. Response of SnO catalyst to 8 ppm TATP and 11 ppm hydrogen peroxide.

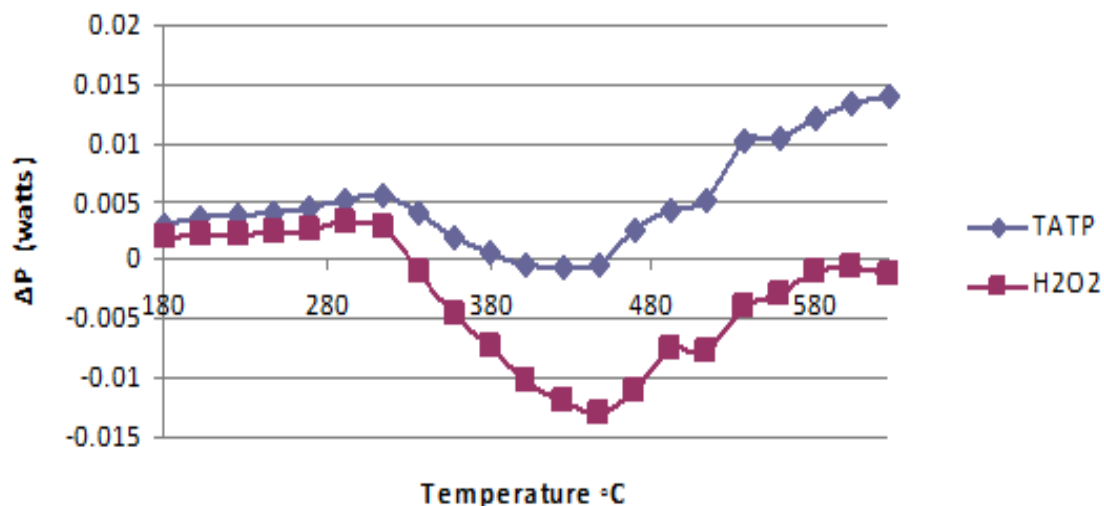


Figure 3. Response of V₂O₅ catalyst to 8 ppm TATP and 11 ppm hydrogen peroxide.

	Target Gas				
	NH ₃	NO ₂	H ₂ O ₂	Urea	TATP
AgCoO	Yes	No	No	No	incomplete
CuO	Yes	No	Yes	Yes	incomplete
FeO	Yes	Yes	incomplete	incomplete	incomplete
NiO	No	No	Yes	No	incomplete
SnO	Yes	Yes	Yes	Yes	Yes
SnO ₂	Yes	No	Yes	Marginal	incomplete
VO	No	No	Marginal	No	Yes
WO	Yes	Yes	Marginal	No	Yes

Table 1. Responses of various metal oxide catalysts to selected target gases.

Details: Two different sensor templates have been used to detect specific explosives and explosive precursors, the results of which are summarized in Table I. One template has utilized a coil based microheater and the other has utilized a thin film microheater that has been deposited on an alumina substrate to form a solid state sensor, shown in Figure 4. In this figure, a finished solid state sensor in a connector is shown ready for testing, as well as an alumina plate containing an array of sensors patterned for metallization. Combinatorial libraries are typically prepared on these sensor arrays containing nickel microheaters formed on individual alumina plates using microlithography techniques. In this way, the sensor elements can be snapped from the perforated alumina plate and mounted in a connector (Figure 4) for insertion into the mass flow controlled gas delivery system. In this way, various material combinations are achieved by co-sputtering to form individual sensors with unique chemistries. Such configurations have been extremely useful for rapidly screening catalyst combinations. These sensor platforms differ considerably in terms of robustness, with the solid state sensor being a much more robust platform. The

speed and accuracy also differ as well as the time constant for the two platforms. Therefore, we are working towards a platform that combines the best features of each; the MEMS based platform that is described at the end of this report. The solid state sensor platform is very similar to the MEMS based devices in many ways and also serves as a vehicle to provide engineering design criteria for the MEMS template.

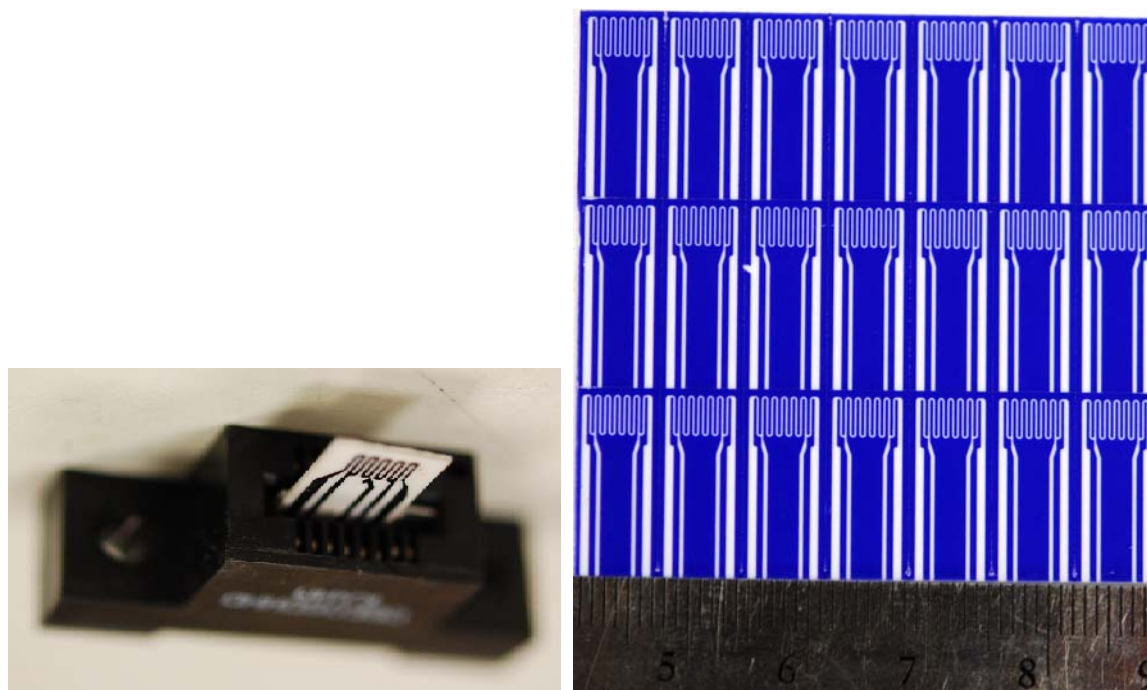


Figure 4. Photos of the solid state sensor platform used for catalyst screening & combinatorial chemistry. Left is the sensor packaged in a connector; right, an array of solid state sensors ready for metallization.

The bulk of the sensors used to screen the various metal oxide catalysts were the coil based microheaters. Scanning electron microscopy (SEM) was used to characterize the coverage of the various catalysts on the microheater surfaces before and after exposure to the target molecules. Figure 5 below shows that the surface morphology varies with the particular catalyst deposited on the microheater surface. From the micrographs it can also be seen that the surface roughness and coverage vary considerably from catalyst to catalyst. The catalysts have been sputter-deposited onto the microheaters to form libraries of microstructures has been established for each catalyst/target molecule pair to determine if changes have taken place in the microstructure as a result of exposure to the different molecules.

The selectivity of the different catalysts for different target gas molecules (even closely related ones such as NO_2 vs NH_3) was systematically investigated. Sensor response to similar concentrations of NO_2 and NH_3 show very different behavior in terms of sensitivity to the target molecules using the same catalyst as shown in Figure 6 below. Here the ammonia response is quite large for the SnO catalyst but almost no response was observed for NO_2 (within the noise floor of the instrument) using the same SnO catalyst over the same temperature range.

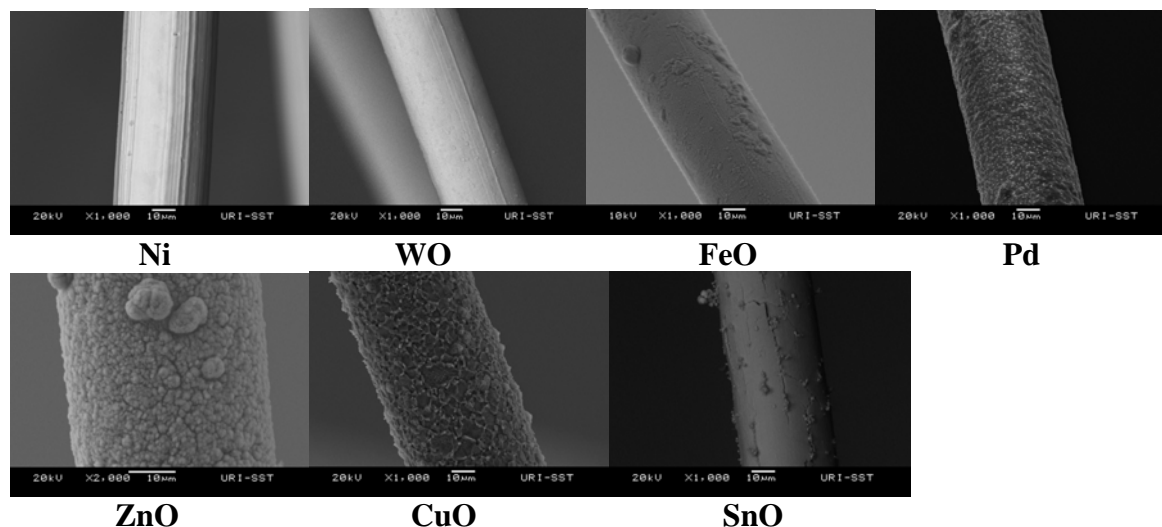


Figure 5. SEM micrographs of various metal oxide catalysts on a microheater support.

Discrimination by two different catalysts to the same target gas can be seen in Figure 7, where NH_3 was used as the target gas. Here the V_2O_5 catalyst and SnO catalyst have very different responses; i.e. the sign of the response is different for each catalyst, suggesting that the response for one catalyst is endothermic while the response for the other catalyst is exothermic. Catalyst selectivity was also preserved here as indicated by the peaks occurring at different temperatures and the light off conditions being shifted with respect to the different metal oxide catalyst. The response of tin oxide catalyst to 36 ppm urea is shown in Figure 8. It was one of only a few catalysts that responded to urea. In fact, SnO responded to all of the target gases tested to date.

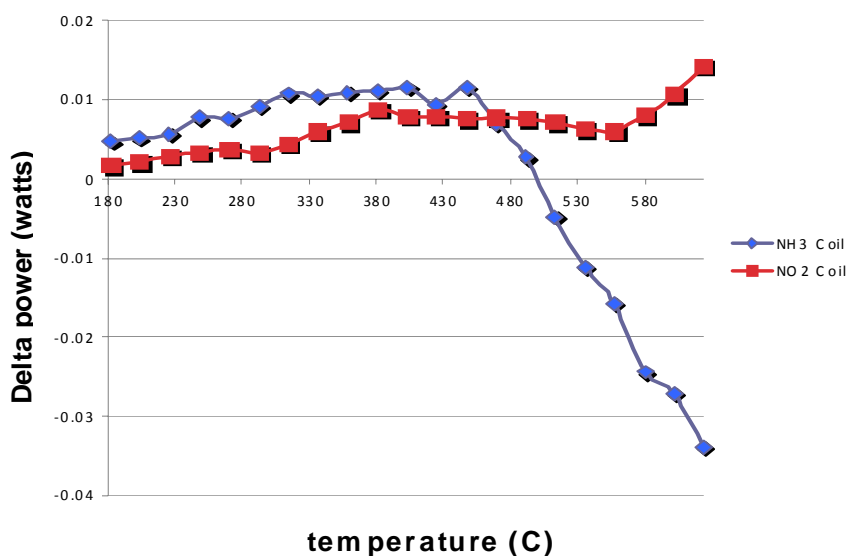


Figure 6. Response of the tin oxide (SnO) catalyst to 7450 ppm ammonia (NH_3) at 113.9 sccm flow and 7450 ppm nitrous oxide at 113.8 sccm flow

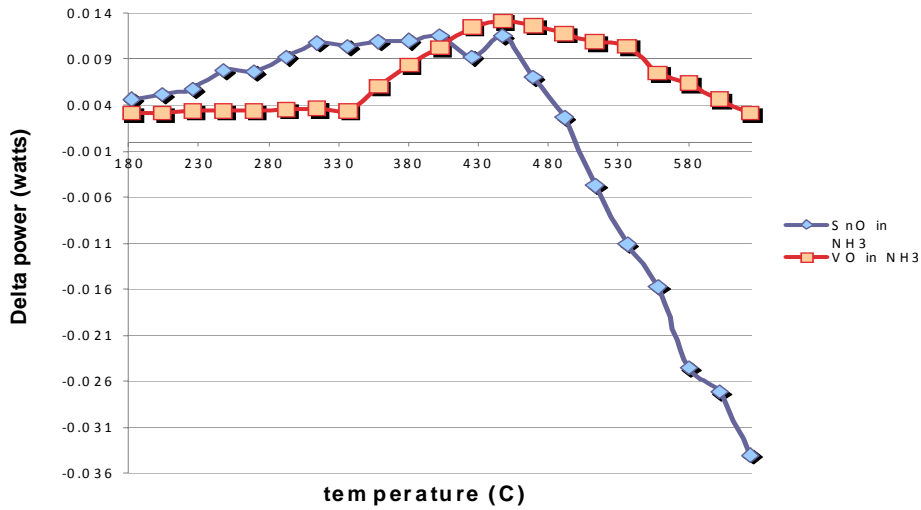


Figure 7. Response of a tin oxide (SnO) catalyst and a vanadium oxide (V₂O₅) catalyst to 7450 ppm ammonia (NH₃) at 113.9 sccm flow

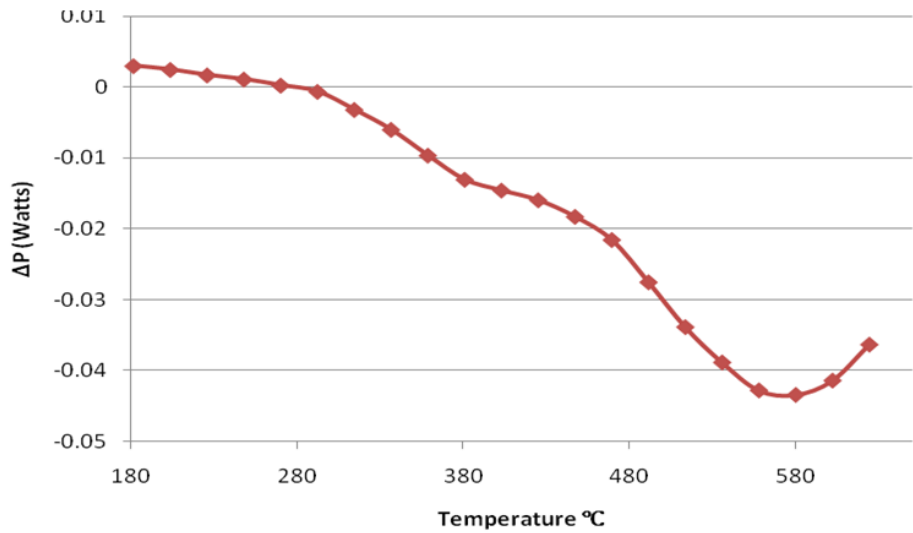


Figure 8. Response of a tin oxide (SnO) catalyst to 36 ppm urea at 100 sccm flow

MEMS/IC Integrated Detector: *What we can reach next year*

The design and fabrication of arrays of microheater based sensors containing multiple catalysts is currently being pursued with the US Navy (NUWC), in Middletown, RI. These sensor arrays will use

pattern recognition or equivalent electronics to check against a self contained library that will eventually be integrated into a MEM's platform to provide real time detection of a large number of threat indicator molecules. Working with Dr. Alan Davis and other engineers from NUWC, we have already taken steps to develop a MEM's based prototype sensor which will eventually be fabricated into these sensor arrays. The first designs or layouts on silicon have been completed and delivered to a MEM's foundry for fabrication. We are anticipating delivery of the die in August 2010. The ultimate goal is to implement the MEM's based sensors and associated electronics (IC) on a CMOS die (and later on SiGe BiCMOS die) to include the heater, isolated platform for the catalytic reaction and temperature measurement via infra-red sensors. The microheater (thin film serpentine) was placed in the center of a 1.5mmX1.5mm die and the IR detector and electronics will be placed on the periphery (Figure 9: Top View). The SWNT and metal oxide catalyst will be deposited on the passivation layer over an area of 1 mm². The microheater element is fabricated out of a top-level metallization and the substrate under the microheater becomes the sacrificial layer (Figure 9: Side View). Removal of the silicon under the microheater provides the isolation necessary to incorporate both the microheater and semiconductor circuits on the same die. There are two possibilities for IR detection, the first is to deposit a pyroelectric material such as AlN [6] shown in Figure 9. Passivation cuts must be made here in order to contact the pyroelectric IR sensor. A second approach employs a SiGe diode. It is possible that there will be sufficient detection at MWIR/LWIR wavelengths when the IC is fabricated using the SiGe BiCMOS process.

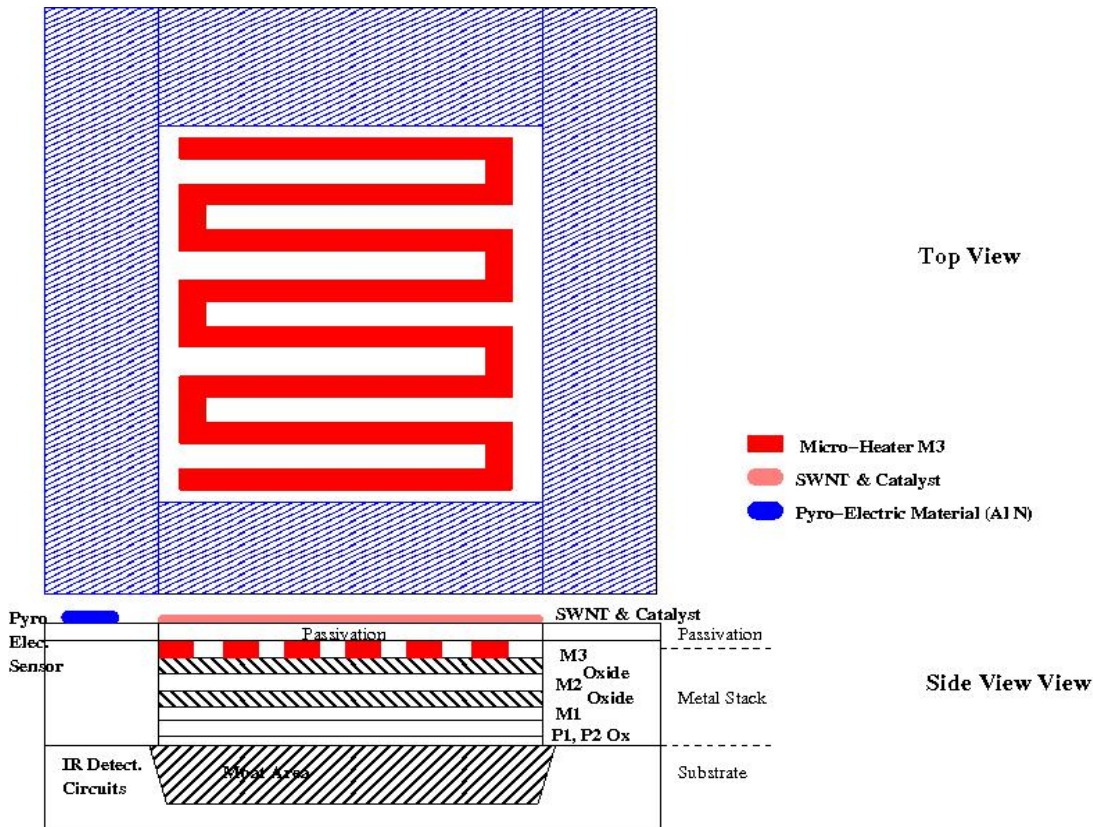


Figure 9. Design of a MEM's based sensor complete with a microheater and isolation platform for the catalytic reaction



Undergraduate Students Supported by the DHS Project

Caitlin Hurley; Chemical Engineering major
 Kellie Waterman; Chemical Engineering major
 Bruce Schaller; Chemical Engineering major

Graduate Students Supported by the DHS Project

August Cote; Electrical Engineering PhD student
 Yun Chu; Chemical Engineering PhD student
 Tom Hilfer; Chemical Engineering MS student

Papers and Posters

“A Persistent Surveillance Technique for the Detection of Explosive Precursors”, Caitlin Hurley, Matin Amani, Bruce Schaller, Mike Platek, Otto Gregory
 October 2009 Dept. of Homeland Security Workshop at URI

“A Persistent Surveillance Technique for the Detection of Explosive Precursors”, Caitlin Hurley, Matin Amani, Bruce Schaller, Mike Platek, Otto Gregory
 March 2010 Dept. of Homeland Security Review at URI

References

1. H. Nanto, T. Minami, and S. Takata, K. J., “ZnO thin film ammonia gas sensors with high sensitivity and excellent selectivity”, *J. Applid Physics*, 60(2), 15 p.482 (1986).
2. M.S. Wagh, G.H. Jain, D.R. Patil, S.A. Patil, L.A. Patil, “Modified zinc oxide thick film resistors as NH₃ gas sensor”, *Sensors and Actuators B*, 115, p. 128–133, (2006)
3. M. Aslam, V.A. Chaudhary, I.S. Mulla, S.R. Sainkar, A.B. Mandale, A.A. Belhekar, K. Vijayamohan), “A highly selective ammonia gas sensor using surface-ruthenated zinc oxide”, *Sensors and Actuators*, 75, p.162-167 (1999)
4. G.S. Trivikrama Rao 1, D. Tarakarama Rao, “Gas sensitivity of ZnO based thick film sensor to NH₃ at room temperature”, *Sensors and Actuators B*, 55, p.166-169 (1999)
5. G. Uozumi, M. Miyayama, H. Yanagida, “Fabrication of CuO-infiltrated ZnO composite and its gas sensing properties”, *J. Mater. Sci.*, 32, (11) 2991–2996 (1997).
6. E. E. Crisman, J. S. Derov, A. Drehman, O. J. Gregory, “Large Pyroelectric Response from Reactively Sputtered Aluminum Nitride Thin Films”, *J. Electrochemical Society, Electrochemical and Solid State Letters*, Vol. 8, Issue 3, pp A141-L1, (2005).
7. “Gas Sensor Apparatus”, August 5, 2008, O.J. Gregory, A.H. Mengel, D.R. Flanders and M.B. Feick, US Patent No.7,408,158.

Fragmentation of Gas Phase Ions of Simulants & Explosives in Air at Ambient Pressure;

Gary A. Eiceman

New Mexico State University

Objectives

A main objective of these studies has been to add previously unavailable physical or chemical properties of explosives- the rate of decomposition of gas phase ions of explosives at ambient pressure. Such parameters underlie the performance of existing measurement devices and fix fundamental limits on detection and serve as the foundation for future methods of chemical detection. Our goal was to establish a data base with systematically reported and documented kinetics of decomposition of explosive ions. We had previously shown that ion kinetics could be obtained with ion mobility spectrometers specially designed and operated to obtain kinetic measurements. This effort has been comprised of three stages: a. Instrument building; b. validation of the measurements using standards; c. studies with explosives. We have completed stages a and b and are in progress in stage c. In addition, we explored how energy from a high electric field enters an ion and is distributed and absorbed using a differential mobility spectrometer.

Introduction

Ions of explosives, found initially as adducted species such as M^+Cl^- where M is the molecule electro-statically. The adduct ion in trace detectors or atmospheric pressure ionization mass spectrometers can remain for 10 ms or longer as the adduct or, depending upon the explosive can undergo dissociation to $M + Cl^-$ or can undergo hydrogen abstraction to $[M-1]^+ + HCl$, or can undergo fragmentation. The simplest of these, dissociation to Cl^- , or in the instance of positive ion chemistry M_2H^+ going to $M + MH^+$, has been explored at NMSU and methodology developed to obtain rate constants for ion behavior in air at ambient pressure.¹ This had never been achieved before our work and today is significantly underdeveloped. In virtually all or the kinetic studies and literature referenced energetic parameters, positive ion chemistry with carbonyl groups were reported.

In studies sponsored exclusively from the Center of Excellence, we built a new and improved kinetic IMS, and validated the methods and new instrument.²⁻⁴ During the latter half of 2010, we refined further the kinetic IMS (Figs 1, 2) and explored the behavior of explosives using the refined kinetic instrument.

Summary of kinetic studies

We validated the kinetic experiment using ketones and were within a few percent error of heats of associations, acceptable for this work. So far we have discovered that the explosives decompose, dissociate, and fragment simultaneously. We had anticipated this⁵, but have been forced to accept that our Faraday plate ion detector for the kinetic IMS in Figures 1 and 2 needs to be replaced by a mass spectrometer. At the beginning of Summer 2010, we are modifying our IMS to allow mass analysis of ions during the kinetic experiment.



Fig 1. Kinetic ion mobility spectrometer inside oven so all components within 1C.



Fig 2. Entire kinetic IMS apparatus to measure rates of decomposition of explosives.

In the study of ions under high electric fields using a commercial differential mobility spectrometer, we published two manuscripts and discovered that energy flow into ion of high mass differs significantly from flow of field energy into ion internal energy with low mass ions. We saw dissociation and decomposition as shown in Figure 3 and in the manuscript entitled: "Gas Phase Fragmentation of Protonated Esters in Air at Ambient Pressure through Ion Heating by Electric field in Differential Mobility Spectrometry", we reported. A planar differential mobility spectrometer has been used to study the ions formed at atmospheric pressure by a series of n-alkyl carboxylic acid esters (M). MH^+ and M_2H^+ ions were present at low temperature. The combination of thermal energy and energy derived from collisional heating by acceleration in the asymmetric electric field caused ion decomposition at an effective temperature (T_{eff}) higher than ambient. The products were the protonated carboxylic acids F^+ . The electric field thresholds for the first observation of F^+ decreased as the ambient temperature was increased. The rate $1.5^\circ C$ per Townsend, was the same for all esters; however, there was a measurable mass dependence. The higher the molar mass for the ester of a given acid, the higher the required field. Although MH^+ is the well-established precursor of the protonated acid, an apparent direct formation of F^+ from M_2H^+ was observed even though no MH^+ was present in the spectrum. This is ascribed to T_{eff} being mass dependent. A field sufficient to raise a M_2H^+ to T_{eff} for dissociation to $MH^+ + M$, raises MH^+ to a higher T_{eff} , leading to its immediate decomposition.

While the esters and explosives showed fragmentation, we were not able to obtain reliable data for simple dissociation (Fig 4). For this we used ketones, publishing "A determination of the effective temperatures for the dissociation of the proton bound dimer of dimethyl methylphosphonate in a planar DMS:" "The dissociation of the proton bound dimer of dimethyl methylphosphonate to the protonated and neutral molecule has been studied in a planar differential mobility spectrometer. The internal energy of the ions is the sum of the thermal component and electric field component and results in an effective temperature, T_{eff} , that is significantly greater than ambient atmosphere temperature (T). The measured rate constant for dissociation, which rises exponentially with field strength, together with activation energy and pre-exponential factor previously determined under thermal conditions, allow calculation of T_{eff} as a function of electric field strength. T_{eff} is a linear function of electric field intensity at constant T over the range of T from $60^\circ C$ to $140^\circ C$. The efficiency of the available collision energy in causing dissociation decreases with increasing T, from 52% at $60^\circ C$ to 40% at $140^\circ C$.

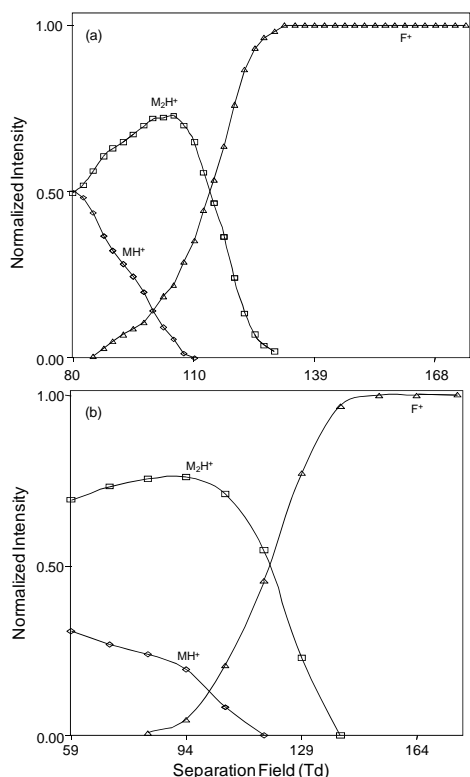


Fig 3. Normalized ion intensities of propyl acetate from (a) DMS (b) DMS/MS at a DMS temperature of 100°C. MH^+ ($CH_3COOC_3H_7$) H^+ , M_2H^+ ($(CH_3COOC_3H_7)_2H^+$), fragment $CH_3COOH_2^+$ normalized to total ion intensity, against DMS field (MH^+ diamond; M_2H^+ , square; fragment, triangle).

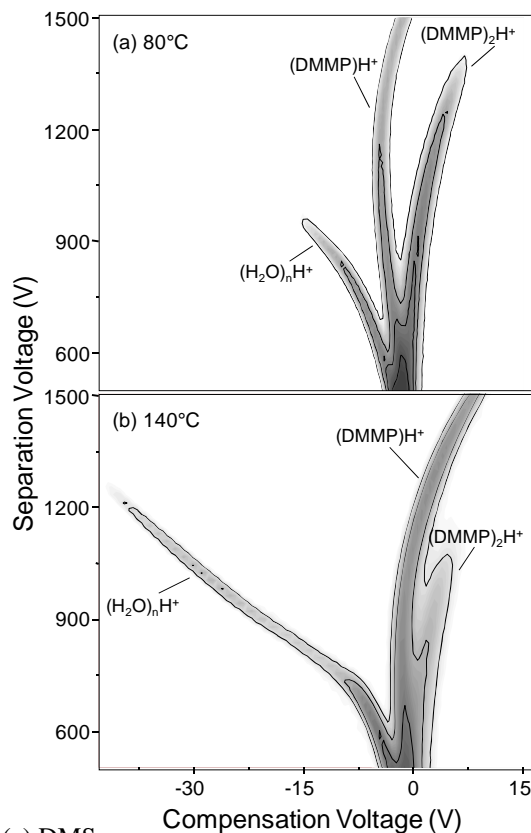


Fig 4. Dispersion plots for DMMP in air at (a) 80°C and (b) 140°C

Current and Future

Our intention to obtain kinetic parameters for dissociation of ions must be expanded to include fragmentation, dissociation, and hydrogen abstraction all simultaneously and the current kinetic IMS alone will not allow us to make such determinations. We can observe with the current instrument kinetics of reactions; however, the Faraday plate detector is not capable enough to assign ion intensity to individual product ions. Fortunately, we have a mass spectrometer which can be fitted to the kinetic IMS and we are making an next instrument build with an MS detector. We have studied a range of explosives from nitrotoluene to TNT and also taggants with nearly the same result: very complex chemistry not able to be deconvoluted without a mass spectrometer detector. We will finish building the instrument and begin IMS/MS studies.

References

1. R.E. Ewing, G.A. Eiceman, C.S. Harden, and J.A. Stone, "The kinetics of the decompositions of the proton bound dimers of 1,4-dimethylpyridine and dimethyl methylphosphonate from atmospheric pressure ion mobility spectra", *Int. J. Mass Spectrom.* 2006, 76-85, 255-256.
2. X. An, J.A. Stone, and G.A. Eiceman, Gas Phase Fragmentation of Protonated Esters in Air at Ambient Pressure through Ion Heating by Electric field in Differential Mobility Spectrometry and by Thermal bath in Ion Mobility Spectrometry, *International Journal of Mass Spectrometry* 2009, published
3. X. An, J.A. Stone, and G.A. Eiceman, A determination of the effective temperatures for the dissociation of the proton bound dimer of dimethyl methylphosphonate in a planar differential mobility spectrometer. *International Journal of Ion Mobility Spectrometry* 2010, published
4. X. An, J.A. Stone, and G.A. Eiceman, Dissociation of proton bound dimers of ketones at ambient pressure in air through thermal and electric field induced energy, *Journal of Physical Chemistry*, in preparation.
5. R.E. Ewing, G.J. Ewing, D.A. Atkinson, and G.A. Eiceman, A critical review of ion mobility spectrometry for the detection of explosives and explosive related compounds *Talanta*, **2001**, 54, 515-529.

Students X. An, PhD in February 2010; Y. Rajapakse, PhD Student in Summer 2010

Damage Criterion and Residual Life of Structural Steel Subjected to Blast Loading

H. Ghonem
Department of Mechanical Engineering
University of Rhode Island

Objectives

The objective of the study is to determine the effects of blast loadings on the residual life of the low carbon structural steel which is the primary reinforcing phase material in almost all critical civil structures in the USA. This objective is achieved by identifying a deformation criterion described in terms of the twin volume fraction in the impacted material. This criterion will be established by coupling three methods; numerical simulations of impact conditions, constitutive material modeling based on the laws of mass, momentum, and energy conservation, and experimental work involving high velocity impacts using a plate driven gas gun. Finite element simulation of impact conditions provides knowledge of impact wave parameters as well as a description of the blast related stress distribution within the impacted steel. The residual life is obtained experimentally by assessing the ductility reduction and available fracture energy as a function of twin volume fraction. From this study, a link between blast history and residual life of the reinforcing steel phase will be established.

Summary

The effect of impact loading on the microstructure deformation and corresponding residual life of low carbon steel have been examined using an integrated experimental, analytical and numerical approach. A series of five plate impact experiments have been carried out on disc type steel specimens using a single stage gas gun with projectile velocities ranging from 200 to 500 m/sec, see Fig. 1a. Fixed back conditions, Fig 1b and 1c, were employed in order to minimize loss of impact energy. Longitudinal stress histories were recorded using stress gauges bonded centrally between the back surface of the target disk and a steel backing plate.

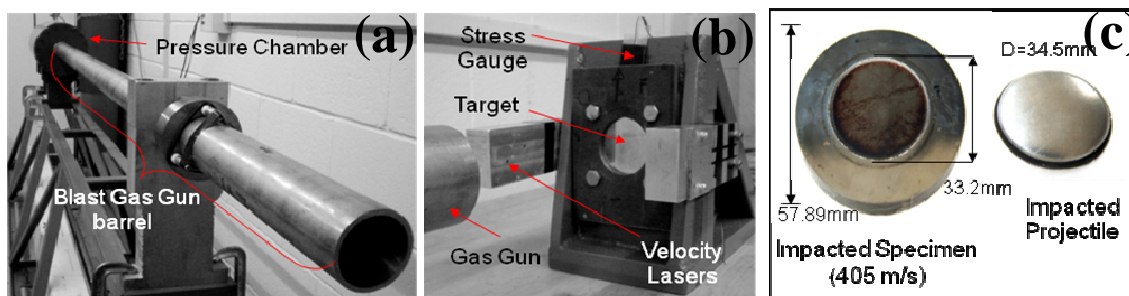


Fig. 1: a) Experimental gas gun; b) Target fixed back; c) Impacted specimen & projectile

Optical microscopy of post impact test specimens revealed a high density of mechanical twins within the α -ferrite grains, Fig. 2a and 2b, as compared to the no impact condition, Figure 2c. The volume fraction of the twins in the impacted specimen was calculated using systematic manual point count method and shows a nonlinear increase of the volume fraction as the impact stress approaches a level of saturation (Fig 2d).

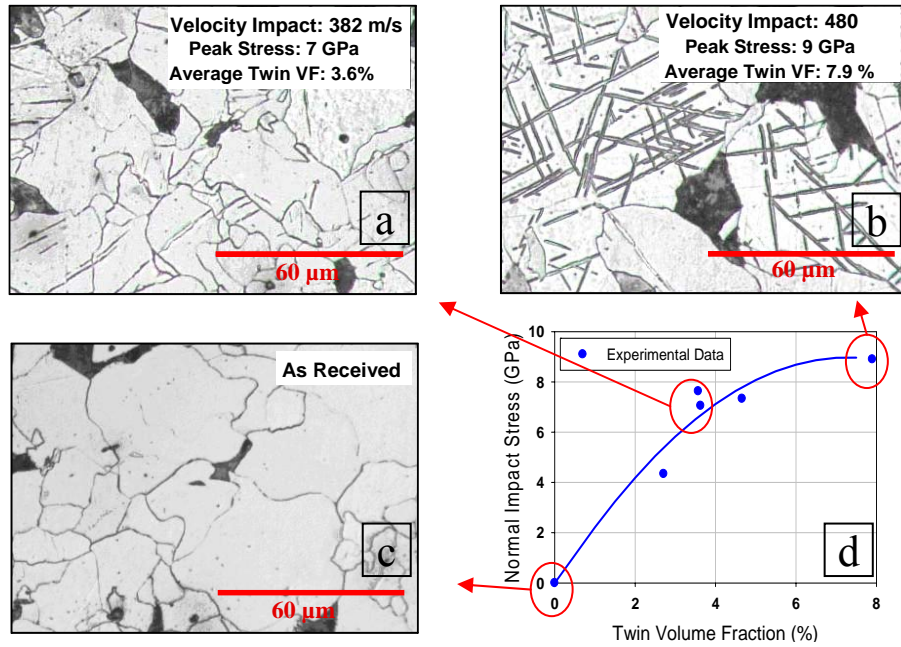


Fig. 2: Experimental twin volume fraction as a function of blast stress and impact speed

A numerical procedure has then been carried out to simulate blast loading of a plate driven impact, replicating the process of a steel member subjected to blast loadings, and similar to those carried out experimentally. This simulation provides knowledge of impact wave velocity as well as corresponding stress field across the test specimen, See Fig 3.

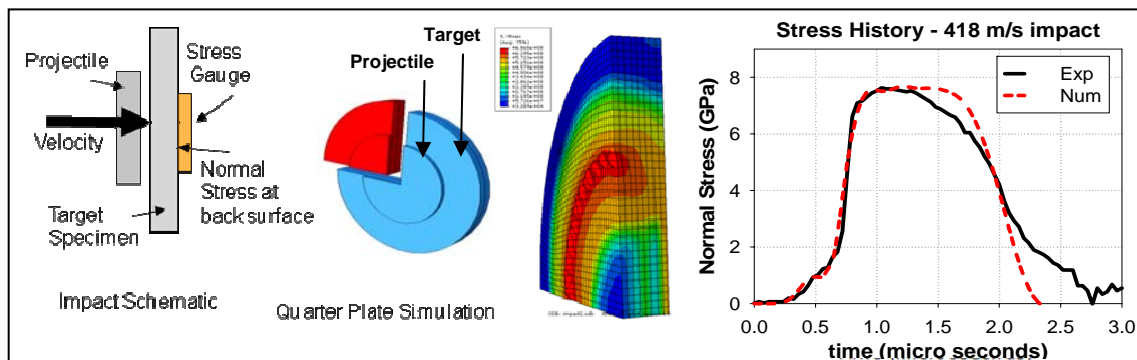


Fig. 3: (a) simulated experimental set up, (b) Numerically obtained stress field across the specimen, and (c) Comparison of experimentally and numerically obtained back stress wave

Results of this model have been used to optimize material parameters required for the implementation of analytical constitutive model to calculate the twin volume fraction as a function of blast wave pressure and associated particle velocity. The coupling of the numerical simulation tool and the analytical constitutive model represent the basis for the experimental tasks of determining the volume fraction of twins.

Achievements

- Blast defined deformation criterion has been established for low carbon steel in terms of twin volume fraction.
- High rate impact loading of steel specimens using a light gas gun has been carried out for a stress range of 4-10 GPa.
- A correlation between blast loading and the amount of twin formation has been established for five different impacts.
- Current work on a coupled analytical-numerical blast material model is being developed and applied to simulate microstructural and mechanical deformation response as a function of blast velocity.
- Residual life assessment are in final stages of preparation
- 2 Journal paper has been prepared; one is submitted to International Journal of Impact Engineering
- A conference paper in IMPLAST 2010 Conference report proceedings has been accepted

Future Work

Residual life Due to Extreme and Repeated Blast Loadings of Critical Civil Structures

Fatigue specimens are to be extracted from blast impacted discs and tested to measure residual life as a function of twin volume fraction, see Fig. 5. A correlation between residual life and twin deformation volume fraction will be established. When completed, the approach will be examined for level of blast loadings for strain rates ranging from 10^5 s^{-1} to 10^8 s^{-1} . Currently, our available gas gun operates in the low to intermediate blast pressure. In order to extend the residual life research, a unique hypervelocity gas gun is being developed by Ghonem's research group at URI. The design, while incorporates similar design aspects of current techniques, is rated for ten times the current pressure and incorporates a quick release system for pressure discharge to projectile, of which the existing method is lacking. The pressure chamber is designed for a maximum pressure of 10,000 psi; Figure 6. Based upon calculated projectile velocities, a target velocity of over 1000 m/s and a peak stress level of 20 GPa is expected. The successful design and construction of this advanced gas gun will provide the experimental means to capture the full range of explosive impacts and allow the study of multiple impact events, which are of high priority in blast mitigations of critical civil structures.

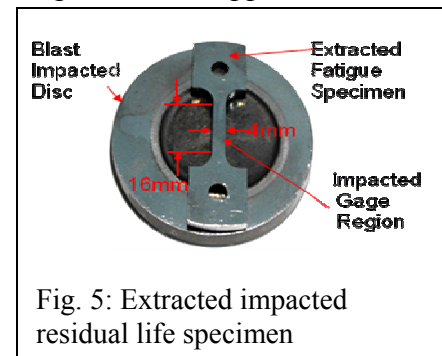
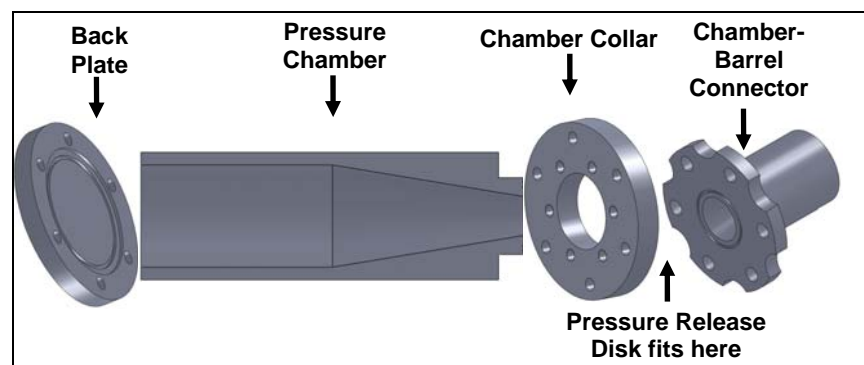


Fig. 6: Main components of ultra high speed proposed gas gun



Attenuation and mitigation of stress waves propagating in blast shielding materials

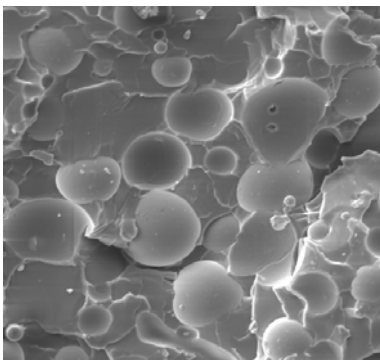
Carl Ernst Rousseau
University of Rhode Island

Objectives

One of the most important aspects of mitigation consists in the ability to develop effective structures and materials that can withstand the extreme loading conditions found in blast and impact situations. To succeed in fulfilling those tasks, these materials must also be subject to structural constraints related to weight and volume, thereby the necessity of selecting novel, light-weight composites, or heterogeneous materials in the search for ideal shielding and structural integrity. Particulate-, and fiber-based composites have been an essential element of novel material development, and thus require behavioral scrutiny at high loading rates. The response of these multi-phase materials under dynamic conditions is complex due to the considerable wave interactions and local failure modes that exist within the non-homogeneous material. The latter may include local debonding, cracking, or comminution as a function of the particle size, shape, and layout. Attempting to optimize dynamic properties for protection purposes calls for a thorough understanding of the micromechanical behaviors, as well as particulate to matrix interactions that will provide desirable responses. Thus, the purpose of the research is to investigate and quantify such behaviors in model materials, by carefully tracking propagating waves within them. Particulate composite materials will have claim to the primary focus in the first stages of the research, with a special emphasis on the geometries of single and multiple inclusions. The research will also investigate the specific behavior of particulates and microstructural components in the material system, and relations will be established between local failure and macroscopic response.

Details

Technical Approach: Various means of dissipation of the energy imparted by a bullet, projectile, shrapnel strike, or by an explosion are being sought. In all these various cases, the stress wave generated propagates within the material, conveying damage along its path. Our goal is to minimize such damage, thereby, the focus on attempting to control both the magnitude and the breadth of the propagating stress. In addition to particulates and other types of composites, as well as biomimetic inspired material systems, certain methodologies such as purposeful induction of areas of local collapse, may constitute natural energy sinks, or diverting means by which we may achieve our mitigation goals.



SEM of sectioned model material showing particulates within matrix.

Task 1 - Direct Stress Attenuation: The effectiveness of each material system is determined primarily through a stress wave propagation method, where stress attenuation over a specific distance within the material is recorded by means of embedded piezoresistive stress gages. We are also currently engaged in implementing the recently developed Photonic Doppler Velocimetry, a system through which deflection in the path of the light reflected from the back face of a specimen is captured. These variations are effectually indicative of the velocity profile (particle velocity) at the rear of the specimen and provides a means of verification of the stress recording by means of direct stress-speed relations. In addition, the technique is attractive as it is a non-invasive, non-contact method, and circumvents any slight deviation that might result from the presence of the gage in the material.

Task 2 - Internal Friction: Inherent internal friction within the material is being sought as this effect is representative of the mechanism present in energy dissipation, thereby in the dampening of the damage caused by nefarious external effects. The initial effort in this area is focussed on hollow glass particulates, or microballoons, immersed within an epoxy matrix, forming what is generally called a syntactic foam. Such material have numerous application in situations requiring a combination of reduced density, high compressive strength, low moisture absorption, and improved damping properties. Thus, they have become a frequent component in sandwich composites used in aerospace and maritime applications. Ultrasonic waves are launched into the material. Retrieval of this wave upon exiting the material provides a measure of the internal friction elicited in reducing its magnitude. Ultrasonic attenuation coefficient from experiment is compared with a previously developed theoretical model for low volume fractions, and takes into account attenuation loss due to scattering and absorption. In addition to evaluating the apparent attenuation, quasi-static compressive tests were also conducted to fully characterize the material. Both quasi-static and dynamic properties, as well as coefficients of attenuation, ultrasonic velocities are strongly dependent upon the volume fraction and size of the microballoons. Criteria are established to provide guidance for the usage of these materials under a wide range of conditions. These same materials will now be investigated with the particulates positioned in a functionally-graded configuration.

Task 3 - Stress Wave Scattering: At least as important in heterogeneous material, is the scattering or dispersion across grain boundaries, and at particle or material interfaces. This mechanism generates complex stress wave interactions that can greatly diminish stress propagation-induced failure. Thus, our goals here is to enhance the scattering mechanisms through manipulation of the microstructure.

Task 4 - Numerical Modeling: Companion finite element simulations aimed at guiding the direction of the experiments are performed routinely. Conversely, each experiment is simulated numerically in an attempt to establish better simulations techniques, and sound predictive methods. Upon correlation of specific empirical and numerical data, the latter can then be used to surmise the full-field, detailed information about the material behavior.

Accomplishments

Publications

A peer-reviewed article on the behavior of functionally graded materials, under quasi-static and low impact conditions is set for publication this year. The specific focus of this article is on

the preferential path followed by cracks during failure events. Three presentations will be made in October at the SEM-IMPLAST 2010 conference. All three will be expanded and submitted to peer-reviewed journals.

Students

One student will have received his Master's degree at the end of the year as a result of his work on this activity. Another, doctoral student is fully supported by this effort. The two students supported are, respectively, Bhaskar Ale and Gifford Plume.

Collaborations

The techniques used in the research are very versatile in that their application is universal to any material. Thus, they have led to two collaborative ventures. The first relates to the study of structural steel. Properties of the material are evaluated at high temperatures in their virgin state. This is, again, repeated after impact, thus simulating a material state that is subsequent to an explosion or collision. The embedding of the gages within the material provide a faithful profile of the internal loading, which can therefore be inserted as numerical input to numerical simulations. Inference of the health monitoring of buildings is the ultimate goal of this exercise.



Example of damage imparted to structural steel. Embedded gage is seen appended to specimen.

The second collaborative project involves the spallation study of cast iron, with the national laboratories. Spallation is a common occurrence in metals that follows a strike or an explosion.

Development of Novel Composite Materials & Structures for Blast Mitigation

Arun Shukla
University of Rhode Island

Objective

The present study aims at developing novel materials and structural configurations that could be effectively used for blast mitigation. The study also focuses on understanding the structural response to separate and simultaneous blast and fragment impact. The ability of a structure to absorb and reflect blast energy is extremely important in blast mitigation. Thus, an effort was also made to better understand the redistribution of blast energy during the blast loading process.

Summary

A shock tube apparatus was utilized to generate a controlled shock loading on the specimens (Fig. 1a). It has an overall length of 8 m, consisting of a driver, driven and muzzle section. The high-pressure driver section and the low pressure driven section are separated by a diaphragm. By pressurizing the high-pressure section, a pressure difference across the diaphragm is created. When this difference reaches a critical value, the diaphragms rupture. This rapid release of gas creates a shock wave, which travels down the tube to impart dynamic loading on the specimen. The driver gas is helium and the driven gas is ambient air.

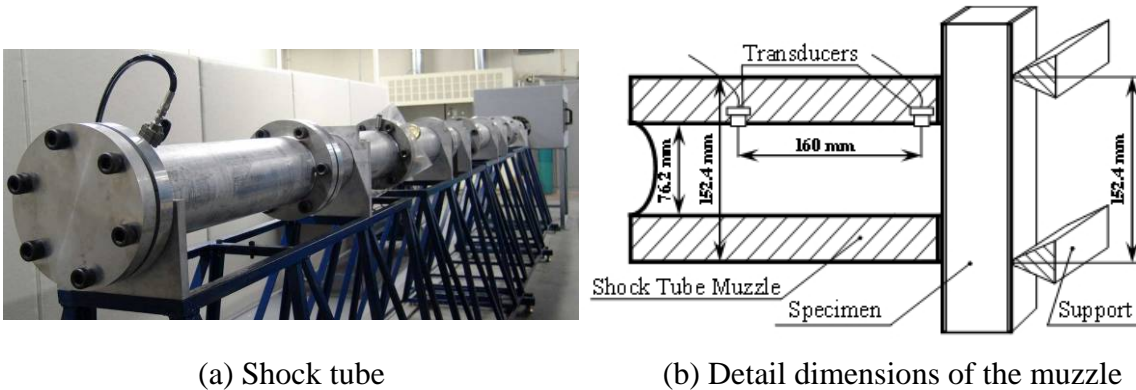


Fig 1: Shock tube apparatus

Fig. 1b shows detailed dimensions and locations of the muzzle, specimen, supports and the pressure sensors (PCB102A). The sensors are mounted at the end of the muzzle section to measure the incident pressure and the reflected pressure during the experiment. The final muzzle diameter is 0.0762 m (3 in). The distance between the two sensors is 0.16m and the distance between the second sensor and the end of the muzzle is ~0.02m. The specimen was placed in the supports and positioned close to the end of the muzzle. These support fixtures ensure simply supported boundary conditions with a 0.1524 m (6 in) span. Fixtures have also been developed for ensuring a fully clamped boundary conditions and simply supported boundary conditions with a span of 0.2032 m (8 in) and 0.254 m (10 in). Fig. 2 gives a typical pressure profile.

Digital Image Correlation (DIC) technique was also used to measure the full-field, in-plane and out-of-plane displacements. The DIC arrangement is shown in fig. 3. Initially the camera records an image of the specimen in its un-deformed state. A second picture is then taken

after the specimen has deformed. The two images are then compared in order to calculate the in-plane and out-of-plane displacements of the specimen. A random speckle pattern is applied on the specimen and each speckle individually tracked in order to obtain the in-plane and out-of-plane displacements.

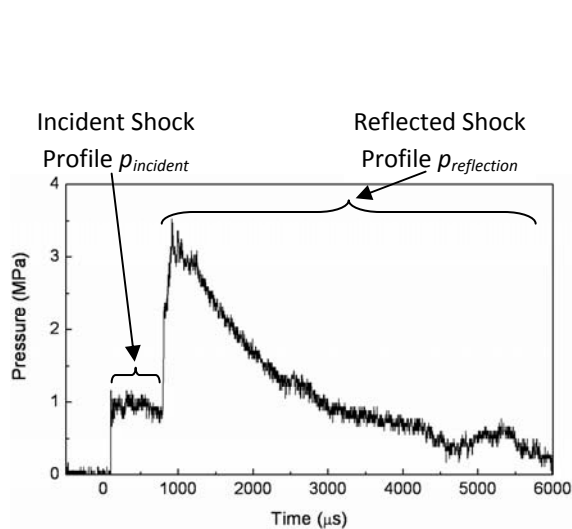


Fig 2: Typical experimental pressure profile

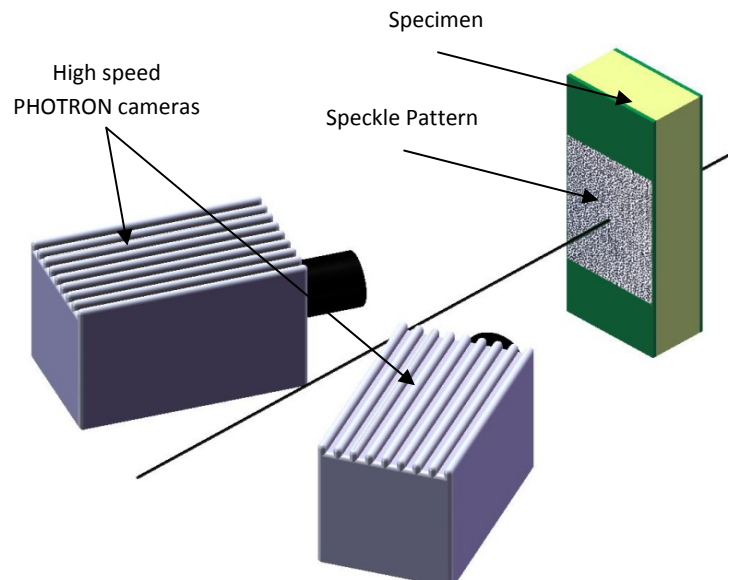


Fig 3: Schematics of the back face DIC analysis

Accomplishments

Task 1. Dynamic Constitutive Behavior of Foam Core Materials

This task involved the investigation of dynamic constitutive behaviors of the foam cores (Corecell™ A-Series) utilized in our sandwich composites using a Split Hopkinson Pressure Bar (SHPB). These foam materials are used to manufacture light weight composite structures which have a good blast mitigation property. This particular study helped to better understand the behavior of functionally graded material.

Task 2. Response of Pre-Damaged (shrapnel) Composites to shock loadings

In case of an explosion, it's not just the blast waves which cause the damage to structures. Shrapnel and other fragments also hit and cause damage to the specimen and then they are subjected to the blast/explosion loading. Thus, sandwich composites with existing damage were studied under blast loading conditions in order to determine how such pre-damage affects the response of the specimens to blast loads. Two different types of pre-damage were investigated, which consisted of ballistic damage and low-velocity impact damage respectively.

Task 3. Evaluation of Energy Associated with Shock Wave

The ability of a structure to absorb and reflect blast energy is extremely important in blast mitigation. Structures that can absorb and reflect blast energy effectively will efficiently dissipate and disperse the intensive pressure pulse and protect anything located behind them. Evaluating various energies, such as the energy stored in the shock wave as well as the energy reflected from and transferred into the structures, will help in understanding the energy redistribution behavior during the blast loading process. Analytical expressions were developed

using gas dynamics equations to evaluate the energy associated with the incident shock wave (incident energy) and the reflected shock wave (reflected energy) for a shock tube experiment.

Details

Task 1. Dynamic Constitutive Behavior of Foam Core Materials

The main aim of this study was to investigate the dynamic constitutive behaviors of the foam cores (Corecell™ A-Series) utilized in our sandwich composites using a Split Hopkinson Pressure Bar (SHPB). Three types of Corecell™ A foam were studied, A300, A500 and A800. The densities are $\sim 58 \text{ kg/m}^3$, $\sim 92 \text{ kg/m}^3$ and $\sim 150 \text{ kg/m}^3$ respectively. Fig.4 shows the quasi-static and high strain-rate behavior of the different types of Corecell™ A foams. For quasi-static behavior, the stress-strain curves show three deformation regions: the elastic region; the plateau stress region and the densification region. For high strain rate behavior, the stress-strain curves also show elastic and plateau stress regions though the strain does not reach the densification region. Table 1 shows the quasi-static and high strain-rate yield stresses. This shows the high energy absorption ability of these foams under low stress levels.

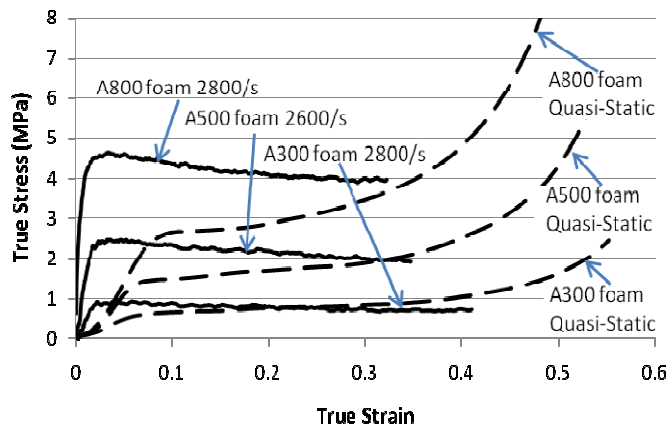


Table 1. Yield strength of Corecell™ A foams

Foam Type	A300	A500	A800
Quasi-Static Yield Stresses (MPa)	0.60	1.35	2.46
High Strain-Rate Yield Stresses (MPa)	0.91	2.47	4.62

Fig 4: Quasi-static & high strain-rate behaviors of different types of Corecell™ A Foams

Task 2. Response of Pre-Damaged (shrapnel) Composites to shock loadings

This particular task focused on the response of sandwich composites with existing damage to blast loading in order to determine how such pre-damage affects the response of the specimens to blast loads. Two different types of pre-damage were investigated, which consisted of ballistic damage and low-velocity impact damage respectively. The sandwich specimens were comprised of two E-glass fiber vinyl-ester composite facesheets with a quasi-isotropic layup $[0/45/90/-45]_S$ and a Corecell™ A800 foam core. The specimen dimensions were 254 mm long, 102 mm wide, and 60 mm thick with a face sheet thickness of 5 mm. The average areal density of the specimens was 27.9 kg/m^2 . An example of a specimen is shown in Fig.5.

2.1 Ballistic Damage

Ballistic damage was imparted to the specimens in a controlled fashion in order to regulate the level of damage in each specimen. The level of damage was controlled by the number of times that an individual specimen was struck by a projectile. The projectiles used were 165 grain (10.69 gr.) APM2 armor piercing bullets fired from a 300 Winchester magnum. An image and dimensions of the projectile type are shown in Fig.6.

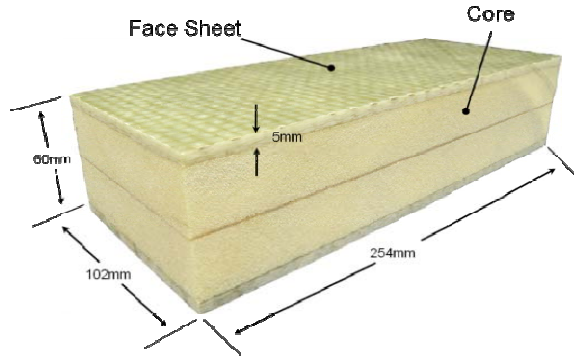


Fig 5: An example of specimen


		.30 cal. 165 grain Spitzer Copper Jacket Stainless Steel Core	
Diameter	Length	Mass	Average Velocity
7.89 mm	34.9mm	10.69 g	320 m/s

Fig 6: An image and dimensions of the projectile

2.2 Low Velocity Impact Damage

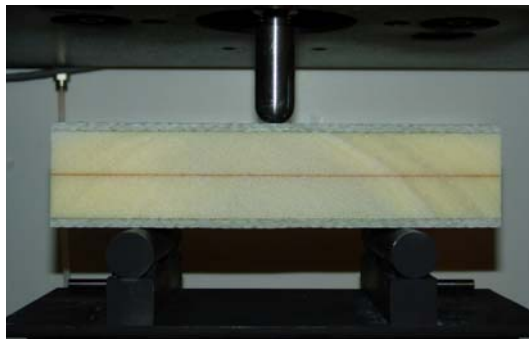


Fig 7: Low velocity impact setup

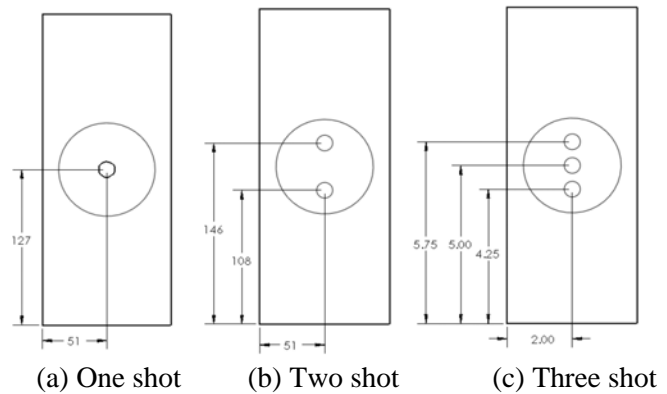


Fig 8: Impact locations on specimens

Low velocity impact damage was imparted to the specimens using an Instron Dynatup 9210 drop tower in order to regulate the level of damage in each specimen. As shown in Fig 7, the specimens were placed in simply supported conditions. A 25.4 mm diameter hemispherical striker was installed on the top and the impact energy was chosen as 300 J. The level of damage was controlled by the number of times that an individual specimen was struck by an indenter. The number was varied from 1 to 3. The locations of the impacts for each specimen are shown in Fig. 8. Impacts were located within a 76.2 mm diameter circle that was centered on the specimen and this area corresponds to the loading area of the shock tube.

2.3 Shock wave loading results

The same experimental setup as in Fig. 1 was utilized for a controlled shock loading. An incident shock wave with incident peak pressure of approximately 1.7 MPa and a wave velocity of approximately 1300 m/s was generated and impinged upon the specimen. The simply supported span is 203.2 mm. Fig. 9 and 10 show the post mortem images of the specimens with ballistic damage and low-velocity impact damage, respectively.

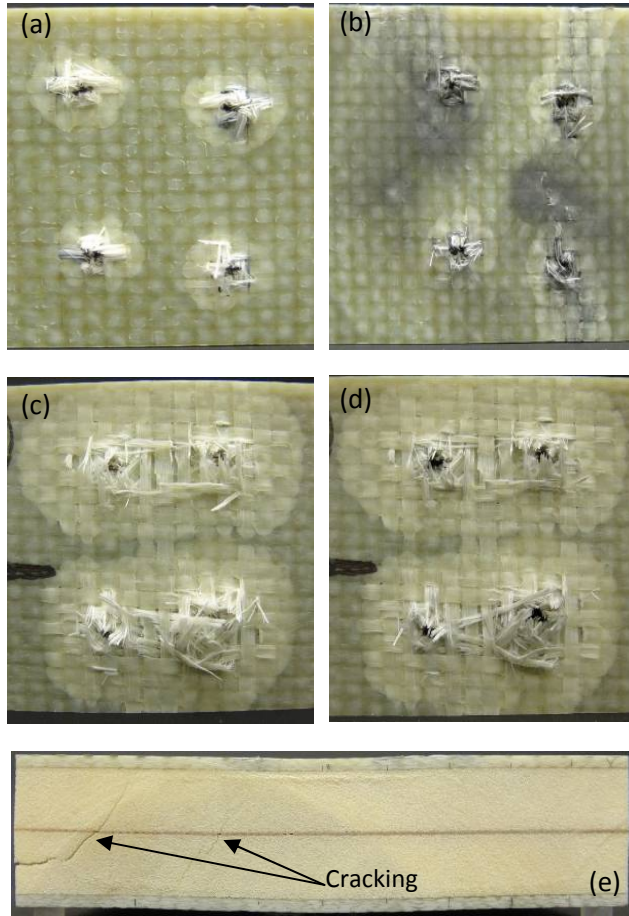


Fig 9: Ballistic damage
 (a) Pre-blast ballistic damage on front face
 (b) Post-blast damage on front face
 (c) Pre-blast ballistic damage on exit face
 (d) Post-blast damage on exit face
 (e) Core cracking after blast loading

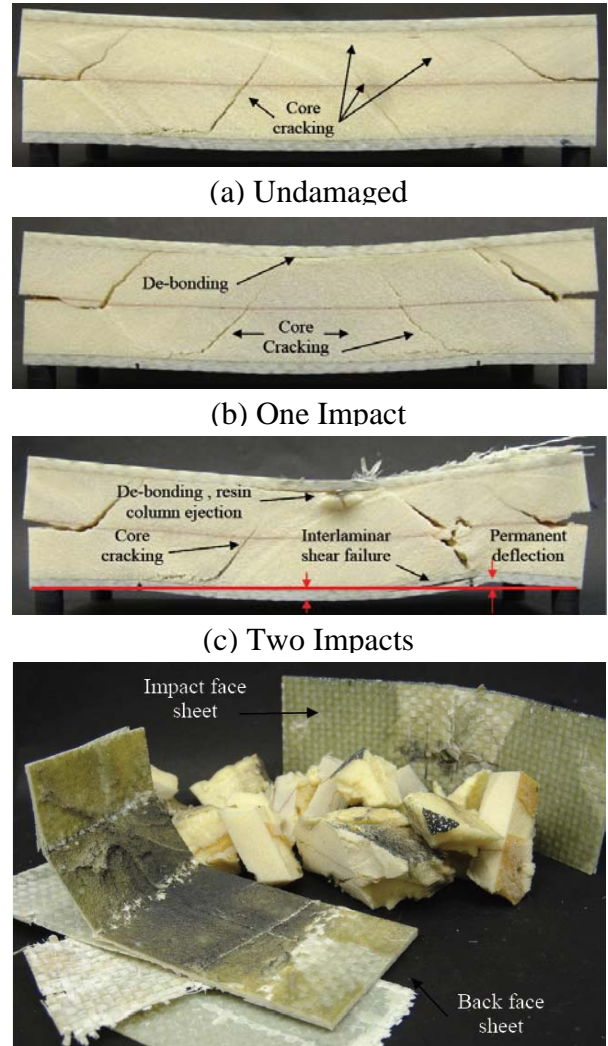


Fig 10: Post mortem images of low velocity impact damage followed by blast experiments

Task 3. Evaluation of Energy Associated with Shock Wave

The energy stored in the shock wave is equivalent to the work done by the gas as it propagates through the cross-section of the shock tube. When a shock wave with pressure profile $p(t)$, which induces a gas particle speed u , propagates through a tube with cross sectional area S and impinges a panel, the work that the shock wave imparts on the panel during time dt is $p(t)*S*u*dt$. Thus, the total energy stored in the gas during the loading process can be obtained by integrating $p(t)*S*u*dt$ with respect to time, as shown in Eq. (1) and (2).

$$E_{incident} = \int [p_{incident}(t) * S * u_{incident}] dt \quad (1)$$

$$E_{reflected} = \int [P_{reflected}(t) * S * u_{reflected}] dt \quad (2)$$

Here, the cross sectional area S , of the shock tube is a known constant and the pressure profiles of the shock wave $p(t)$ can be measured. The particle speed u located behind the shock

wave front can be calculated using gas dynamic theory based on the pressure profiles. This algorithm can be implemented to evaluate the energy stored in the impinging gas (input energy) and the energy remaining in the impinging gas that is disturbed by the reflected shock wave (remaining energy).

If the shock pressure applied on the panel is assumed uniform within the shock tube muzzle area, the force applied on the panel can be obtained by multiplying the pressure by the area. From high speed side view images, the deflection-time data of the panel can be measured. Then, the force-deflection data can be obtained by combining the force-time data and deflection-time data. The energy required to deform the panel can be calculated as the area under force-deflection curve. Thus, this algorithm can be implemented to evaluate the deformation energy as eq. (3).

$$E_{deformation} = \int_{S_{shock\ tube}} \left(\int p(t) dl_{deflection} \right) dS \quad (3)$$

Fig. 11 shows an example of the evaluated energies, which came from the experiment conducted on sandwich panels with a four layer core gradation. The difference between input and remaining energies is the energy lost during the shock wave-specimen interaction. This energy includes the energy absorbed by the composite structures, sound, light, heat and other forms of energy. It can be seen that a large amount of energy was still remain in the gas after the shock wave loading on the specimen (remaining energy). The deformation energy is the energy that the gas applied on the specimen after the shock wave-specimen interaction. The total energy mitigated by the sandwich structures is the summation of the deformation energy and the difference between input and remaining energies.

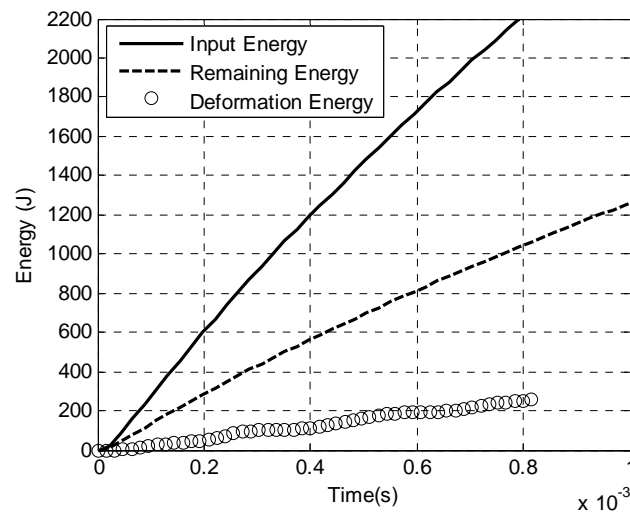


Figure 11: Comparison of evaluated energies

Students Supported

1. Puneet Kumar
2. Matthew Jackson
3. Daniel Gracia
4. Jefferson Wright
5. Andrew Krystnewicz

Conference & Journal Publications

1. E. Wang, N Gardner, A. Shukla, "The blast resistance of sandwich composites with stepwise graded cores", *International Journal of Solid & Structures*, 46, 3492-3502, 2009.
2. E. Wang, A. Shukla, "Analytical and Experimental Evaluation of Energies during Shock Wave Loading", *International Journal of Impact Engineering*, submit for publication.
3. E. Wang, N. Gardner and A. Shukla, "Experimental study on the performance of sandwich composites with stepwise graded cores subjected to a shock wave loading", SEM Annual Conference and Exposition on Experimental and Applied Mechanics, Albuquerque, New Mexico , June 1-4, 2009.
4. N. Gardner, "Blast performance of sandwich composites with discretely layered core", SEM Annual Conference and Exposition on Experimental and Applied Mechanics, Student Paper Competition, Albuquerque, New Mexico , June 1-4, 2009.
5. S.A. Tekalur, E. Wang, M. Jackson and A. Shukla, "Failure Behavior and energy absorption of sandwich composites under dynamic loading", SEM Annual Conference and Exposition on Experimental and Applied Mechanics, Albuquerque, New Mexico , June 1-4, 2009.
6. E. Wang and A. Shukla, "Evaluation of Incident, Reflected and Deformation Energies During Blast Experiments", SEM Annual Conference and Exposition on Experimental and Applied Mechanics, Albuquerque, New Mexico , June 1-4, 2009.
7. N. Gardner and A. Shukla, "The Blast Response of Sandwich Composites With a Functionally Graded Core", SEM Annual Conference and Exposition, Indianapolis, Indiana, June 7-10, 2010.
8. N. Gardner and A. Shukla, "The Blast Response of Sandwich Composites With a Functionally Graded Core and Polyurea Interlayer", SEM Annual Conference and Exposition, Indianapolis, Indiana, June 7-10, 2010.
9. E. Wang and A. Shukla, "The Blast Response of Sandwich Composites with In-Plane Pre-Loading". SEM Annual Conference & Exposition, Indianapolis, IN, June 7-10, 2010.
10. P. Kumar and A. Shukla, "Blast Loading response of Glass Panels", SEM Annual Conference and Exposition, Indianapolis, Indiana, June 7-10, 2010.
11. E. Wang and A. Shukla, "Core Deformation of Sandwich Composites under Blast Loading", SEM Annual Conference and Exposition, Indianapolis, Indiana, June 7-10, 2010.
12. E. Wang and A. Shukla, "Blast Response of Sandwich Composites using Digital Image Correlation Technique", 9th International Conference on Sandwich Structures (ICSS9), Caltech, Pasadena, California, June 14 - 16, 2010.
13. E. Wang and A. Shukla, "Performance of Pre-Stressed Sandwich Composites Subjected to Shock Wave Loading", 14th International Conference on Experimental Mechanics (ICEM 14), Poitiers, FRANCE July 4-9, 2010.

Structural Response to Non-ideal Explosions

J. E. Shepherd , J. A. Karnesky ; J. S. Damazo

California Institute of Technology

Objective

The objective to develop the capability to predict the effect of non-ideal explosions, i.e. the degree of plastic deformation induced by a non-ideal explosion and to investigate methods to mitigate the extent of the deformation.

Summary

Experiments and numerical simulations were performed in the Explosion Dynamics Laboratory in thin-walled steel tubes. Gaseous detonations were used as a model to simulate various internal explosions. The first series of experiments was performed in C1010 mild steel tubes with a 1.5 mm wall thickness and 1.2 m length. The detonable mixture used was stoichiometric $C_2H_4-O_2$ at pressures varying from 0.8 bar to 3 bar. Three regimes of deformation were observed for different initial pressures. For low pressures (less than 1 bar), the deformation was purely elastic. Mid-range pressures (2 bar in these tests) saw plastic deformation on the reflected wave only. At high pressures (3 bar), plastic deformation (residual strains up to 20%) was observed on both the incident and reflected waves. We were able to perform numerical modeling to obtain quantitatively close results in each of these deformation regimes.

Accomplishments

Carried out first plastic deformation testing with repeated loading using gaseous detonation.

Measured reflected pressure history and developed pressure-time loading model.

Used finite element numerical simulations and SDOF models to compare predicted and measured deformation. Tested several material response models.

Discovered periodic deformation mode and explained origin with wave interference concepts and plastic deformation models.

Details

It is the goal of these experiments to obtain a guideline such that, given an initial pressure, one may predict whether plastic deformation occurs and, if plastic deformation does occur, to what extent. In order to do this, a facility was constructed to allow us to plastically deform 127 mm diameter, 1.5 mm wall thickness tubes with an internal detonation (Fig. 1). In order to avoid initiation transients within the specimen tubes, the detonations were initiated in a 1.2 m long thick-wall tube and allowed to develop into a steady near-CJ wave before entering the specimen tube. The presence of a well-formed detonation wave was confirmed with pressure gauges located in the driver tube. To ensure proper wave reflection, the test specimen tubes were held between an aluminum plug and steel collet at the reflection end. A pressure gauge was also located inside the aluminum plug to record the pressure trace in the reflecting end.

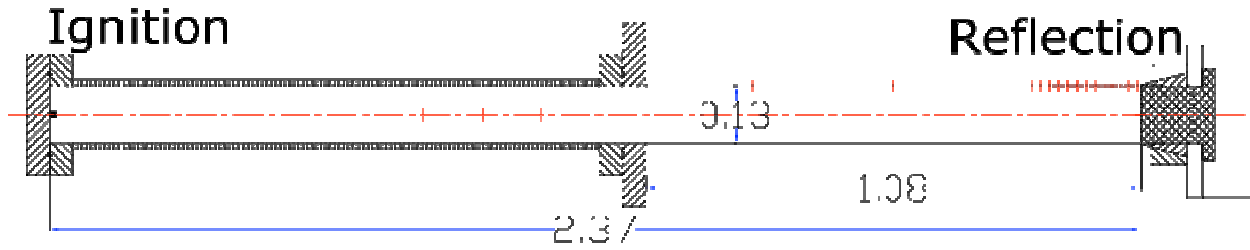


Figure 1: Diagram of experiment used in detonation experiments, dimensions in meters.

Tube deformation and movement measurements were obtained with strain gauges, a displacement gauge, and a high-speed camera; hence we were able to record the dynamic material response to the explosion. Figure 2 shows two specimen tubes after repeated detonations. Figure 2a was subjected to five detonations of a mid-range pressure (2 bar) and Fig. 2b was subjected to three detonations of a high pressure (3 bar). The sharp rise on the right-hand side of the tubes indicates where the collet and plug terminated.

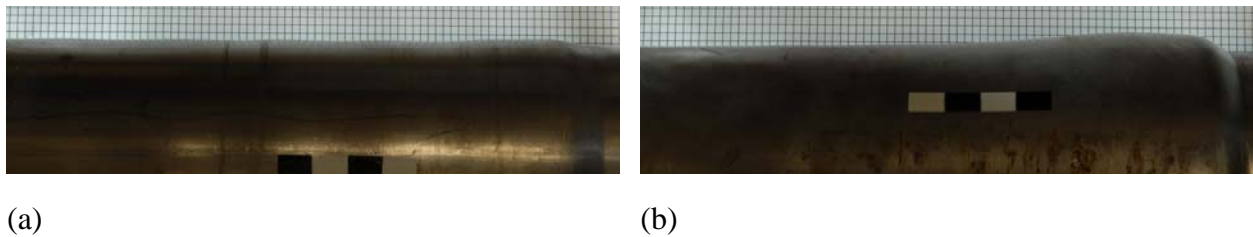


Figure 2: Deformed detonation tubes subjected to (a) five 2 bar initial pressure detonations and (b) three 3 bar initial pressure detonations.

Low pressure experiments yielding only elastic deformation were performed with an array of pressure transducers mounted in the tube in order to quantify the pressure loading on the tube—the pressure transducer mount is shown in Fig. 3. We have developed a model for the detonation loading based on ideal gas dynamics and measured end wall pressures. The internal pressure model gives pressures as function of time and spatial location in the region of interest near the reflecting end of the tube. In addition to a model for the pressure, a constitutive relation is required to model the deformation of the tube. To determine the constitutive relation, we collaborated with Prof. Rusinek of Paul Verlaine University in Metz. Using a sample of the specimen tubes, Prof. Rusinek performed a double-shear test to measure the stress-strain curve at strain rates up to 100 s^{-1} .

The modeled pressures and constitutive relation were used to predict residual plastic deformation using two approaches: a single degree of freedom model that includes strain-hardening effects; two-dimensional finite-element simulations using the code LS-DYNA.

Figure 4a portrays the same tube as seen in Fig. 2a. This orientation clearly shows the presence of a periodic deformation mode. This ripple pattern was only observed on the mid-range 2 bar initial pressure detonations. The single degree of freedom simulation explained this result as an interference between the phase of elastic oscillation induced by the incident detonation with the time of arrival of the reflected shock wave. Increasing the pressure decreases the degree of elastic oscillation of the tube wall and hence this deformation mode is not observed for high-pressure detonations.

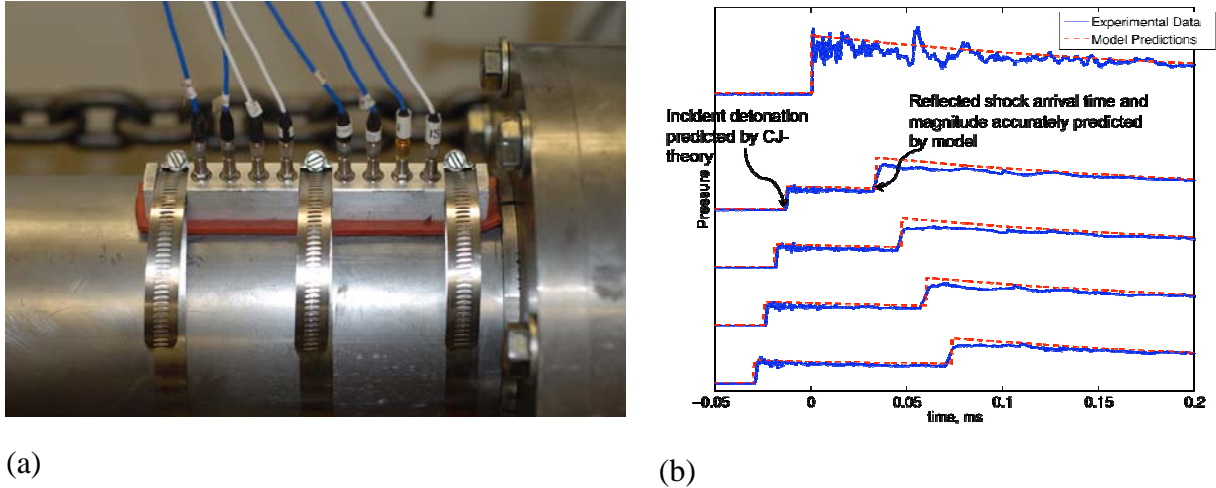


Figure 3: (a) Experimental setup used to validate pressure loading model. (b) Comparison with measured and modeled pressure traces.

Although the single degree of freedom code is useful in examining the physics involved in plastic deformation and in obtaining a quick estimate of the deformation, a more detailed simulation is required to achieve quantitatively accurate comparisons. Thus we performed two-dimensional finite element simulations using the code LS-DYNA. As displayed in Fig. 4b, these finite element simulations were able to give quantitatively accurate results of material deformation. These results also illustrated the importance of employing a very realistic model for the material (stress-strain) properties including strain hardening, strain-rate and thermal softening effects. In addition, we found that careful attention to the mechanics of the supporting structure and attachment of the tube was needed in order to have well-defined boundary conditions with axi-symmetric deformations.

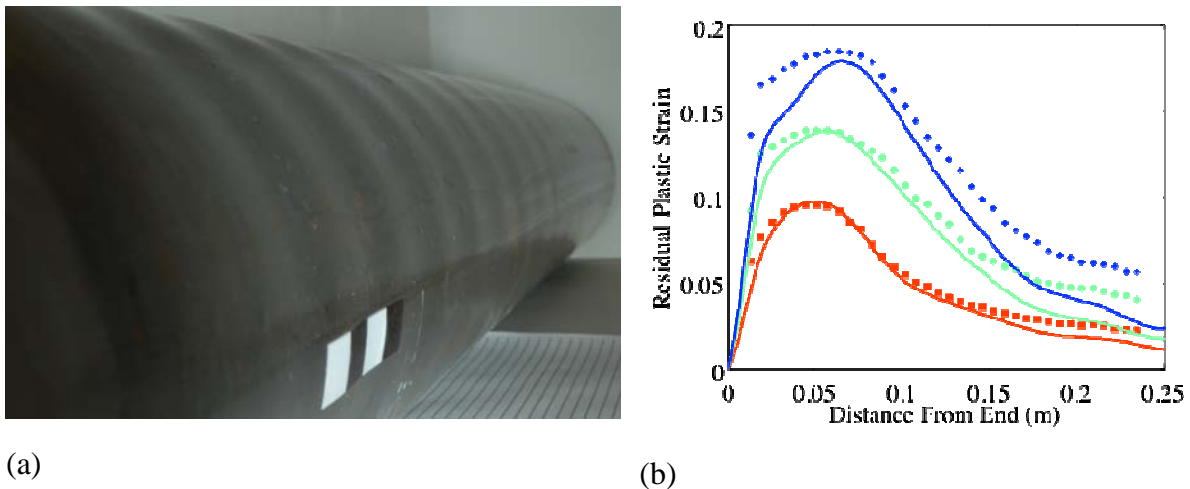


Figure 4: (a) Deformed tube that was subjected to five 2 bar initial pressure detonations. (b) Comparison of finite element simulation with measured residual plastic strain of the specimen tube after each of three 3 bar initial pressure detonations.

Future Work

The goal is ultimately to develop a comprehensive model of plastic deformation, rupture, and blast wave generation for both detonation and deflagration loading. The next steps are:

Carry out testing with better characterized materials including austenitic stainless steel. We need to use materials for which extensive high-strain rate and high-strain properties are well known. There is a large database on 304 Stainless and this is also used in other explosive containment tests. Tests will be performed with several different types of materials that examine a range of material behavior with an emphasis on plastic deformation and rupture properties.

Explore techniques to mitigate the severity of plastic deformation. Proposed methods include either an internal or external polymer coating. In addition to absorbing or transferring energy away from the tube, these coatings are likely to damp the elastic oscillation present in the 2 bar initial pressure case and thereby to lessen the peak height of the observed ripple pattern.

Pursue coupled fluid-structure computations to account for the feedback between deformation and gas dynamics. The deformation in the current experiments is sufficiently large that we expect the gas dynamics to be affected and our simple model of loading will rapidly become inaccurate as more plastic deformation occurs. We plan to use the fluid-structure capability of AMROC with thin-shell models of the structure as a first approach to this problem. Prof. Meiron (Faculty at Caltech) will be helping with this portion of the effort and we will leverage previous (ASC program) and ongoing (PSAAP program) DOE code development efforts at Caltech for the software base.

Develop collaboration with other organizations so we can use their test capabilities for rupturing tubes. The energies and blast waves associated with rupturing large tubes are a challenge for our containment facilities. Scott Jackson of DE-9, Shock & Detonation Physics group at Los Alamos has suggested that it may be possible to use Los Alamos test facilities for this purpose if there is enough overlap with other DHS-sponsored programs at their test site. We are pursuing this possibility.

Water Blast Mitigation: Progress Report

Steve Son, D. Reese, E. Miklaszewski

Purdue University

Objective

The purpose of this study is to investigate the effectiveness of water as a blast mitigant. Water blast mitigation is being investigated in multiple configurations including: solid water barriers, water sprays and water sheets. Solid water barrier tests have been completed and results are presented here. A robust system to evaluate the blast mitigation capabilities of water has been built and initial results are shown here. The effectiveness of water sheets as a mitigation technique is yet to be evaluated. We hope to elucidate the fundamental mechanisms for blast mitigation in these systems by using such techniques as high speed pressure profile characterization, Phase Doppler Anemometry (PDA), high speed imaging and shadowgraphy.

Summary

All tests in this study use an explosively driven shock tube as means of producing a shock wave. By utilizing this setup we achieve a repeatable laboratory scale 1-D shock wave. Figure 1 shows a typical laboratory-produced shockwave, imaged using shadowgraphy. Additionally, by changing the length of the shock tube, the characteristics of the shock wave can be changed. This will allow testing the various water mitigation techniques against characteristically different shock waves. Specifically, different sized shock tubes can produce thin pressure profiles with high peak pressure as opposed to lower peak pressures with longer positive pulse duration.

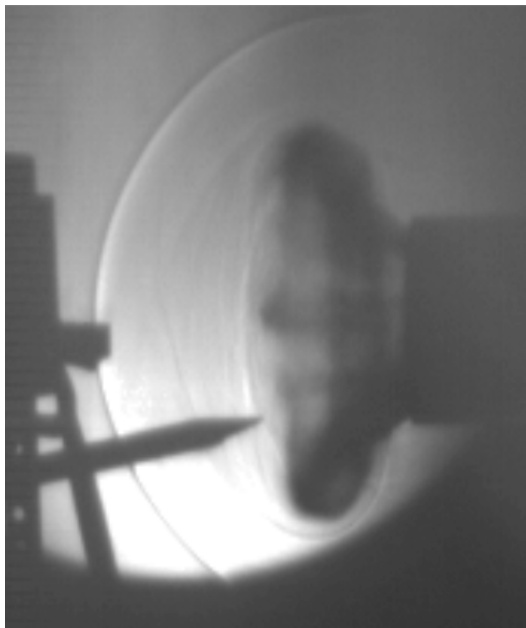


Fig 1: Shadowgraph of a laboratory shock wave

Tests with water-filled barriers, and wet/dry sponges have been completed. Baseline tests without water were also obtained for comparison. High-speed diagnostics were used to characterize the effectiveness of the water barriers. The water is essentially incompressible, so the blast wave is transmitted with minimal losses. In contrast, a water-filled sponge is much more effective at blast mitigation. It is well known that a multiphase system can have an equilibrium sound speed that is much lower than either of its constituents. Consequently, such a system can have a sound speed much lower than that of air or water. This produces a large impedance mismatch, which improves the blast mitigation performance.

Initial tests using water sprays have been completed. Results show a measurable difference between the mitigation ability of a “fine mist” and a “heavy spray”. The fine mist appears to be more effective at decreasing the peak pressure close range (1ft) while heavy spray

appears to be more effective at distance (4ft). This may be due to different energy transfer mechanisms. Additionally, initial results show larger droplets decrease the wave speed of the shock, possibly due to an increase momentum transfer. An extensive testing matrix has been produced to determine the relationship spray number density and droplet size has on the mitigation capability of a spray.

Future work includes:

- Perform remaining spray mitigation tests
- Use Phase Doppler Anemometry (PDA) to accurately classify sprays
- Investigate “water sheets” as a blast mitigant
- Investigate shock wave interactions with single droplets

Accomplishments

In the solid barrier tests, the effectiveness of wet and dry sponges as a mitigant has been quantified. In comparison to free field gauge, the dry sponge slightly decreased the peak overpressure by 4.5% while increasing the impulse by 90% and increasing the pulse duration by ~60%. This method did not significantly decrease the peak pressure and effectively broadened the shock wave but is not considered a good method for future blast mitigation study. However, the wet sponge drastically lowered the peak overpressure by 54% while significantly increasing both the impulse and pulse duration. These results, in agreement with literature, verify the importance of multiple phases and layers in blast mitigation. Impedance mismatches absorb energy from the blast waves.

The next solid water barrier test involved comparing a PMMA box with and without water. The PMMA box filled with water showed a decrease of peak overpressure by 14%, a decrease of impulse by 42% and a decrease in pulse duration of roughly 50%. The empty box (no water) performed better at diminishing the peak over pressure (~56%) and slightly less at decreasing the impulse (~25%). In contrast, the pulse duration was broadened by 27% in this case. The empty box performed better than the box full of water due to impedance mismatches. The empty box has two interfaces with a significant impedance mismatch (air-PMMA and PMMA-air) while the box full of water only has one (air-PMMA). The second interface (PMMA-water) does not play a significant role in blast mitigation due to the similar densities of water (1 g/cm^3) and PMMA (1.2 g/cm^3).

The latest tests to be completed are aimed at evaluating the effectiveness of different water sprays at a blast mitigant. Pressure transducers are placed at interval distances in a given spray so that the attenuation of the shock wave through the multiphase system can be quantified. The “fine mist” spray appears to be more effective decreasing the peak overpressure at close range (1ft) while the “heavy spray” appears to be more effective at distance (4ft). The heavy spray decreases the impulse of shockwaves more in comparison to the fine mist. Additionally, the heavy spray also decreases the wave speed more. Future testing will be dictated by a test matrix that has been developed to independently quantify the mitigation dependence of sprays with droplets size ranging from 10-800 microns, and with flow rates of .06-2.5 GPM per nozzle. In future tests, high speed video and shadowgraphy techniques will be used to visually capture the shockwave-spray interaction.

Details

Experimental Setup

This study uses an explosively driven shock tube to produce shock waves. By utilizing this setup we achieve a repeatable laboratory scale 1-D shock wave. The shock tube, figure 2, consists of the detonation chamber and the high explosive chamber. The two chambers are bolted together so as to separate the high explosive from the fragments produced by the aluminum detonator cap. The two chambers are linked connected by a small hole through which detonation cord is passed. Previous works have used this method to produce shocks with success (1). Figure 1 shows a typical laboratory produced shockwave imaged using shadowgraphy.



Fig 2: Explosively driven shock tube (1)

Solid Water Barrier Tests

Sponge Test Setup

The solid water barrier experiments performed consist of two parts. First, the mitigation ability of a wet sponge and dry sponge was investigated using the setup seen in figure 3. In these experiments, a sponge was placed in front of a pressure transducer on a test plate. A second transducer was also placed on the test plate to take reference measurements for comparison.

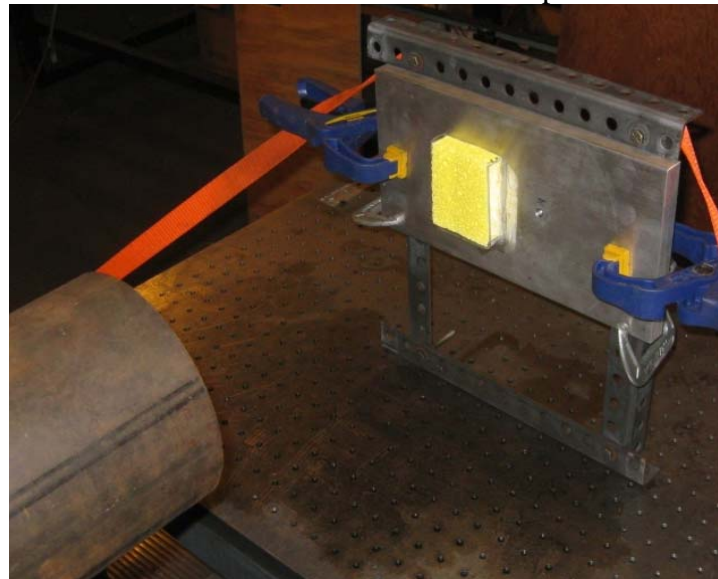
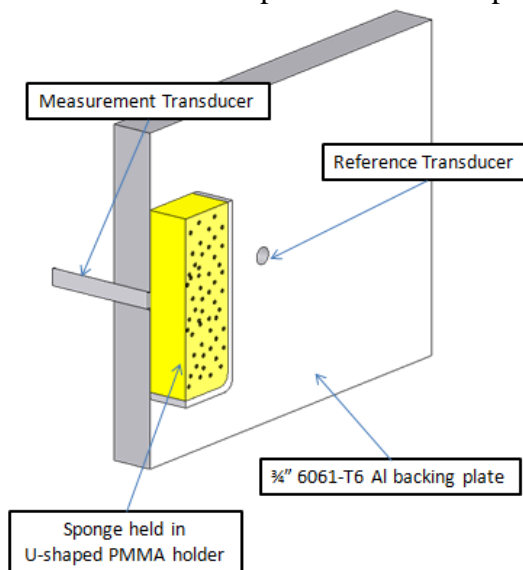


Fig. 3: Sponge mitigation setup

Sponge Test Results

Figure 4 shows the recorded pressure profile for the plate reference, dry sponge and a wet sponge tests. Important pressure profile characteristics have additionally been summarized in Table 1.

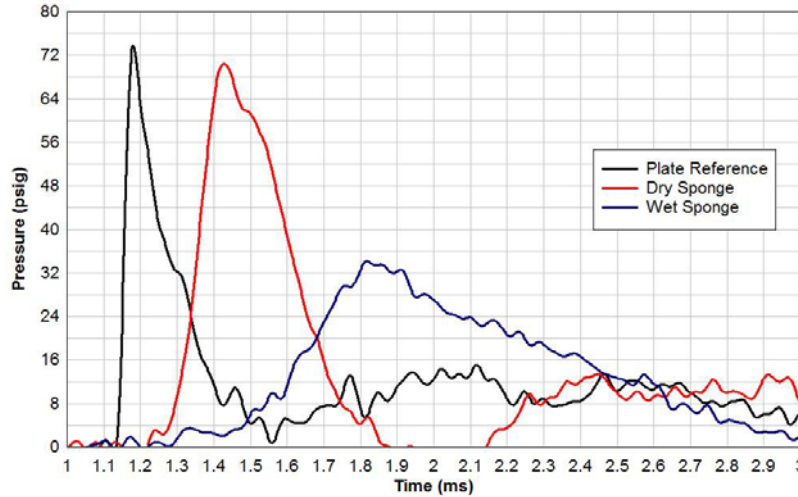


Fig. 4: Sponge Tests Pressure Profiles

Table 1: Summarized Sponge Test Results

Test	Peak Pressure (psig)	Impulse (psig-ms)	Positive Pulse Duration (ms)
Plate Reference	73.67	10.41	.42
Dry Sponge	70.34	19.01	.67
Wet Sponge	34.07	25.03	1.81

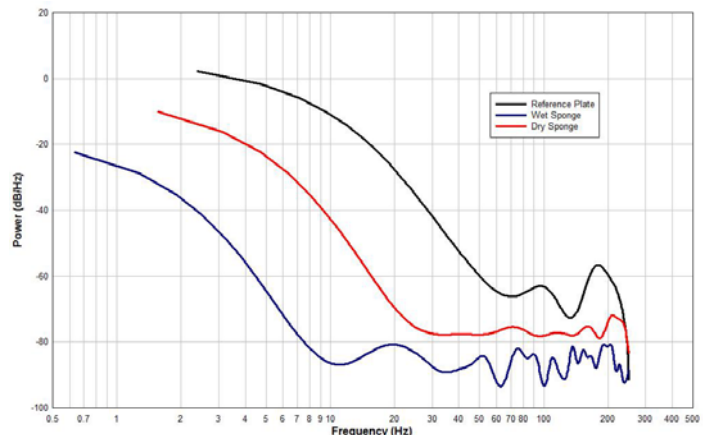
In comparison to the reference gauge, the dry sponge slightly lowered the peak overpressure (4.5%) while increasing the impulse (90%) and pulse duration (~60%). However, the wet sponge drastically lowered the peak overpressure (54%) while significantly increasing both the impulse and pulse duration. A delay in transmission of the shockwave is also seen as an x-axis offset. Figure 5 shows the power spectral density (PSD) of the positive pulse of the reference measurement, dry sponge and wet sponge tests. The wet sponge has contribution from the lowest frequency of all the tests and also has the largest pulse length. This relationship is expected and verifies our results due to the known relationship between low frequency contribution and impulse magnitude (2).

All PSD plots were calculated using the following formula:

$$(1) \quad P(dB) = 20 \log \frac{P}{P_{ref}}$$

Where: $P_{ref} = 14.7$ psi

Fig. 5: Sponge Test's PSD



An important physical observation from these tests was that though the wet sponge was not constrained, no water “squeezed out” due to the shock wave. This was verified by weighing the sponge immediately before and after test to verify no mass deficit.

Solid Water Barrier Test Setup

The second part of the solid water barrier tests utilized a similar setup, Figure 6. During these experiments a sample of water was held in place via a PMMA box instead of using a sponge. Again, a second transducer was used so as to have a reference measurement of the wave so as to make a comparison on the mitigation effectiveness.

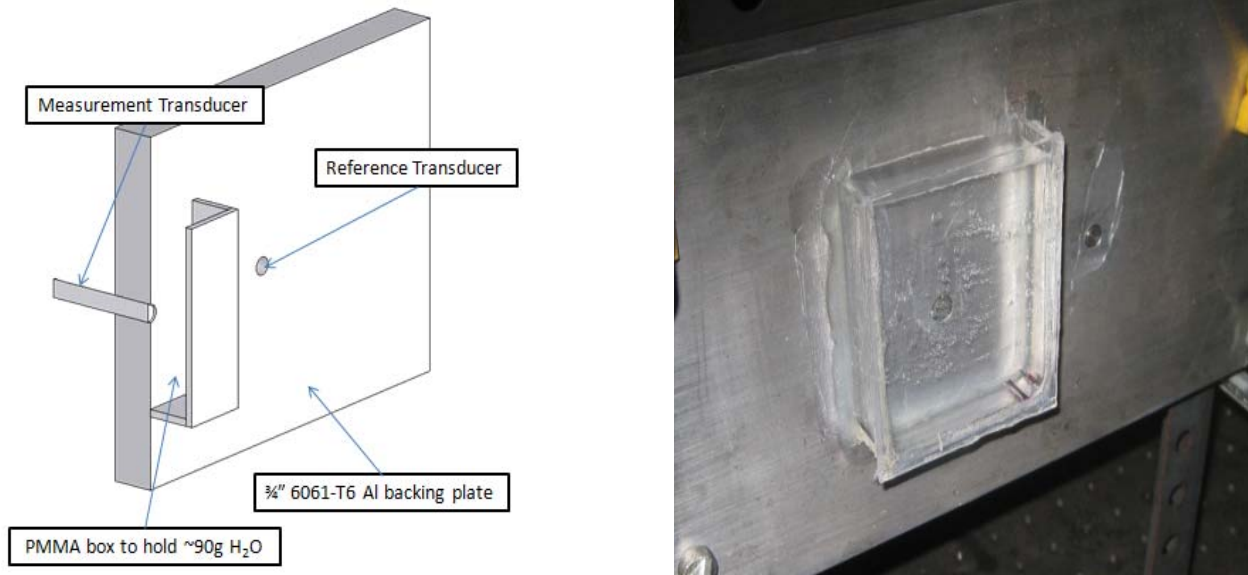


Fig. 6: Solid water barrier setup

Solid Water Barrier Test Results

Figure 7 shows the recorded pressure profile for the free field reference, dry sponge and a wet sponge. Important pressure profile characteristics have additionally been summarized in Table 2.

Fig. 7:- Solid Barrier Tests Pressure Profiles

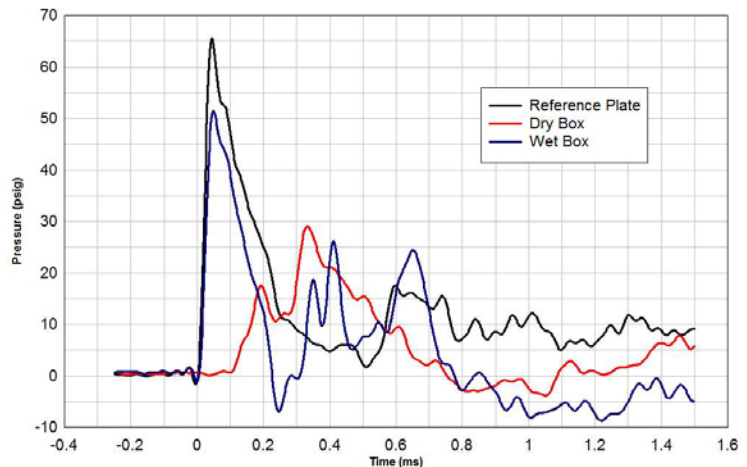


Table 2: Solid Barrier Summarized Results

Test	Peak Pressure (psig)	Impulse (psig-ms)	Positive Pulse Duration (ms)
Plate Reference	65.54	10.72	.51
Dry Box	28.78	7.95	.65
Wet Box	51.26	6.20	.23

The PMMA box filled with water showed a decrease of peak overpressure by 14%, a decrease of impulse by 42% and a decrease in pulse duration by roughly 50%. The empty box (no water) performed better at diminishing the peak over pressure (~56%) and slightly worse at decreasing the impulse (~25%). In contrast, the pulse duration was broadened by 27% in this case.

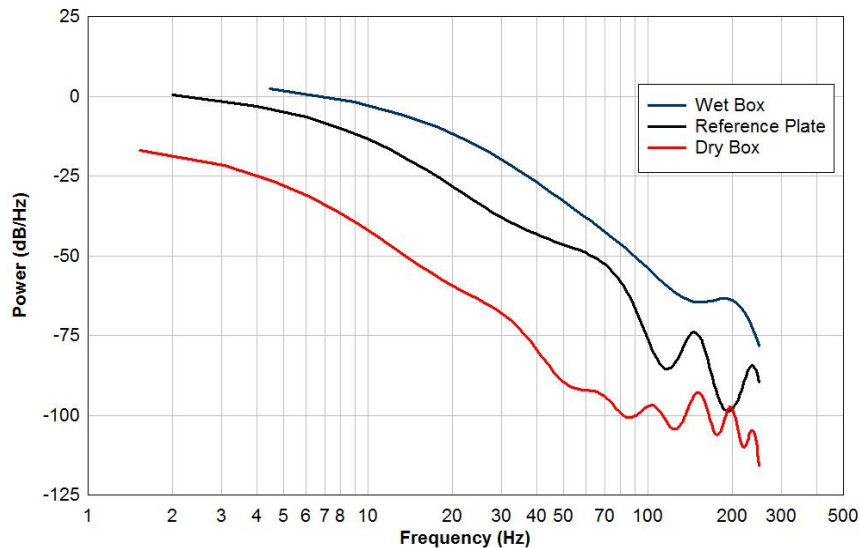


Fig. 8:- Solid Barrier Tests PSD

Figure 8 shows the power spectral density (PSD) of the positive pulse of the free field, dry box and wet box tests. The dry box has the most contribution from the low frequencies of all the tests and also has the largest pulse length.

Incompressible fluid between plate and box “lid” leads to less transmission loss than expected. The reason the empty box performed better than the box full of water can be explained by impedance mismatches. The empty box has two interfaces with a significant impedance mismatch (air-PMMA and PMMA-air) while the box full of water only has one (air-PMMA). The second interface (PMMA-water) does not play a significant role in shock wave mitigation due to the similar densities of water (1 g/cm^3) and PMMA (1.2 g/cm^3). More effective mitigation may be achieved by allowing the water to be displaced. This will be tested via water sheet mitigation.

Water Spray Mitigation

The latest tests to be completed are aimed at evaluating the effectiveness of different water sprays at a blast mitigant. An elaborate spray system has been designed, built and initial results are presented here. Pressure transducers are placed at interval distances in a given spray so that the attenuation of the shock wave through the multiphase spray system can be quantified.

Spray Mitigation Setup

The spray system, Figure 9, was designed and built so that a variety of water sprays can be produced in conjunction with the shock tube used in previous experiments. A test matrix has been developed to independently quantify the mitigation dependence of sprays with droplets size ranging from 10-800 microns and with flow rates of .06-2.5 GPM per nozzle.

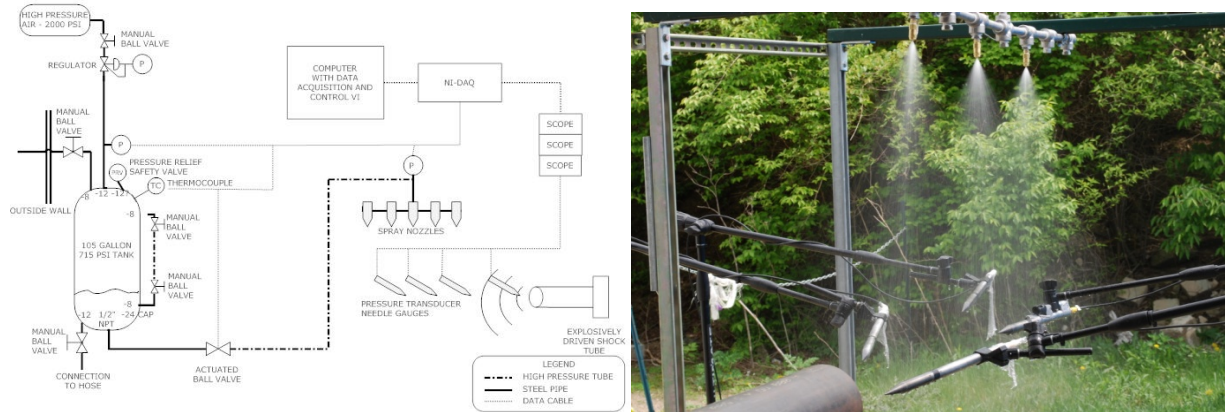


Fig. 9:- Spray Mitigation Setup

Spray Mitigation Results

Initial results show contrast between different sprays of different types. Figures 10-12 show various characteristics of the laboratory produced shock waves in a free field test (no spray), with a “heavy spray” (Fulljet Nozzle) and a “fine mist” (Fogging nozzle). Table 3 shows the spray characteristics of these different sprays. Future testing will include more accurate characterization of the sprays by using Phase Doppler Anemometry (PDA). PDA testing will be especially useful in determining the number density of a spray since the spray velocity is much smaller than the shock wave speed.

Table 3:- Spray Parameters

Test	Flow Rate (gpm)	Droplet Size (microns)
Fogging Nozzle	0.245	~10-100
Full jet	1.2	~800

Figure 10 shows how these two different sprays affect the peak overpressure. The fine mist appears to be more effective at close range (1ft) while the heavy appears to be more effective at distance (4ft). Further testing will quantify this in detail as well as minimize scatter by improving our pressure transducer placement and improved data processing techniques. Figure 11 shows that the heavy spray lessens the impulse of the shock better. Additionally, Figure 12 shows that the heavy spray decreases the wave speed of the shock wave while the fine mist has

no effect. The initial results show that heavy sprays absorb more energy. As testing continues, the mechanisms of energy transfer will be investigated closely. Some methods of quantifying energy transfer include:

- Kinetic energy calculations via droplet velocity measurements from high speed imaging
- Wave speed calculation via high speed pressure measurements

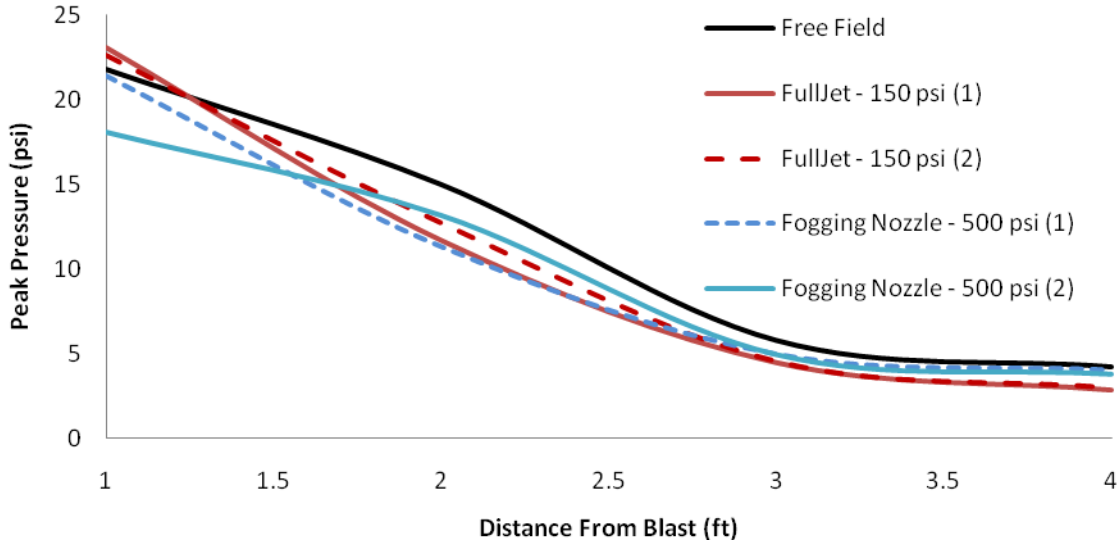


Fig. 10: Peak Overpressure Spray Comparison

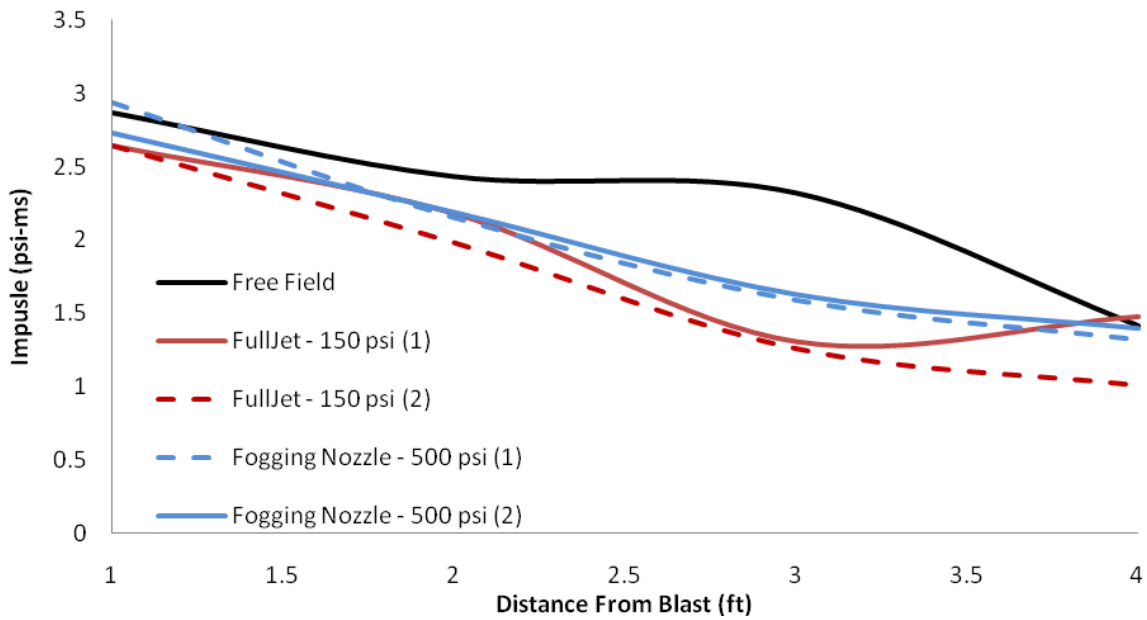


Fig. 11: Impulse Spray Comparison

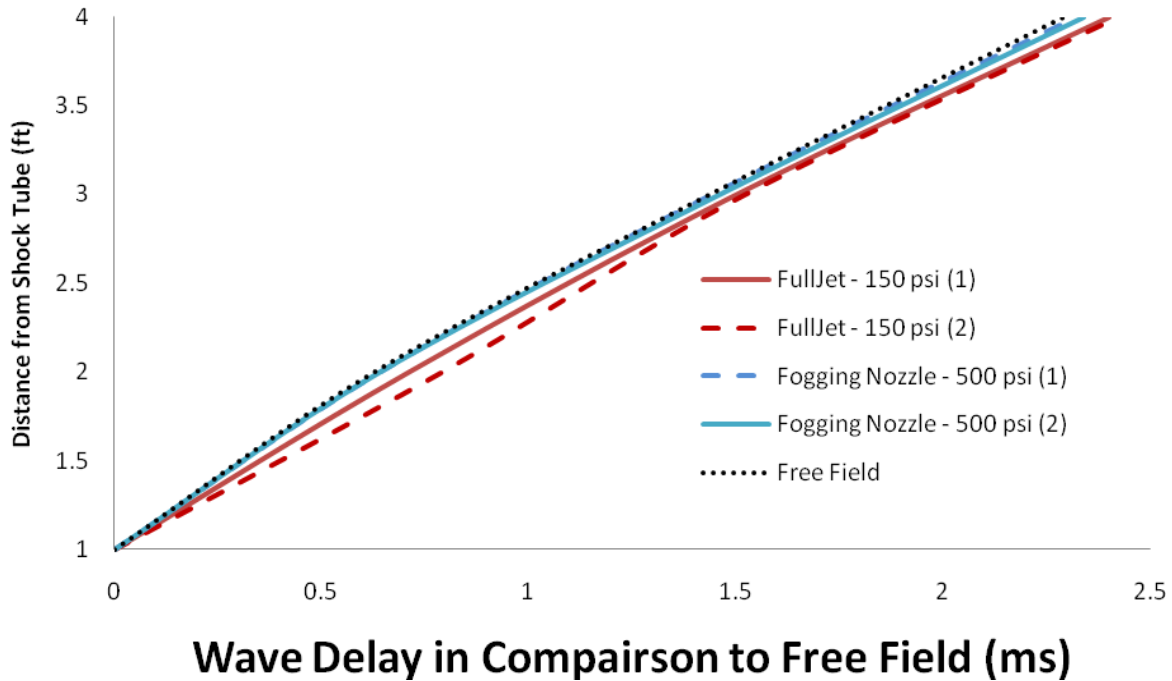


Fig. 12: Shock Wave Delay

The wave delay in Figure 12 is calculated by measuring the time elapsed from the trigger. Current the pressure transducer at 1 foot is used to trigger but future testing will be trigger from the exit of the shock tube.

Continuing Work

With initial spray mitigation tests complete, plans for continued work have been identified. In order to accurately classify the various sprays, personnel are being trained to use Phase Doppler Anemometry (PDA). This will allow precise characterization of spray parameters like droplet size and spray number density. This is especially important because simply varying the flow rate may not vary the mitigation ability of a spray. The speed of a shock wave through a spray is so much larger than the droplet velocity that the timescale of shockwave-droplet interaction is small. Therefore, independent variables for continuing work will be droplet size and number density.

Before continuing with testing of a large variety of sprays, two methods for improving the fidelity of the data have been identified. An effort will be made to reduce signal noise by minimizing shock reflections between various pressure transducers in the test field. Also, data analysis techniques are being reviewed to avoid errors in calculating peak overpressure, impulse and positive pulse duration.

Additionally, the PSD of the pressure profiles from various sprays will be analyzed. Since initial results show that the impulse of the shock wave change based on different sprays, the PSD is expected to be of interest.

Additionally, by changing the length of the shock tube we have proven that we can change the frequency characteristics of the shock wave. This will allow us to test the various water mitigation techniques against characteristically different shock waves.

At the conclusion of spray testing, other water mitigation configurations will also be explored. Similar to the water barrier tests, water sheets will be investigated. In these tests, water will not be constrained from being displaced via momentum transfer. "Waterfalls" of varying thickness will be placed in series to test the mitigation effectiveness of this configuration. High speed images of shock wave interactions with single droplets will also be investigated.

Students Supported



David Reese (Partially Supported)



Eric Miklaszewski (Partially Supported)

Conference & Journal Publications

- Conference paper in progress

Works Cited

1. Alley, Matt D. "Explosive Blast Loading Experiments for TBI Scenarios: Characterization and Mitigation." Thesis. West Lafayette, IN / Purdue University, 2009. Print.
2. Petukhov, Yu V. "Change in Shock-Wave Pressure Impulse with Distance Near the Source." *Zhurnal Prikladnoi Mekhaniki I Tekhnicheskoi Fiziki* (1985): 102-06. Web.

Self Healing Materials for Autonomic Mitigation of Blast Damage

Nancy R. Sottos; Scott R. White; Jason F. Patrick
University of Illinois at Urbana-Champaign

Objective

This document outlines research conducted at the University of Illinois over the past nine months, in regards to the development of self-healing materials for autonomic mitigation of blast-induced damage. The goal of this project is to develop self-healing composite systems for mitigation of blast damage over a variety of platforms including civil based infrastructure and aerospace vehicles. The intended outcome of this research will not only address issues directly related to protection and recovery of blast-induced damage but also contribute to scientific advancements in the realm of polymer composites. A concise list of research accomplishments motivated by the aforementioned objectives is provided below:

Tasks Accomplished

- Survey of literature pertaining to self-healing polymeric materials and state-of-the-art composite structural systems used for blast protection.
- Selection of ideal system in regards to blast mitigation performance and realistic integration of self-healing technology.
- Extension of current microencapsulation techniques to include expansive foam healing chemistries suitable for larger scale blast damage (Details I).
- Design and fabrication of a shear test fixture to induce damage under quasi-static loading conditions in order to assess healing performance in a standard lab setting (Details II).

Summary

Our first milestone was to develop initial specifications for a self-repairing material system based on modern structural requirements for blast resistant composite structures. We completed a comprehensive survey of state-of-the-art materials and potential failure modes for blast resistant composite structures.¹⁻⁶ Based on our review of the literature in this area, we identified 3D woven composite sandwich structures as primary candidates for integration of self-healing functionality.⁷⁻¹² The unique architecture of 3D woven sandwich panels is favorable for seamless integration of current self-healing technology with little impact on initial mechanical properties. Novel composite sandwich panel configurations such as Transonite® make use of 3D woven E-glass composite skins separated by a polymeric foam core and rigidly connected by through thickness fiber insertions. These panels have been shown to withstand 5 lbs of C4 explosive detonated at a mere 3 ft standoff distance. Depending on the through thickness fiber stitching density, primary failure modes after shock loading include delamination of the face sheets from the core, microcracking in the 3D woven composite face sheets, and shear failure of the foam core.

In our initial work, we have chosen to focus on core damage and the development of a *self-healing polymeric foam*. Blast events predominantly cause the foam core to fail in shear,

significantly reducing structural stiffness and sandwich efficiency of the composite system. Self-healing of core damage will enable recovery of stiffness and should result in enhanced resistance to multiple blast events. Conventional polyurethane (PUR) and polyisocyanurate (PIR) foam cores are condensation materials prepared from organic polyisocyanates, polyols, catalysts, surfactants, and a foaming or blowing agent. In typical foam formulations, the polyisocyanate compound is referred to as Part A whereas the remaining materials constitute Part B. Our strategy is to develop a two capsule system, Part A and Part B, and disperse these capsules throughout the foam core. Blast-induced shear damage to the core will trigger rupture of the capsules, causing the components to come in contact and react to regenerate the foam scaffold. The foaming reaction depending upon stoichiometric ratios can result in a volumetric expansion of up to 20 times, making this an ideal system for healing large, blast induced damage. We have focused our initial efforts on encapsulating the Part A (polyisocyanate) foam component, due to some previous work¹⁰ within our research group.

We have also recently designed and fabricated a shear test fixture according to ASTM C273 - Standard Test Method for Shear Properties of Sandwich Core Materials¹³, in order to induce damage in polymeric foams. This experimental set-up will allow us to assess healing performance in a standard laboratory setting, under quasi-static loading conditions.

In the second phase of this project, we intend to incorporate a bio-inspired microvascular network into the 3D woven composite face sheets. The microvascular approach allows for the continuous delivery of healing agents, enabling multiple healing cycles of large volume damage regions. The two-step proposed self-healing sandwich methodology is graphically outlined in Figure 1 below.

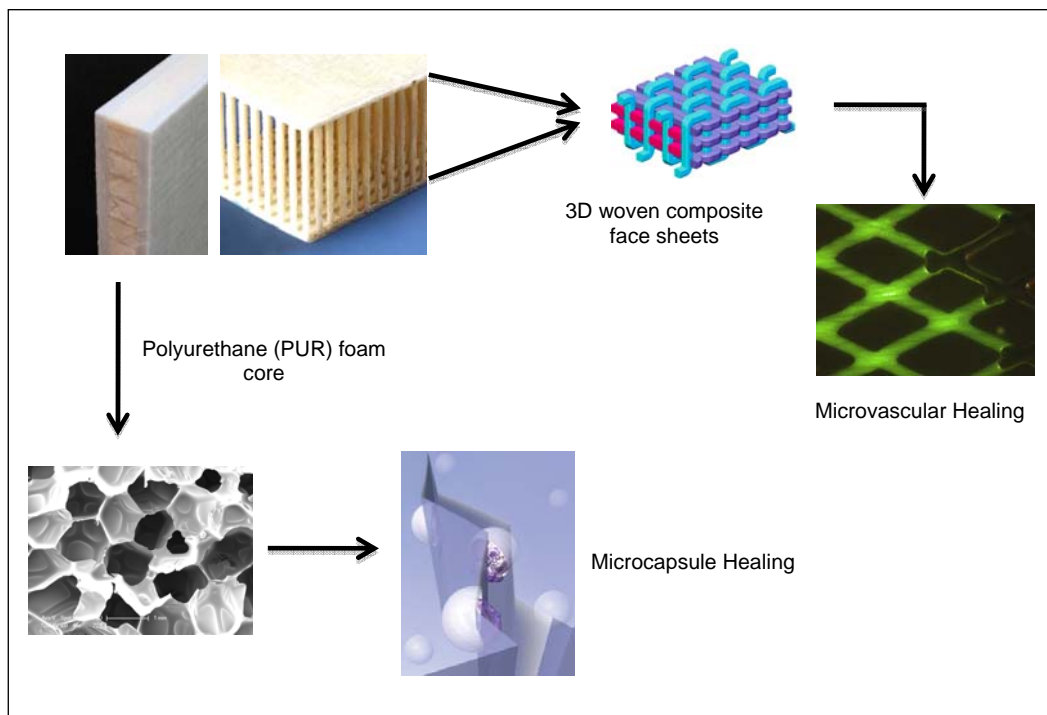


Figure 1. Proposed self-healing sandwich panel methodology

Details I: Microencapsulation of Foam Healing Agents

In progress to date, we have successfully encapsulated the polyisocyanate component, or Part A of the foam self-healing chemistry. Initial efforts focused on the encapsulation of a less reactive, aliphatic isocyanate, Isophorone Diisocyanate IPDI. Modification of a published encapsulation technique¹⁰, allowed for the in-situ polymerization reaction to be performed using commercially available materials. The IPDI microcapsules were then incorporated into a polyurethane (PUR) foam core to assess survivability and rupture capability upon damage initiation. Figure 2 shows an optical image taken at 5x magnification of an IPDI microcapsule embedded in the PUR foam core material. The capsule not only survived the foaming process but also remained bonded and intact after careful sectioning of the PUR foam. However, successful healing can only be achieved by the release of healing agents contained in the core of the microcapsules. Figure 3 demonstrates the ability of the IPDI capsules to rupture and release healing agent (blue) upon damage initiation to the PUR foam. Thus this preliminary investigation revealed the viability of using a microcapsule-based approach to self-healing in cellular foam materials.

Aliphatic diisocyanates such as IPDI are not used specifically in the production of polyurethane foam but rather in coating applications that require resistance to abrasion and deterioration from UV light. A more reactive, aromatic compound, Methylene Diphenyl Diisocyanate MDI, is used directly in the production of both polyurethane (PUR) and polyisocyanurate (PIR) foams. Polyisocyanurate foams are essentially an improvement of polyurethanes, requiring a higher proportion of MDI and the reaction takes place at elevated temperatures. This research investigation is focused on self-healing PUR foams, due to the more favorable processing conditions.

All isocyanates are moisture sensitive and polymerize in the presence of water. The low reactivity of the aliphatic IPDI made it possible to form a shell wall via an in-situ polymerization reaction in an aqueous emulsion. The same encapsulation technique was performed using aromatic MDI as the core material but resulted in solid spheres instead of capsules. Thus, an entirely new encapsulation methodology was developed. Using Silicon Oil as the continuous phase, a stable emulsion of MDI was achieved by agitation at a rate of 800 RPM. Titration of a silicon oil soluble, mono-functional amine, 3-aminopropyltrimethoxysilane, into the emulsion resulted in the formation of a polyurea shell wall around an MDI core. An optical image of the MDI microcapsules taken at 5x magnification is shown in Figure 4. Presence of MDI in the core of was confirmed by Fourier Transform Infrared (FTIR) spectroscopy. In addition, a small amount of capsules were crushed on a glass slide to which a droplet of a commercial Part B foam component was added. The sequence of images (a-d) in Figure 5, show the “micro” foaming process and also confirm the presence of MDI. Thus we have demonstrated the ability to create PUR foam from an encapsulated Part A.

The newly developed encapsulation technique is the first of its kind and although successful, it requires an in-depth parametric study in order to optimize the process and produce high quality capsules for self-healing. Work is in progress to improve the encapsulation procedure, assess the stability of these capsules, and develop a process to incorporate them into a foam core. Future work under this phase of the project will also involve the encapsulation of Part B foaming components: polyols, catalysts, surfactants, and blowing agents. We are currently investigating the possibility of using micro fluidic encapsulation devices to accomplish this objective.

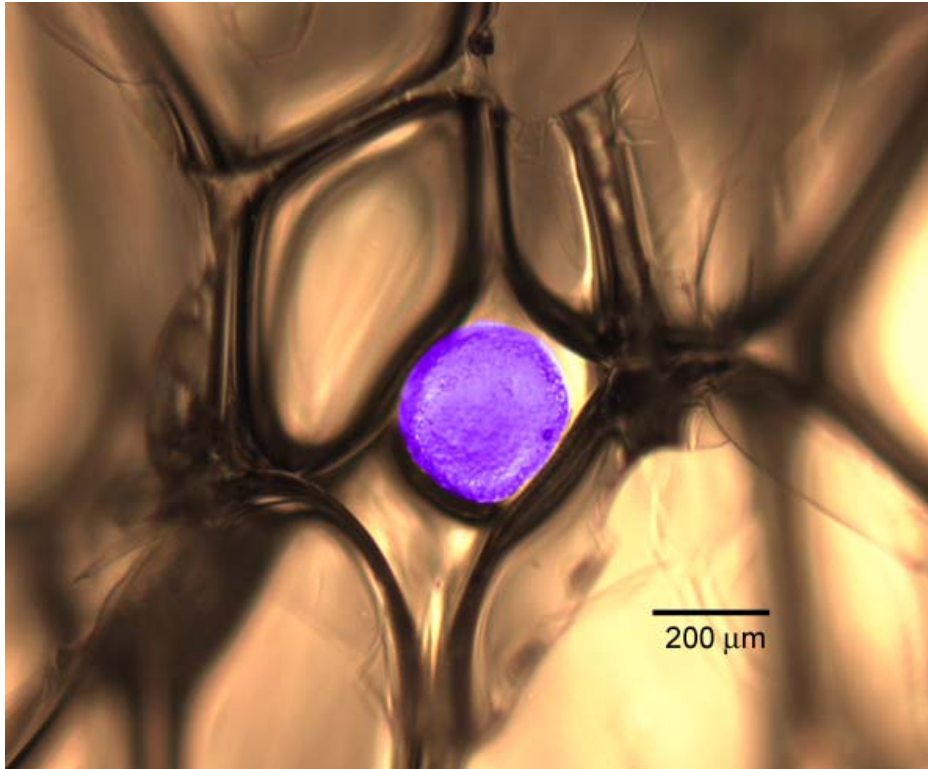


Figure 2. Intact IPDI microcapsule in PUR foam

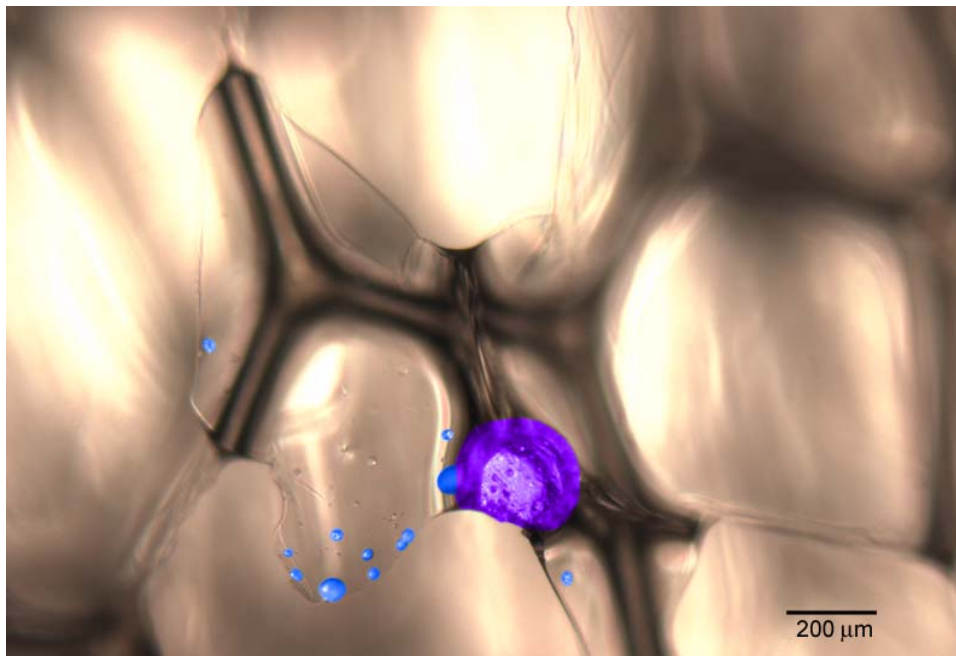


Figure 3. Ruptured IPDI microcapsule showing release of core

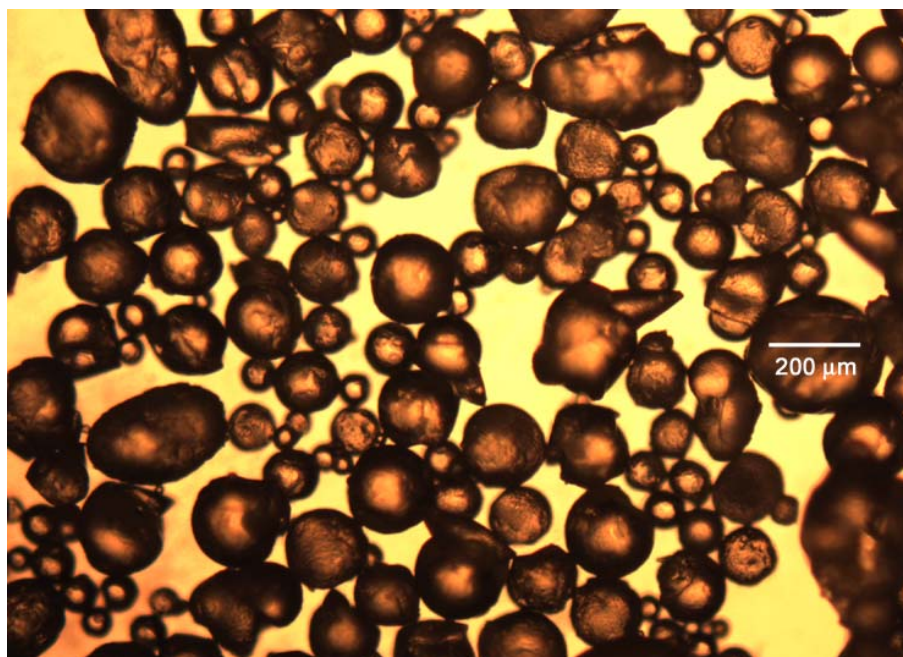


Figure 4. Optical image of MDI microcapsules taken at 5x magnification

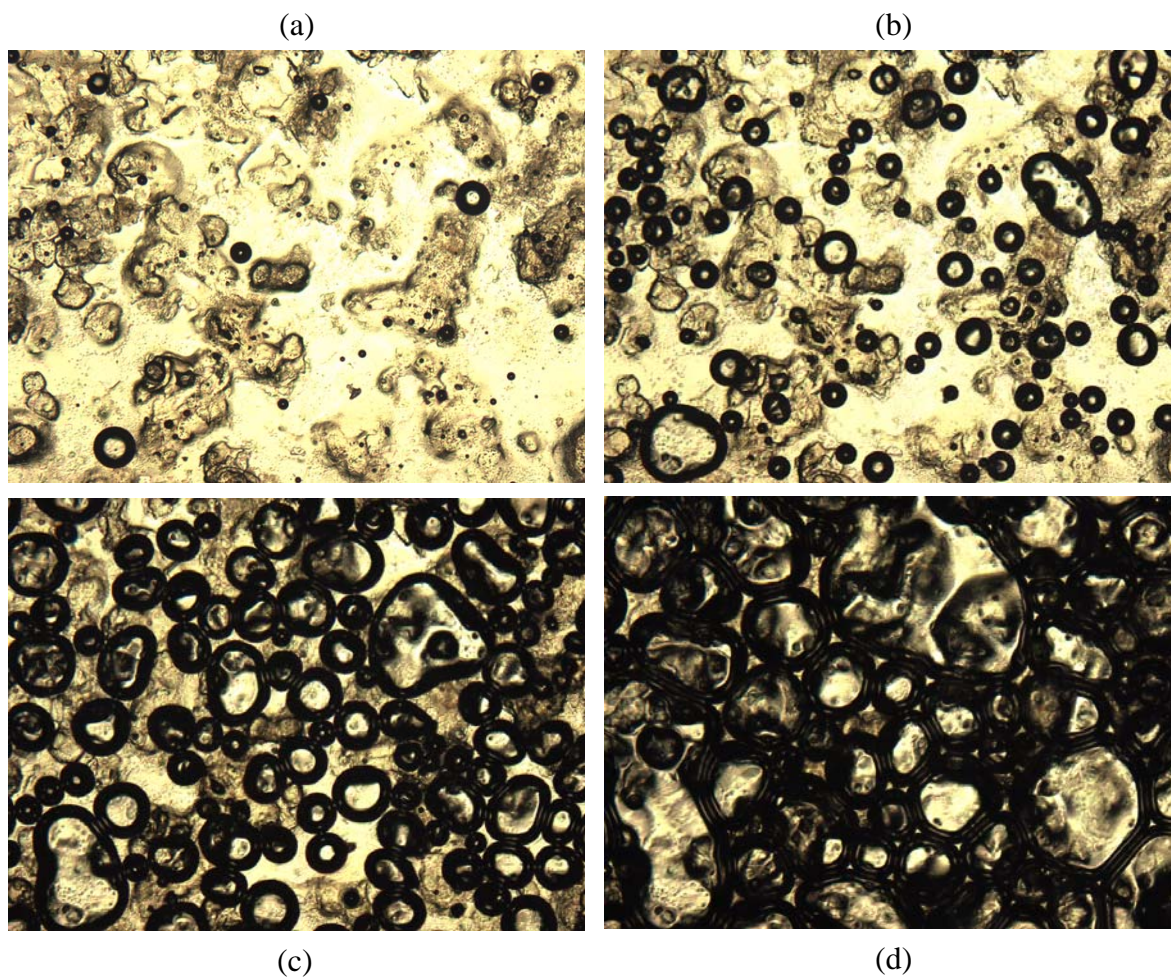


Figure 5. Foam production by placing droplet of Part B on crushed MDI capsules

Details II: Mechanical Evaluation of Foam Core

Based upon a previous research investigation⁴ of Transonite® sandwich panels and the dominant failure modes provided in the literature, we have developed a mechanical testing protocol to induce damage in PUR foam cores based on ASTM C273 - Standard Test Method for Shear Properties of Sandwich Core Materials¹³. A scaled down version of the ASTM recommended test fixture has been designed, fabricated, and assembled in our laboratory at the Beckman Institute. A 3D nonlinear Finite Element Analysis was performed using Abaqus CAE to determine appropriate specimen dimensions that would minimize secondary stresses, per ASTM recommendations. The load cell and displacement sensor have been incorporated into the data acquisition (DAQ) hardware via Omega digital signal processing units and National Instruments LabView software package. Figure 7 shows graduate student, Jason Patrick, ensuring proper sensor functionality and alignment of a foam specimen prior to testing. A preliminary test was performed on a commercial Trymer® 3000 PIR foam, shown in Figure 8 with multiple shear (Mode II) fractures along the length. Upon load removal, the induced shear cracks decrease in separation distance and become barely visible, as depicted in Figure 10. However permanent damage has occurred to the polymeric foam core. Thus, this quasi-static test is an efficient, inexpensive, and repeatable procedure to “simulate” blast damage in PUR foam materials used in sandwich structures. In addition, the crack closure characteristics of the foam upon unloading make this an ideal methodology for evaluation of self-healing.

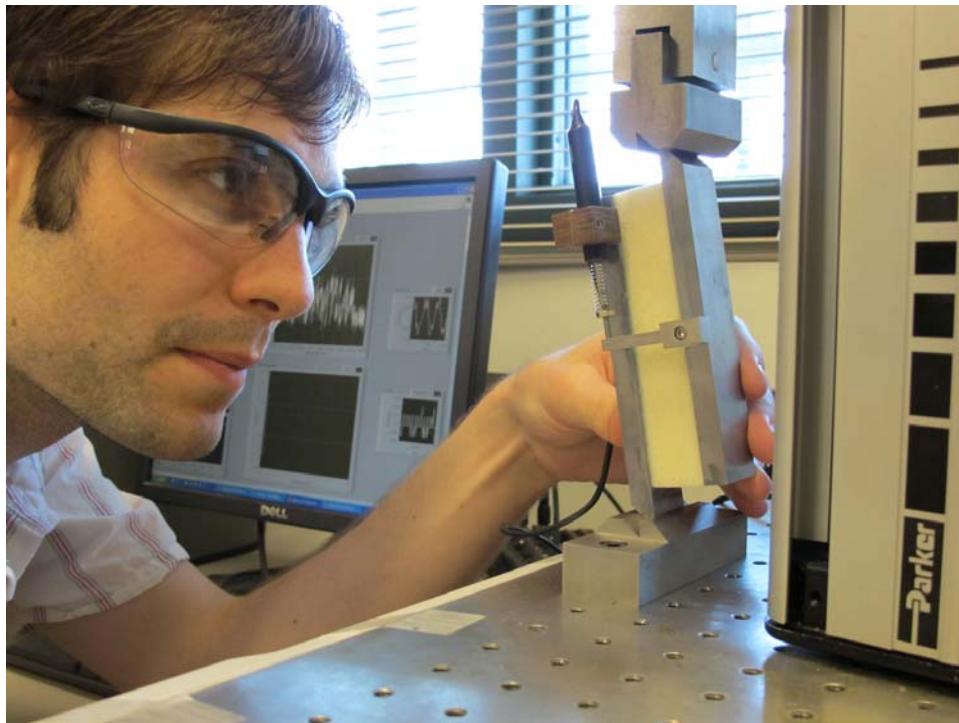


Figure 7. Assembled shear test fixture in Beckman laboratory at the University of Illinois

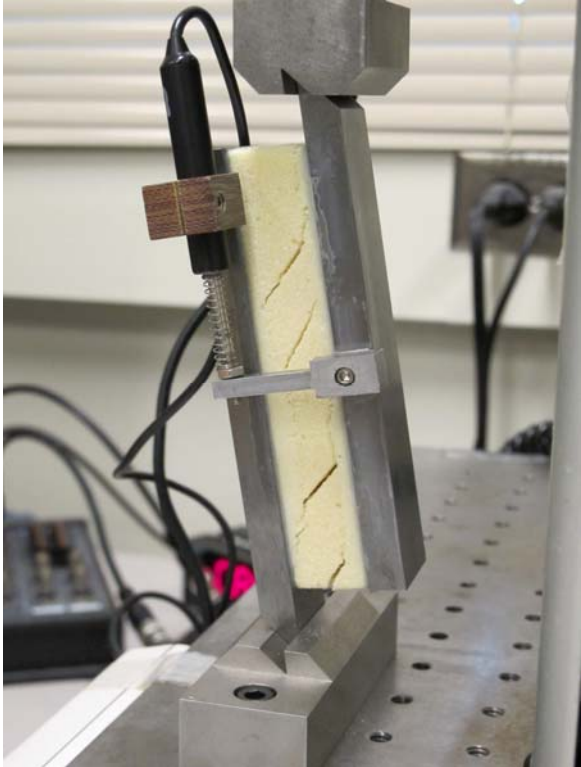


Figure 8. ASTM C-273 shear test of Trymer[®] 3000 PIR foam with Mode II fractures

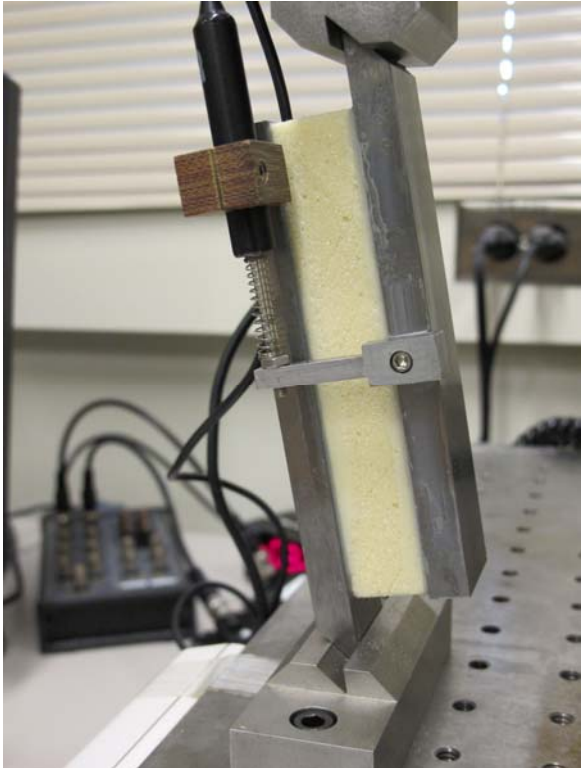


Figure 9. Closure of shear cracks in Trymer[®] 3000 specimen after unloading

References

1. J.N. Baucom, M.A. Zikry. Evolution of Failure Mechanisms in 2D and 3D Woven Composite Systems under Quasi-static Perforation. *Journal of Composite Materials*, Vol. 45 (2003)
2. J. LeBlanc, A. Shukla, C. Rousseau, A. Bogdanovich. Shock Loading of three-dimensional woven composite materials. *Composite Structures*, Vol. 79 (2007)
3. J. Grogan, S.A. Tekalur, A. Shukla, A. Bogdanovich, A. Coffelt. Ballistic Resistance of 2D and 3D Sandwich Composites. *J Sandwich Structures and Materials*, Vol. 9 (2007)
4. Patrick, J. (2007). "Fundamental Characteristics of 3-D GFRP Pultruded Sandwich Panels." M.S. Thesis, Department of Civil and Environmental Engineering, North Carolina State University, Raleigh, NC.
5. Bogdanovich, A. E., and M. H. Mohamed. Three-Dimensional Reinforcements for Composites, *SAMPE Journal*, vol. 45 (2009)
6. S.A. Tekalur, A. Bogdanovich, A.E. Shukla. Shock loading response of sandwich panels with 3-D woven E-glass composite skins and stitched foam core. *Composites Science and Technology*, Vol. 69 (2009)
7. White S.R., Sottos N.R., Geubelle P.H., Moore J.S., Kessler M.R., Sriram S.R., Brown E.N., Viswanathan S. Autonomic healing of polymer composites. *Nature* 409, 794-797 (2001)
8. Kessler M.R., Sottos N.R., White S.R. Self-healing structural composite materials. *Composites: Part A* Vol. 34, 743–753 (2003)
9. Toohey, K.S., Sottos, N.R., Lewis, J.A., Moore, J.S.; White, S.R. Self-healing materials with microvascular networks, *Nature Materials*, 6, 581-585 (2007)
10. Yang, J., Keller, M.W., Moore, J.S., White, S.R.; Sottos, N.R. Microencapsulation of Isocyanates for Self-Healing Polymers, *Macromolecules*, 41, 9650-9655 (2008)
11. Blaiszik, B., Caruso, M., McIlroy, D., Moore, J., White, S.; Sottos, N.R. Microcapsules filled with reactive solutions for self-healing materials, *Polymer*, 50, 990-997 (2009)
12. Toohey, K.S., Hansen, C., Lewis, J.A., White, S.R. and Sottos, N.R. Delivery of two-part self-healing chemistry via microvascular networks, *Advanced Functional Materials*, 19, 1399-1405 (2009)
13. ASTM C273 / C273M - 07a, "Standard Test Method for Shear Properties of Sandwich Core Materials," *Book of ASTM Standards*, American Society for Testing and Materials, Vol. 15.03

Self-Healing Concrete

Arijit Bose

University of Rhode Island

Objective:

Develop a new class of concrete that has self-healing properties. This will prolong the life-time of the concrete, prevent catastrophic failure, and reduce rebar corrosion.

Accomplishments:

A new concrete mixture has been developed containing polyurethane capsules with sodium silicate solution. This concrete shows ~25% recovery of flexural strength after stressing to failure. This is compared to ~10% recovery in control samples, demonstrating the self-healing nature of these materials. No loss in compression strength has been observed. Corrosion is also inhibited significantly. The penetration of the sodium silicate into cracks upon breaking the microcapsules and the formation of a CSH complex in those regions is responsible for this healing action.

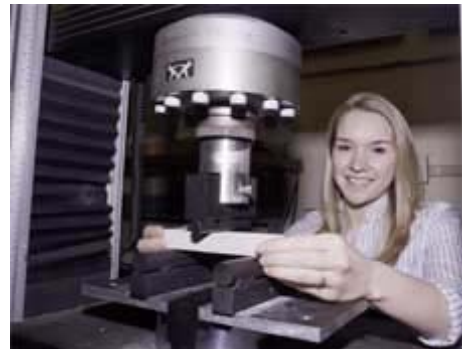
Details:

Details are provided in the attached manuscript, to be submitted shortly to the Journal of Concrete Research.

Students Supported:

Michelle Pelletier, M.S. June, 2010.

Michelle Pelletier, a graduate student in chemical engineering working with Professor Arijit Bose, has developed a unique self-healing concrete that may increase the life of bridges, foundations and sidewalks. Numerous online news and industry websites have reported on her discovery, including [Providence Business News](#), [The Chemical Engineer Today](#), [The Engineer](#), [R&D Magazine](#), [Homeland Security News](#), [Daily Tech](#), [Science Daily](#), [E Science News](#), and many more.



Conference & Journal Publications

Self-healing concrete, M. Pelletier, A. Bose, MRS Meeting, Boston, 2009

Self-healing concrete, M. Pelletier, A. Shukla, A. Bose, IMPLAST 2010, Providence, 2010.

Self-healing Concrete – recovery of flexural strength and corrosion resistance, M. Pelletier, A. Shukla, A. Bose, to be submitted to *J. Concrete Research*, July 2010.

Goals and objectives for 2010-11

- (i) Expose microcapsule containing concrete to blast loading conditions and examine dynamic mechanical properties
- (ii) Fill capsules with soft gel materials to analyze energy absorption capacity under dynamic loading conditions
- (iii) Optimize capsule size, polyurethane shell thickness and microcapsule loading to provide maximum recovery.
- (iv) Fill capsules with calcium nitrite solution and examine corrosion resistance upon stressing to failure.

Self-healing concrete with a microencapsulated healing agent

Michelle M. Pelletier and Arijit Bose
Laboratory of Soft Colloids & Interfaces, Department of Chemical Engineering
University of Rhode Island, Kingston, RI, USA

Corresponding Author: Arijit Bose, Ph.D.
Department of Chemical Engineering
University of Rhode Island
217 Crawford Hall, 16 Greenhouse Rd.
Kingston, RI, 02881, USA
Phone: +1-401-874-2804
Fax: +1-401-874-4689
Email address: bosea@egr.uri.edu

2.1 Introduction

In order to be considered a smart or self-healing material, the concrete must have the ability to repair damages caused by an environmental stimulus over time. Generally, a self-healing system is developed by having some sort of a contained repair agent that is made readily available. The agent is used when an external stimulus, typically stress, initiates its release and the appropriate environment promotes healing.

2.1.1 Self-healing systems

Smart concrete is a way to utilize and promote further self-healing than what is naturally done by the material. A more conventional method of self-healing of concrete incorporated an expansive chemical admixture into the mix [1]. Their results showed a significant decrease in the water permeability rate through the porous structure, but did not show sufficient self healing within the material. Researchers from Japan developed a self-healing material requiring a heating device [2-4]. A small, film-like pipe or hollow, brittle, glass pipes (**Figure 1**) containing a repair agent is embedded into the concrete. When a crack occurs and with suitable heating from an outside source, the film melts or glass pipes break to release the healing agent, which in turn is hardened by the applied heat to heal and fill the crack. Though seemingly effective, the limitations to this method are that the pipes require selective heating, which is virtually impossible for internal cracks that could be deep in the infrastructure. Such high heat may have adverse effects to localized areas of concrete surrounding the pipe. Finally, this type of system is difficult to do on the bulk scale, which would be required for structures requiring large amounts of material. Similarly, Mihashi and Yoshio proposed incorporating glass pipes containing the repairing agent into the concrete for self-healing capabilities to restore strength and for the prevention of water leakage [5]. This same concept was also displayed by Li et al. who incorporated hollow glass fibers containing ethyl cyanoacrylate, a superglue-type thermoplastic monomer, into the mix [6]. Their experiments were able to confirm the rupture of the hollow

fibers as well as the release of the healing agent. Self-healing is confirmed by analyzing the elastic modulus of the sample. It was discovered that the healing agent was able to restore the material back to its original strength after repeat loading with damage occurring in the first cycle. This hollow-fiber method has been successful in other concrete systems as well as reinforced polymers and epoxies [7-13]. A newer method being explored is to use bacteria as a healing agent [14-16]. Self-healing is achieved by incorporating different types of bacteria that are capable of precipitating calcium carbonate to heal cracks. Results show evidence of increased compressive strengths and decreased water permeability in the samples containing the bacteria.

Another novel, self-healing technique has been achieved involving microcapsules to store the repairing agent until needed. Sottos et al. developed a polymer composite system that incorporates a catalyst into the polymer matrix phase with a microencapsulated repair agent [17]. The healing agent is released upon crack propagation through the microcapsule, resulting in as much as an 80% self-healing efficiency after a fracture. This method has been successful in various polymer composite systems and will be employed in this work [18-20].

2.2 Microcapsules

2.2.1 Encapsulation Methods, Release Mechanisms and Advantages of Microencapsulation

Encapsulation has proven to be a suitable method for self-healing systems. Encapsulation of the healing agent is important for two main reasons. First, it allows for isolation of the agent and protection from the surroundings and potential chemical reactions. Furthermore, it allows for a controlled and targeted release. This is important, especially in a self-healing system, where the ultimate goal is to be able to heal cracks in a specific location as they occur. Yow and Routh [21] published a review of various methods used to encapsulate a liquid core with a polymer shell. These have been used in various applications and include colloidosome formation [22, 23], oil-core encapsulation through phase separation [24-26], layer-by-layer polyelectrolyte deposition [27, 28], polymer growth by surface polymerization [29] and interfacial polymerization [30-32]. The work in this thesis employs interfacial polymerization and the technique will be further discussed later in this chapter.

The type of release of an encapsulated core material is also a property that can be tailored for a particular system. The most simplistic case is when the capsule's shell is ruptured by mechanical stress. Other techniques include dissolving the shell through selective heating, a particular solvent, time-dependent degradation or a chemical reaction or even by reverse transitions, such as capsule swelling [21]. To ensure selectivity, capsules can also be made to rupture in response to environmental changes such as pH [33], light [34, 35] and temperature [36, 37].

Microencapsulation of the healing agent was an attractive method for this self-healing system. First, this technique can be applied to water-in-oil emulsions. This is key since the sodium silicate healing agent is dispersed in the aqueous core and a majority of encapsulation methods are for oil cores. Secondly, interfacial polymerization is one of the simplest procedures for encapsulation when compared to the other methods mentioned previously. Its simplicity allows for quick microcapsule fabrication and also consistency between batches.

2.2.2 Polyurethane Microcapsules

Interfacial polymerization is described as two monomers dissolved in incompatible phases that meet at an interface and react instantaneously [21]. A simple schematic of this process is shown in **Figure 2**. Polyurethane microcapsules are synthesized by the reaction between water and a diisocyanate. They are prepared in a water-in-oil emulsion in which the aqueous phase becomes encapsulated by the polymer shell. Water is dispersed in an organic phase of toluene and the droplets are stabilized by two surfactants. After addition of the diisocyanate, the emulsion is left to react at an optimal time, temperature and shearing rate. The temperature of the reaction is the most important factor since it controls the reaction kinetics, ensuring the rapid formation of the first porous layer and overall maturation of the shell over time [30]. The diisocyanate and water droplets react at the interface of the oil and water, producing a thin shell. Over the reaction time, the shell matures into a full capsule. Each microcapsule consists of a cross-linked polyurethane shell with an aqueous phase healing solution of sodium silicate. The average diameter of the capsules under these conditions is about 373 μm . Capsule size can be controlled by increasing or decreasing the shearing rate for the four hour duration [30].

2.3 Pre-healing crack formation

Rupturing of the capsules and healing is activated by mechanical stress. For experimental purposes, a controlled load is applied to induce cracking within the sample. The cracking is minor and internal only and meant to imitate minor cracking and deformations that occur within the concrete after applied or natural stresses, such as increased loading or creep. Because of the randomized loading and large amount of capsules, it is assumed that each crack will rupture some capsules and allow the healing to take place. After the appropriate healing time has passed, the samples are retested to see how much strength has been maintained after being fatigued and weakened. The capsules are expected to supply enough healing agent to properly heal microscale cracks. This will ultimately result in greater strength post-fatigue since it is reducing the porosity and ultimately restoring that location of the material to its initial state. It is also meant to reduce water permeation further in the material, which in turn would reduce corrosion in structures containing steel reinforcement bars.

2.4 Capsule Synthesis and Specimen Preparation

2.4.1 Synthesis of polyurethane microcapsules

The *in situ* synthesis adapted from Saihi et al. is described in the following steps [31]. First, 4.202mL of Span 85 and 2.116mL of polyethyleneglycol (PEG) was dissolved in 90mL of toluene. A 15mL aliquot was taken from this solution and placed into a separate beaker (referred to as E_1). Next, 0.682mL of methylene diisocyanate (Basonat) and 0.0469mL of dibutyl tin dilaurate was dissolved in E_1 . This blend was mixed at 350 rpm to ensure a homogenous mixture and set aside. The original mixture (Span 85, PEG and toluene) was combined with 30mL of water, stirring at 8000rpm in a homogenizer or blender. Finally, E_1 was added to this primary emulsion and stirred at 700rpm for 10 minutes at room temperature. The speed was reduced to 350rpm at 63 °C and allowed to react for 4 hours. A light microscopy image of a polyurethane microcapsule is shown in **Figure 3**.

2.4.2 Preparation of concrete samples containing microcapsules

The control samples are prepared in the same manner as presented in Chapter I. For the samples consisting of the healing system, microcapsules are dispersed in the 242 ml of water used in the primary mixture. They are distributed as 2% weight within each cube. After the capsules have been dispersed in the water, the microcapsule samples are prepared the same as the control samples. All samples were cured for 28 days before testing.

2.5 Experimental Procedures

2.5.1 Compressive Strength

The experimental procedure to determine the compressive strength of each specimen is adapted from ASTM C109 [38]. Each sample is centered between the two parallel discs. The load is set to compress at a rate of 1mm/min. For the first test, the load is stopped after the sample has reached a maximum load and shows a gradual descent, but is not allowed to reach failure. A graph of the live data is displayed, allowing the test to be stopped at the appropriate time. After the healing time has passed, each sample is retested to failure.

2.5.2 Flexural Strength

The experimental procedure to determine the flexural strength of each specimen is adapted from ASTM C348-97 [39]. The flexural strength is measured by means of a three point bend test. The setup of this experiment is shown in **Figure 4**. Samples are supported by two parallel beams and compressed by one central beam. The load is set to move at 0.25mm/min. For the first test, the load is stopped after the sample has reached a maximum load and shows a sharp descent, but is not allowed to reach failure. A graph of the live data is displayed, allowing the test to be stopped at the appropriate time. After the healing time has passed, each sample is retested to failure.

2.6 Results and Discussion

2.6.1 Compressive Strength

The results of the compressive strength test for 6 control samples and 6 samples containing microcapsules are presented in **Table 1**. The results for the control samples are, in ksi: 2.279, 2.283, 2.247, 2.244 and 2.276. The samples containing the microcapsules had the following strength values, in ksi: 2.253, 2.307, 2.875, 2.579 and 2.718. The increased strength of the samples with the microcapsules is thought to be caused by two factors. First, in areas where capsules were ruptured by the initial test, the C-S-H that forms in the 1 week healing period behaves elastically under stress. Also, other areas will contain microcapsules that have *not* ruptured. These are believed to also behave elastically and supply some form of cushioning since they are slightly flexible. Once these capsules have ruptured though, the material has then reached the maximum load it can withstand without the assistance of the capsules and C-S-H elasticity, leading to failure. Again, these may help the material compensate a higher load overall and maintain its integrity longer before reaching failure, resulting in higher strength values for the microcapsule samples.

2.6.2 Flexural Strength

This experiment was used to evaluate whether the material was able to recover some of its strength after acquiring some minor, microscale damage. First, the sample was tested until it reached a maximum load and showed the beginning of failing, indicated by the sharp decrease in the material's strength in each figure. The test was stopped so that the internal microcracking

would not become too large to heal by surfacing as much larger cracks. The samples were left to heal for one week. During this time period, the solution that is released from the capsules has time to react with the calcium hydroxide to form the C-S-H, healing some of the cracks that have formed. Ultimately, this would lead to the material obtaining more strength in the second test that is performed to failure compared to the control samples. The results for 6 control samples and 6 samples containing the microcapsules are shown in **Figures 5 and 6** and **Tables 2 and 3**. Strength recovery is reported as a percentage of the strength reached after minor damage has been induced compared to the maximum strength in the initial test. The control samples had about 10-14% of its initial strength left after microscale damage had occurred. The samples containing the microcapsules, however, had 20-26% recovered strength after the damage. This is indicative of the capsules rupturing where the cracks were initiated and healing them, providing more strength to the samples in the second test. Ultimately, this type of healing would be able to promote a longer life of the material since it is prolonging failure. Moreover, it is impressive that this material still maintained about 25% of its strength with only 2% weight of microcapsules in each sample.

In summary, the microcapsules proved to be an effective way of encapsulating the healing agent for a targeted release. The results from the compressive strength tests show that the capsules don't interfere with the cementitious matrix and slightly improve the materials strength with their presence. Their real ability is demonstrated in testing the flexural strength where the presence of the microcapsules helps the material perform *at least* 10% better than the control samples.



Fig 1. Example of brittle glass pipe filled with healing agent.

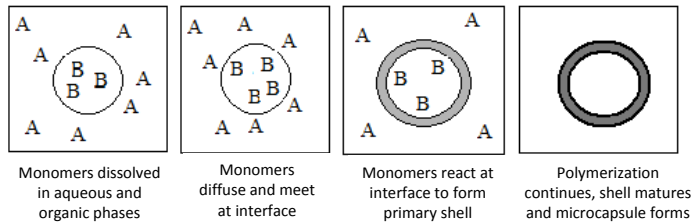


Fig 2. Schematic of formation of the shells from stable water droplets in a continuous oil phase (adapted from Yow and Routh).

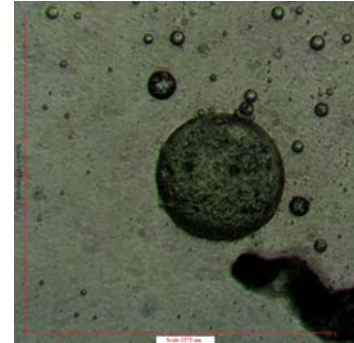


Fig 3 Polyurethane microcapsule synthesized via interfacial polymerization.



Fig 4. Instron instrument measured flexural strength (ASTM C348-97).

Sample	Control, strength in ksi	With 2%wt. microcapsules, strength in ksi
1	2.279	2.253
2	2.283	2.307
3	2.247	2.875
4	2.244	2.579
5	2.276	2.718

Table 1. Compressive strength values for control samples and those containing the microencapsulated healing agent.

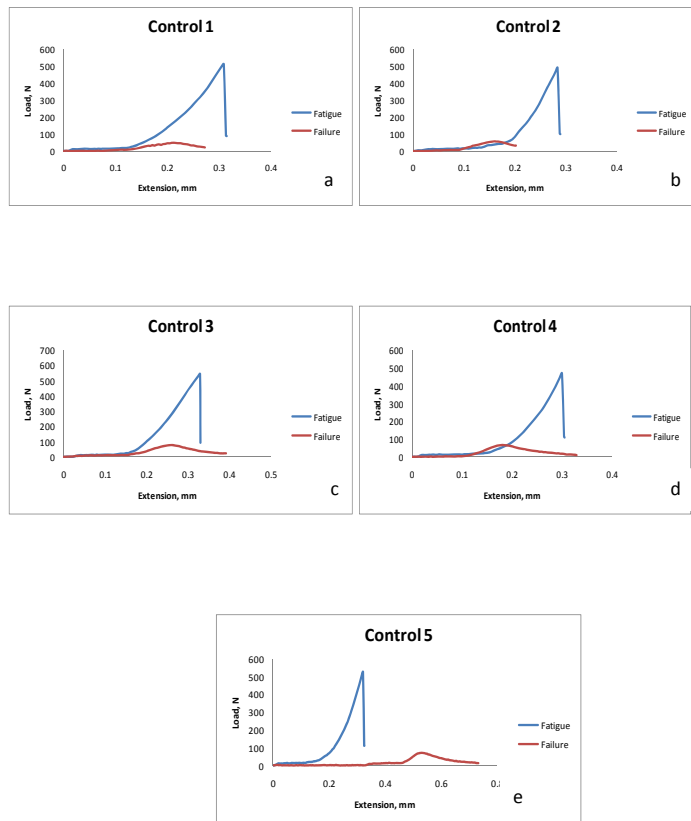


Fig 5. Graphical results from three point bend test for 5 control samples (a-e). The blue lines indicate when the material is weakened by a controlled load, inducing microscale damage. The red lines are where each sample is brought to failure.

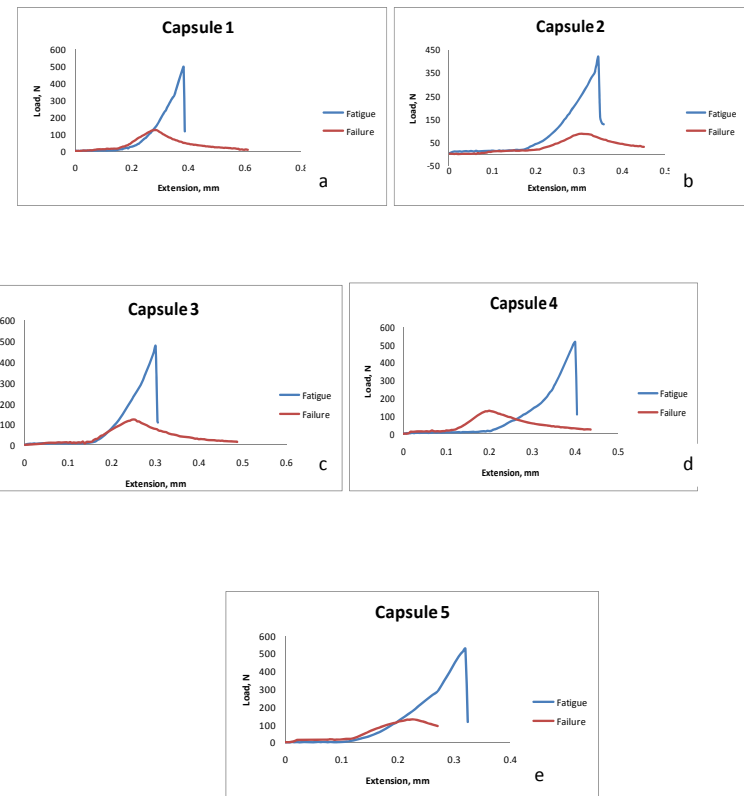


Fig 6. Graphical results from three point bend test for 5 samples containing microencapsulated healing agent (a-e). Blue lines indicate when material is weakened by a controlled load, inducing microscale damage. Red lines are where each sample is brought to failure.

Control	Initial Max Load, N	Max Load After Damage, N	Recovered, %
1	512.889	46.734	9.11
2	490.684	57.555	11.7
3	541.948	76.604	14.1
4	470.582	66.414	14.1
5	525.821	69.613	13.2

Table 2. Summary of flexural strength data for the control samples with their respective recovered strength percentages.

Capsule	Initial Max Load, N	Max Load After Damage, N	Recovered, %
1	495.665	124.373	25.1
2	416.688	85.927	20.6
3	476.583	125.231	26.2
4	513.821	127.525	24.8
5	528.222	130.555	24.7

Table 3. Summary of flexural strength data for the capsule samples with their respective recovered strength percentages.

REFERENCES

- Ishiwata, H.e.a., *Effects of restraining expansion on crack self-healing of concrete*. Konkurito Ronbunshu, 2007. **61**: p. 617-623.
- Nishiwaki, T.e.a., *Development of self-healing system for concrete with selective heating around crack*. Journal of Advanced Concrete Technology, 2006. **4(2)**: p. 267-275.
- Nishiwaki, T., et al., *Thermal Analysis of self-healing concrete system*. Konkurito Ronbunshu, 2009. **59**: p. 469-476.
- Nishiwaki, T., et al., *Development of self-healing concrete with heating device*. Konkurito Ronbunshu, 2005. **16(2)**: p. 81-88.
- Mihashi, H. and Y. Kaneko, *Intelligent concrete with self-healing capability*. Transactions of the Materials Research Society of Japan, 2000. **25(2)**: p. 557-560.
- Li, V.C., Y.M. Lim, and Y.-W. Chan, *Feasibility study of a passive smart self-healing cementitious composite*. Composites Part B, 1998. **29B**: p. 819-827.
- Pang, J.W.C. and I.P. Bond, *A hollow fibre reinforced polymer composite encompassing self-healing and enhanced damage visibility*. composites Science and Technology, 2005. **65**: p. 1791-1799.
- Dry, C.M., *Alteration of matrix permeability and associated pore and crack structure by timed release of internal chemicals*. Ceramic Transactions, 1991: p. 191-193.
- Dry, C.M., *Passive tunable fibers matrices*. International Journal of Modern Physics, 1992. **6**: p. 2763-2771.
- Dry, C.M. *Smart building materials which prevent damage or repair themselves*. in *Proceedings of the Materials Research Society Symposium*. 1992. California: Materials Research Society.
- Dry, C.M. *Smart materials which sense, activate and repair damage; hollow porous fibers in composites release chemicals from fibers for self-healing, damage prevention,*

and/or dynamic control. in *First European conference on smart structures and materials*. 1992. Glasgow, Scotland.

- Williams, G., R. Trask, and I.P. Bond, *A self-healing carbon fibre reinforced polymer for aerospace applications*. Composites Part A, 2007. **38(1525-1532)**.
- Williams, G., R. Trask, and I.P. Bond, *Bioinspired self-healing of advanced composite structures using glass fibres*. Journal of the Royal Society Interface, 2007. **4**: p. 363-371.
- Jonkers, H.M., et al., *Application of bacteria as a self-healing agent for the development of sustainable concrete*. Ecological Engineering, 2009.
- Raijiwala, *Bacterial Concrete: A Self-Healing Concrete*. The Icfai University Journal of Structural Engineering, 2008. **1(2)**: p. 56-63.
- Tittelboom, K.V., et al., *Use of bacteria to repair cracks in concrete*. Cement and Concrete Research, 2010. **40**: p. 157-166.
- Sottos, N.R., M.R. Kessler, and S.R. White, *Self-healing structural composite materials*. Composites Part A: Applied Science and Manufacturing, 2004. **34(8)**: p. 743-753.
- Yin Tao, e.a., *Self-healing woven glass fabric/epoxy composites with the healant consisting of micro-encapsulated epoxy and latent curing agent*. Smart Material Structures, 2008. **17**: p. 15-19.
- Brown, E.N., N.R. Sottos, and S.R. White, *Retardation and repair of fatigue cracks in a microcapsule toughened epoxy composite- Part II: In situ self-healing* Composites Science and Technology, 2005. **65(15-16)**: p. 2474-2480.
- Yin, T., et al., *Self-healing epoxy composites- Preparation and effect of the healant consisting of microencapsulated epoxy and latent curing agent*. Composites Science and Technology 2007. **67(2)**: p. 201-212.
- Yow, H.N. and F.A. Routh, *Formation of liquid core-polymer shell microcapsules*. Soft Matter, 2006. **2**: p. 940-949.
- Velev, O.D., K. Furusava, and K. Nagayama, *Assembly of latex particles by using emulsion droplets 1. Microconstructed Hollow Spheres*. Langmuir, 1996. **12**: p. 2374-2384.
- Velev, O.D., K. Furusava, and K. Nagayama, *Assembly of Latex particles by Using Emulsion Droplets are Templates 1. Reverse (Water in Oil)*. Langmuir, 1997. **13(1856-1859)**.
- Berg, J., D. Sundberg, and B. Kronberg, *Microencapsulation of emulsified oil droplets by in situ vinyl polymerization*. Journal of Microencapsulation, 1989. **6**: p. 327-337.

25. Kasai, K., et al., *Capsule-shaped polymer particles and process for the production thereof*, U.S.P. 4798691, Editor. 1989.
26. Cho, S.H., et al., *Polydimethylsiloxane-based self-healing materials*. *Advanced Materias*, 2006. **18**: p. 997-1000.
27. Katagiri, K. and F. Caruso, *Functionalisation of colloids with robust inorganic based lipid coatings*. *Macromolecules*, 2004. **37**: p. 9947-9953.
28. Schuetz, P. and F. Caruso, *Semiconductor and metal nanoparticle formation on polymer spheres coated with weak polyelectrolyte multilayers*. *Chemistry of Materials*, 2004. **16**: p. 3066-3073.
29. Zha, L., et al., *Monodisperse temperature-sensitive microcontainers*. *Advanced Materias*, 2002. **14**(1090-1092).
30. Frere, Y., L. Danicher, and P. Gramain, *Preparation of polyurethane microcapsules of interfacial condensation*. *European Polymer Journal*, 1997. **34**(2): p. 193-199.
31. Saihi, D., et al., *Microencapsulation of ammonium phosphate with a polyurethane shell. Part II. Interfacial polymerization technique*. *Reactive and Functional Polymers*, 2006. **66**(10): p. 1118-1125.
32. Yang, J., et al., *Microencapsulation of isocyanates of self-healing polymers*. *Macromolecules*, 2008. **41**: p. 9650-9655.
33. Dejugnat, C. and G.B. Sukhorukov, *pH-Responsive properties of hollow polyelectrolyte microcapsules templated on various cores*. *Langmuir*, 2004. **20**: p. 7265-7269.
34. Angelatos, A.S., B. Radt, and F. Caruso, *Light-responsive polyelectrolyte/gold nanoparticle microcapsules*. *Journal of Physical Chemistry*, 2005. **109**: p. 3071-3076.
35. Bedard, M.F., et al., *Polymeric microcapsules with light responsive properties for encapsulation and release*. *Advanced Colloid Interfaces Science*, 2009.
36. Chu, L.-Y., et al., *Preparation of thermo-responsive core-shell microcapsules with a porous membrane and poly(N-isopropylacrylamide) gates*. *Journal of Membrane Science*, 2001. **192**: p. 27-39.
37. Sukhishvili, S.A., *Responsive polymer films and capsules via layer-by-layer assembly*. *Current Opinion in Colloid and Interface Science*, 2005. **10**: p. 37-44.
38. Allen, R.F., et al., eds. *Annual Book of ASTM Standards*. Cement: Lime: Gypsum. Vol. 04.01. 1998, American Society for Testing and Materials: West Conshohocken, PA. 71-5.
39. Allen, R.F., et al., eds. *Annual Book of ASTM Standards*. Cement: Lime: Gypsum. Vol. 04.01. 1998, American Society for Testing & Materials: West Conshohocken, PA. 203-7.